UNIVERSITÀ
DEGLI STUDI
DI PADOVA

Sede Amministrativa: Università degli Studi di Padova

DIPARTIMENTO DI GEOSCIENZE

SCUOLA DI DOTTORATO DI RICERCA IN SCIENZE DELLA TERRA
CICLO XXV

MODERN *IN-SITU* XRD INVESTIGATIONS ON C_3S-C_3A-GY SYSTEMS

Direttore della Scuola: Ch.mo Prof. Massimiliano Zattin Massimiliano Zattin

Supervisore: Dott.ssa Maria Chiara Dalconi M. Chiara Dalconi

Dottorando: Marco Favero
Marco Favero

Abstract

The origin of cement, employed as a binding material, can be attributed to Romans who found that a mixture of lime and crushed volcanic ashes was able to set under water, the resistance being increased along the time, in a way completely different to any other material. Since that age, a huge amount of different kind of cements have been produced to satisfy the request of different mechanical behaviors. To deeply understand the mechanisms that lead to the development of mechanical strength, reaction kinetics that occur during the hydration process must be known. Nowadays we can affirm that cement research has set many important results but despite of this “long-time story”, a lot of improvements are required to better understand the mechanisms of kinetics.

Cements mixed with water are complex systems undergoing critical chemical and physical changes during the hydration process. A unique hydration model able to explain the controlling mechanisms is the main purpose of cement research, but the physical-chemical parameters involved are actually too many. To partly overcome the chemical complexity of common cement materials, simplified cement systems are often used for research purposes. A project has been set to investigate the fundamental reactions occurring during the hydration process and has been divided within 3 different partners: NIST (National Institute of Standards and Technology), W.R. GRACE and University of Padua. Our part of the project was to collect x-ray powder diffraction patterns on the hydrating suspensions, using Rietveld refinement for quantitative phase analysis.

Three simplified cement systems formed by the synthetic phases tricalcium silicate Ca_3SiO_5 (C_3S), tricalcium aluminate $Ca_3Al_2O_6$ (C_3A) and a varying amount of gypsum $CaSO4{\cdot}2H_2O$ ($C\check{S}H_2$) were investigated by means of *in-situ* x-ray powder diffraction (XRPD) and isothermal calorimetry (IC) in order to evaluate dissolution-precipitation kinetics. The main hydration products detected by means of XRPD were ettringite, hemicarboaluminate, portlandite, Ca-Si hydrates (C-S-H): the same occurring in real cements.

The Avrami nucleation and growth model successfully fits the degree of hydration data, confirming that C-S-H should have a layered structure as well as the phases resulting from the decomposition of ettringite. The mass balance method was used to calculate the exact amount of C-S-H formed during hydration, which is not directly accessible from Rietveld refinement. The comparison between the degree of hydration calculated from isothermal calorimetry data and the degrees of hydration calculated from x-ray diffraction has revealed how much the reactant phases are responsible for heat release. In particular, it was seen that the study of C_3S-C_3A-Gy systems is not a simple sum of the investigations of C_3S-Gy and C_3A-Gy systems, which are two further simplified model cements. The synthetic materials suffered a loss on reactivity despite of the under-vacuum sealing, leading to a continuous and unpredictable change of the materials features (particle size, degree of reactivity) during time.

The obtained experimental data should be necessary to proof the effectiveness of software modelling (HydratiCA). The software has been tested and returned satisfactory results for further simplified systems, such C_3S-Gy. Nevertheless, the software is still under a development stage and improvements has to be planned for C_3A-Gy systems before testing more complex blends.

Key words: x-ray powder diffraction, isothermal calorimetry, cement, simplified system, C3S-C3A-Gy, hydration kinetics.

Riassunto

L'origine del cemento, utilizzato come legante nell'industria costruttiva, può essere attribuita direttamente ai Romani, i quali osservarono come una miscela di calcare e ceneri vulcaniche finemente macinate fosse in grado, quando miscelata con acqua, di dar luogo a presa, prima, e ad alte resistenze meccaniche, poi, in un modo così efficace mai osservato precedentemente con altri materiali. Da quando i Romani hanno dato il via all'utilizzo di leganti idraulici, diverse tipologie di cemento sono state prodotte per diversi impieghi costruttivi. Per comprendere esaustivamente i meccanismi che conducono allo sviluppo delle resistenze meccaniche, è fondamentale conoscere a fondo come procedano le cinetiche di reazione durante il processo di idratazione.

La ricerca sui materiali cementizi ha oramai raggiunto risultati ragguardevoli in merito allo studio delle cinetiche chimiche ma, nonostante la lunga storia relativa a questi materiali ancora molto lavoro dev'essere svolto.

I cementi miscelati con acqua formano miscele complesse che si modificano in maniera significativamente complessa, sia dal punto di vista chimico sia dal punto di vista fisico, durante il processo di idratazione. Un modello di idratazione univoco che riesca a spiegare tutte le fasi del processo di idratazione è il fine ultimo della ricerca sui materiali cementizi, sebbene questo obiettivo sia ancora lontano, a causa dei numerosi parametri chimico-fisici coinvolti. Per ovviare almeno in parte la complessità dei materiali cementizi tradizionali, per scopi scientifici vengono prodotti sistemi cementizi semplificati, caratterizzati soprattutto da un numero di fasi inferiore rispetto ad un cemento tradizionale.

Un progetto di ricerca è stato messo a punto per approfondire l'aspetto delle cinetiche di reazione. Tre partner sono coinvolti: NIST (National Institute of Standards and Technology), W.R. GRACE ed Università degli Studi di Padova. La parte di progetto inerente al nostro gruppo di ricerca riguardava l'utilizzo della diffrazione in-situ di raggi X per polveri sulle paste in idratazione, utilizzando l'analisi quantitativa con il metodo Rietveld per quantificare l'andamento delle

fasi nel tempo. Sono stati scelti tre diversi sistemi cementizi semplificati, formati da materiali sintetizzati in laboratorio: silicato tricalcico Ca_3SiO_5 (C_3S), alluminato tricalcico $Ca_3Al_2O_6$ (C_3A) e diverso contenuto di gesso $CaSO4{\cdot}2H_2O$ ($C\check{S}H_2$). Sono state impiegate le tecniche di diffrazione *in-situ* di raggi X per polveri (XRPD) e calorimetria isoterma (IC) per valutare le cinetiche di dissoluzione e precipitazione di reagenti e prodotti. Dall'analisi qualitativa dei diffrattogrammi, i principali prodotti di idratazione individuati sono ettringite, emicarbonato, portlandite, idrati di Ca-Si (C-S-H): gli stessi prodotti di idratazione che si possono individuare nei cementi tradizionali.

Il modello di nucleazione e crescita di Avrami descrive adeguatamente la curva del grado di idratazione, confermando che il C-S-H mostra una struttura a strati, come pure le fasi che derivano dalla decomposizione dell'ettringite. Il metodo del bilancio di massa è stato utilizzato per ricavare quanto C-S-H precipita durante l'idratazione, quantità che non è direttamente calcolabile neanche attraverso l'analisi quantitativa col metodo Rietveld. Confrontando la curva del grado di idratazione calcolato dalla calorimetria isoterma e le curve del grado di idratazione ricavate dai dati in diffrazione rivelano le fasi che qualitativamente e quantitativamente sono maggiormente implicate nello sviluppo di calore. In particolare, si è visto che lo studio dei sistemi C_3S-C_3A-Gy non coincide con la "somma algebrica" dei risultati sugli studi di C_3S-Gy e C_3A-Gy (due sistemi cementizi ulteriormente semplificati). I materiali di partenza hanno subito una perdita di reattività, nonostante siano stati conservati sottovuoto. La perdita di reattività ha di fatto modificato continuamente i materiali, cambiando spesso le condizioni iniziali (distribuzione granulometrica, grado di reattività) portando a risultati non facilmente prevedibili.

I risultati ottenuti sperimentalmente dovrebbero essere propedeutici per provare l'efficacia del software di modellazione (HydratiCA). Il software è stato provato sul sistema C_3S-Gy, fornendo risultati incoraggianti. Tuttavia, tale software, essendo ancora in fase di sviluppo, necessita di miglioramenti soprattutto per quanto riguarda il sistema C_3A-Gy, prima di poter passare alla simulazione di miscele più complesse.

Parole chiave: diffrazione di raggi X per polveri, calorimetria isoterma, cemento, sistema semplificato, C_3S-C_3A-Gy, cinetiche di idratazione.

TABLE OF CONTENTS

NOMENCLATURE AND ABBREVIATIONS

The composition of a cement is usually expressed as the constituents oxides. For example, tricalcium silicate Ca_3SiO_5 is then indicated as $3CaO{\cdot}SiO_2$, abbreviated C_3S. In common cement nomenclature, oxides are expressed as single capital letters, as following:

$C = CaO$
$S = SiO_2$
$A = Al_2O_3$
$F = Fe_2O_3$
$M = MgO$
$K = K_2O$
$\check{S} = SO_3$
$N = Na_2O$
$T = TiO_2$
$P = P_2O_5$
$H = H_2O$
$\check{C} = CO_2$

General components are written as common chemical formula (i.e., CaO) while phases are written as abbreviations (i.e., C_3S). Chemical formula, oxides composition and abbreviations of principal cement phases are reported in table 1.1.

MINERAL NAME	CHEMICAL FORMULA	CEMENT ABBREV.
Calcite	$CaCO_3$	$C\check{C}$
Calcium Silicate Hydrates	$CaO_x(SiO_2)_x$	C-S-H
Dicalcium Silicate (belite)	Ca_2SiO_4	C_2S
Ettringite	$Ca_5Al_2(SO_4)(OH)_{12}{\cdot}26H_2O$	$C_6A\check{S}_3H_{32}$
Gypsum	$CaSO_4{\cdot}2H_2O$	$C\check{S}H_2$
Monosulphate	$Ca_4Al_2(SO_4)(OH)_{12}{\cdot}6H_2O$	$C_4A\check{S}H_{12}$
Portlandite	$Ca(OH)_2$	CH
Tetracalcium aluminate ferrite	$Ca_4Al_2Fe_2O_{10}$	C_4AF
Tricalcium aluminate	$Ca_3Al_2O_6$	C_3A
Tricalcium silicate	Ca_3SiO_5	C_3S

Table 1.1: summary of principal cement phases, expressed as minerals, chemical formulas and abbreviations used in cement science.

GLOSSARY

Cement: hydraulic binder

Concrete: it is a composite mix of cement and mineral aggregates. Such aggregates (sand, rock fragments, gravel) do not reduce mechanical strength despite they represent the 80%-85% of total volume

Mortar: composite mix of cement and mineral aggregates, which dimension is lower than 2 mm

Set: loss of workability of cement paste

Hardening: increase of mechanical strength

Clinker: multiphase aggregate of calcium silicates and aluminates, produced by heating limestone and clay at 1450°C; it is the main cement component (94-96%)

Portland cement: hydraulic binder principally used in construction. Its constituents are finely grinded clinker plus a certain amount of calcium sulphates (4-6%).

Cement paste: viscous material obtained by mixing cement powder with water.

1. Introduction

1.1. General considerations about cement-based materials

When considering cement and, more generally, cement-based materials, we think about a very common material, principally used in construction operations. First use of cementitious materials is directly related to Romans by the engineer Vitruvius, who described the increasing resistance during time of a mixture of lime and crushed volcanic ashes when mixed with water [1]. During the medieval age, masons were able to produce structures with hydraulic cement such as canals, fortresses, harbours and shipbuilding facilities [2], [3]. Later in the 18th century, French and British engineers set the technical knowledge in making hydraulic cements [2], reaching the important result of patenting the process for manufacturing the Portland cement in 1824 by Joseph Aspdin [4], refined by C. Johnson in 1845 who increased the firing temperature and producing a binder more similar to the actual Portland cement.

Portland cement is produced by firing at 1450°C a blend of limestone and claystone or closely related materials with proper reactivity. The firing process induces a partial melting that is responsible of the production of clinker grains. Such grains are finely grinded and mixed with a varying amount of Gypsum (3 – 5% of weight) or other calcium sulphates to obtain the cement.

A general cement composition can be expressed by oxides as well as by phases. In table 1.2 a common cement composition is reported both as oxides and major/minor phases [5].

Oxides [wt %]		Major phases [wt %]		Minor phases [3% wt]
CaO	67	C_3S (alite)	50 – 70	Periclase (MgO)
SiO_2	22	β-C_2S (belite)	15 – 30	Free lime (CaO)
Al_2O_3	5	C_3A (alluminates)	5 – 10	Portlandite ($Ca(OH)_2$)
Fe_2O_3	3	C_4AF (ferrite)	5 – 15	Arcanite (K_2SO_4)
SO_3	2			Aphtitalite ($(K,Na)SO_4$)
MgO	2			
$K_2O + Na_2O$	1			
Others	3			

Table 1.2: Portland cement composition described as oxides, major and minor crystalline phase

This long-term story should suggest a deep knowledge into the cement science, but this is not completely exact. Considering cements as non-natural powders we know that they produce huge mechanical strength when mixed with water. The whole processes involved during hydration are not completely understood because physic, chemical (phase compositions and solubility, pH, ions concentration in solution) and microstructural (pores distribution) parameters are vary and interdependent. An exclusive hydration model for different type of cements is hard to develop but it represents the most important goal in cement science. Furthermore, the poorly crystalline and nanometric main hydration products, which assure the mechanical strength to hardened cement, are difficult to be investigated by traditional analytic methods.

In this direction simplified cement systems offer a different insight into the hydration process of cementitious materials. Simplified systems become useful because their composition is originally known and the reaction that occur during hydration processes can be predicted more accurately.

1.2. The hydration process

The mechanical strength that characterizes cementitious materials is developed during the process called hydration, which involves crystalline phases and water to produce a cement paste. Hydration always entails an increase of paste temperature, because reactions involved are mostly exothermic. Solid to solid and solid to liquid transformations occurring during these complex processes pass through set and hardening stages. Set is recognizable because cement suffers a loss of workability till it becomes no more handable: in particular this is due to aluminate hydration. Hardening is the subsequent step, related to the marked increase in mechanical strength. Chemical transformations such as clinker phases dissolution lead to the precipitation of hydrous phases. Dissolution and crystallization are controlled by the chemical composition of percolating fluids and by diffusion processes. Such processes are strictly connected to porosity (microstructural properties) that evolves during the evolution of hydration.

Each phase has a different dissolution reaction rate and this lead to a different development of mechanichal strength:

- C_3S hydration kinetics is very fast (time scale: days) and it is the main responsible for the mechanical strength measured at 28 days.
- C_2S shows slower kinetics and it influences the rheological behaviour in the long period.
- C_3A and C_4AF are more responsible for material setting: during the first minute of hydration they release a great amount of heat. Sulphate addition is necessary to avoid the undesiderable flash setting.

In most cases the hydration process is described looking at its temporal evolution, measuring the heat production of hydration pastes. We can distinguish 4 main phases (figure 1.1):

1. First minutes of hydration: alluminate dissolution (especially C_3A) and preceipitation of Ca-Al-sulphate hydrates (especially Ettringite).
2. Induction period (2 – 4 hours): hydration kinetics become very slow.
3. Main hydration period (until 24 – 48 hours): clinker phases suffer a dramatic increase in dissolution rate called acceleration period, with a consequent fast precipitation of Ca-Si hydrates (C-S-H) and Ca-hydroxide (Portlandite) that lead to hardening of cement.

4. Long-term hydration (days – months): continuous process where mechanichal strength increase is very slow.

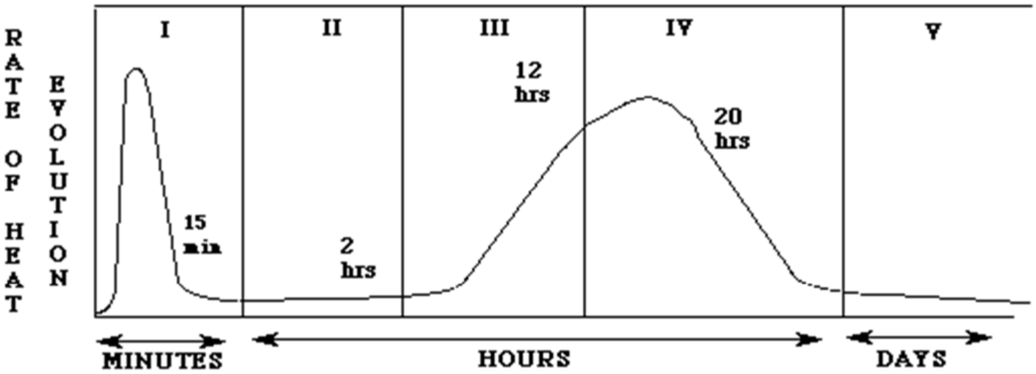

Figure 1.1: calorimetric curve related to the rate of heat evolution during the hydration of an Ordinary Portland Cement [6].

Considering cement workability, the first minutes and the induction period play a fundamental role. Acceleration period determines the end of workability. The fast heat release is generally associated to alluminate hydration, while the loss of workability to silicate hydration. Summarizing the hydration scheme of figure 1.1. we have i) the alluminate hydration controls the workability while ii) silicate hydration determines the end of setting and the subsequent increase in mechanical strength.

Alluminate hydration

Al-rich phases lead to the production of ettringite ($C_6A\check{S}_3H_{32}$), if sulphates content is sufficient. Otherwise, monosulphoaluminate ($C_4A\check{S}H_{12}$) and Ca-Al hydrates (C-A-H) become the dominant phases. Without any sulphate phase present, the so-called flash set occurs (loss of workability in the first minutes of hydration). This is an undesired effect, solved with the addiction of Ca-sulphates (mainly gypsum) that act as set control.

$$C_3A + 26H_2O + 3C\check{S}H_2 \rightarrow C_6A\check{S}_3H_{32} \tag{1.1}$$

$$C_3A + 10H_2O + C\check{S}H_2 \rightarrow C_4A\check{S}H_{12} \tag{1.2}$$

Silicate hydration

Hydration of C_3S e C_2S produce poorly crystalline calcium-silicate hydrates C-S-H and portlandite:

$$Ca_3SiO_5 + (3 + y - x)H_2O \rightarrow (CaO)_x(SiO_2)\cdot H_2O + (3 - x)Ca(OH)_2 \qquad (1.3)$$

C-S-H has not a fixed stoichiometry and and a precise crystalline structure. During hydration, C-S-H composition varies in water content (y) and in Ca/Si ratio (x) [6].

1.3. Tricalcium Aluminate

1.3.1. Crystal Structure

C_3A ($Ca_3Al_2O_6$) is a synthetic phase with cubic symmetry, as the cell side a = 15.263 Å, space group P a 3 and Z = 24. The structure is built by Ca^{2+} cations and rings composed by 6 AlO_4 tetrahedra, with formula $(Al_6O_{18})^{18-}$ [6].

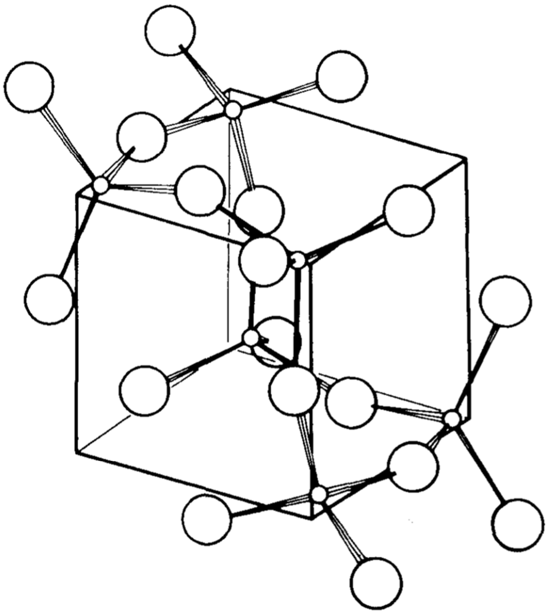

Figure 1.2: Al_6O_{18} rings in C_3A structure. Al atoms are located close to the edges of a cube [6, 7].

The unit cell is composed by 64 subcells, with a side length of 3.816 Å, and eight of these subcells are occupied by $(Al_6O_{18})^{18-}$ rings. Ca^{2+} cations are localized in the middle of, or in proximity of the edges of the remaining subcells. Edge Ca^{2+} cations have 6-fold coordination while the rest of Ca^{2+} have an irregular coordination number. Na^{+} can partly substitute Ca^{2+}, generating solid solutions with general formula $Na_{2x}Ca_{3-x}Al_2O_6$ (con $0 < x < 0.25$). Up to 1% of Na_2O ($x \approx 0.04$) in the structure implies no significant changes while if Na_2O content increases, the symmetry passes from cubic to monoclinc, passing through orthorhombic (table 1.5). Without any other chemical substitution, Na^{+} content reach 5.7% of Ca^{2+} substitution ($x = 0.25$).

% Na_2O	Compositional range x	Abbreviation	Crystal system	Space group
0 – 1-0	0 – 0.04	C_I	Cubic	P a 3
1.0 – 2.4	0.04 – 0.10	C_{II}	Cubic	P 2_1 3
2.4 – 3.7	0.10 – 0.16	C_{II} + O	-	-
3.7 – 4.6	0.16 – 0.20	O	Orthorhombic	P b c a
4.6 – 5.7	0.20 – 0.25	M	Monoclinic	P 2_1 / a

Table 1.3: structural changes of $Na_{2x}Ca_{3-x}Al_2O_6$ at different Na contents [6, 7].

The two cubic forms of C_3A are difficult to be distinguished by x-ray powder diffraction (XRPD): the cell parameter a of C_I (a = 15.263 Å) is too similar to that of C_{II} (a = 15.248 Å). The orthorhombic structure is close to C_I and C_{II} regarding the unit cell composed by pseudo-cubic sub-cells (a = 3.8 Å), but it differs for the Al_6O_{18} rings positions in the sub-cells. The monoclinic structure is obtained from a distortion of the orthorhombic, showing a β angle of 90.1°.

Al^{3+} cations can be substituted by Fe^{3+} and Si^{4+}, up to 4% for Fe_2O_3 and 2% for SiO_2. Higher substitution values can be reached only for non-equilibrium conditions, i.e. the crystallization from under-cooled melts.

1.3.2. Hydration Products

Tricalcium aluminate is extremely reactive when mixed with water. As soon as the first molecules interact together, metastable products are immediately produced (AFm phases) and later converted to the more stable hydrogarnet. These intermediate phases are poorly crystalline, with a varying composition, mostly producing a gel of blurred phases. Such phases can grow as hexagonal crystals, with a perfect basal cleavage (0001), if certain conditions (pH, Ca/SO_3 ratio) become opportune. They are called hexagonal aluminate hydrates or AFm phases (A: Al_2O_3 F: Fe_2O_3 m: monosulphate), with general formula $[Ca_2(Al, Fe)(OH)_6]\cdot X\cdot xH_2O$, where X stands for OH^-, $(SO_4)^{2-}$, $(CO_3)^{2-}$, Cl^- anions which can be all included in the same phase [6]. A common feature of AFm phases is the 6-fold coordination of $Ca(OH)_6$ portlandite-like sheets, with a third of all Ca^{2+} cations substituted by Al^{3+} or partly by Fe^{3+} (figure 1.7). The positive charge obtained after the substitution $Al^{3+} \rightarrow Ca^{2+}$ is balanced by in-layer anions X or X^{2-} and water molecules. Al^{3+} and Fe^{3+} replacement induces a distortion in the main layers, which lead Ca^{2+} to coordinate even the oxygen of water molecules, besides the 6 OH^- anions. The general formula representing a unit sheet can be summarized as $[Ca_2(Al,Fe)(OH)_6\cdot 2H_2O]^+$. In a simple AFm phase these units are piled up to build octahedral pits that contain X-type ions and water molecules.

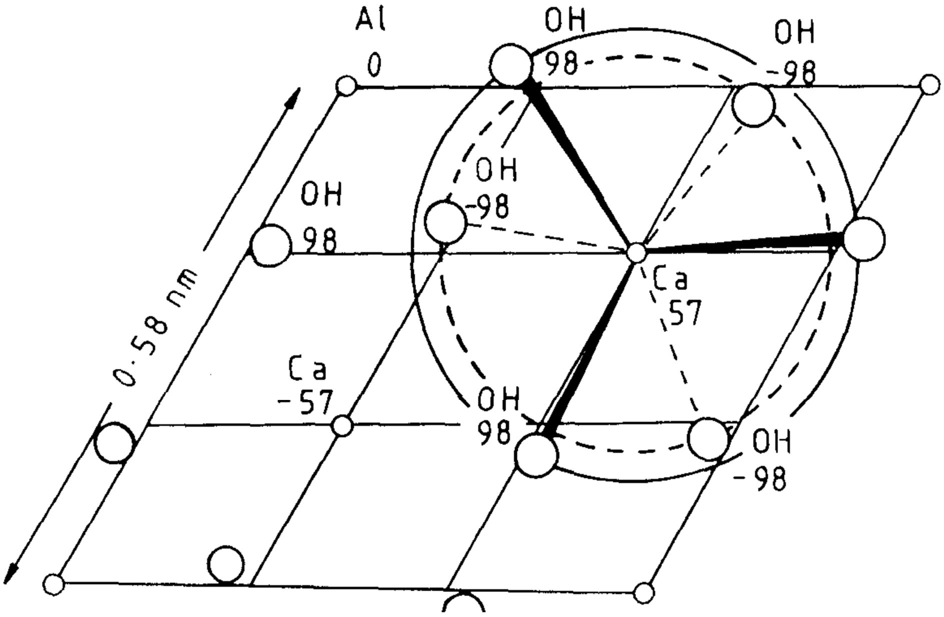

Figure 1.3: the structure of one $[Ca_2Al(OH)_6]^+$ layer in an AFm phase, a-b projection. Length values are expressed in pm. H atoms have been omitted. Big circles show the distortion of CaO_6 octahedra, that give to Ca atoms a coordination number up to 7 with

the addition of one water molecule (not in the figure) above or below the plane of this projection [6, 9, 10].

Because of this peculiar structure, the variation of cell parameters *a* and *b* is not wide within compounds of different composition, while parameter *c* significantly change depending on which ions and molecules enter in the interlayer levels (table 1.6).

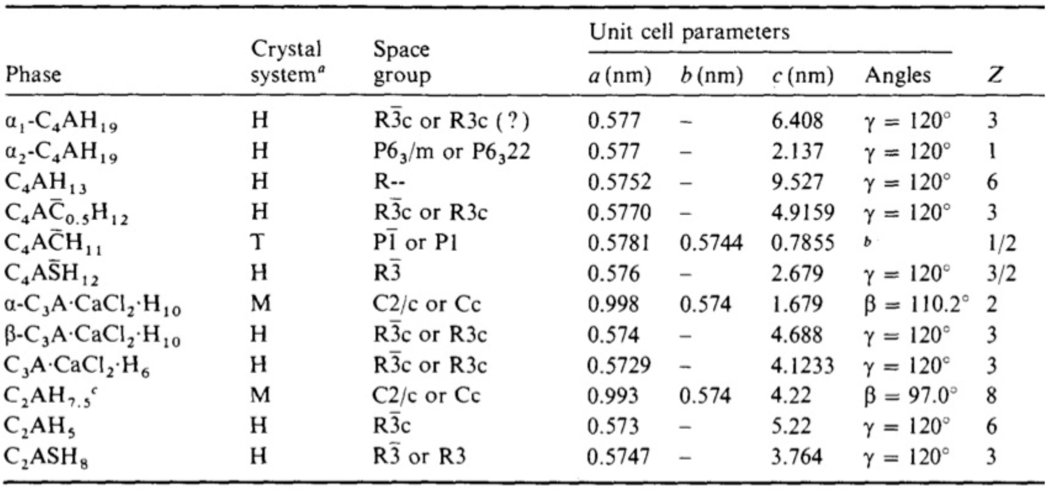

Phase	Crystal system^a	Space group	Unit cell parameters				Z
			a (nm)	*b* (nm)	*c* (nm)	Angles	
α_1-C_4AH_{19}	H	$R\bar{3}c$ or R3c (?)	0.577	–	6.408	$\gamma = 120°$	3
α_2-C_4AH_{19}	H	$P6_3/m$ or $P6_322$	0.577	–	2.137	$\gamma = 120°$	1
C_4AH_{13}	H	R--	0.5752	–	9.527	$\gamma = 120°$	6
$C_4A\bar{C}_{0.5}H_{12}$	H	$R\bar{3}c$ or R3c	0.5770	–	4.9159	$\gamma = 120°$	3
$C_4A\bar{C}H_{11}$	T	$P\bar{1}$ or P1	0.5781	0.5744	0.7855	^{b}	1/2
$C_4A\bar{S}H_{12}$	H	$R\bar{3}$	0.576	–	2.679	$\gamma = 120°$	3/2
α-$C_3A \cdot CaCl_2 \cdot H_{10}$	M	C2/c or Cc	0.998	0.574	1.679	$\beta = 110.2°$	2
β-$C_3A \cdot CaCl_2 \cdot H_{10}$	H	$R\bar{3}c$ or R3c	0.574	–	4.688	$\gamma = 120°$	3
$C_3A \cdot CaCl_2 \cdot H_6$	H	$R\bar{3}c$ or R3c	0.5729	–	4.1233	$\gamma = 120°$	3
$C_2AH_{7.5}{}^c$	M	C2/c or Cc	0.993	0.574	4.22	$\beta = 97.0°$	8
C_2AH_5	H	$R\bar{3}c$	0.573	–	5.22	$\gamma = 120°$	6
C_2ASH_8	H	$R\bar{3}$ or R3	0.5747	–	3.764	$\gamma = 120°$	3

Table 1.4: structural characteristics of AFm phases. H: Hexagonal, T: Triclinic, M: Monoclinic [6].

Another important factor is the thermodynamic stability of different AFm, that changes with the entering anion or the molecule in the interlayers of these metastable phases (table 1.7). During hydration, $(OH)^-$ anions are present in solution at high concentrations; $(SO_4)^{2-}$ and $(CO_3)^{2-}$ are less soluble and so low amounts are detectable at high pH values. Various sources are responsible for sulphate and carbonate contents, either during clinker preparation or after clinkerisation (e.g. gypsum, which can be contaminated by carbonates). These notes are useful to consider the variety in cements composition, because some AFm are metastable in any conditions and tend to decompose while other AFm are included in well-defined stability fields. To give an example, hemicarboaluminate and monocarboaluminate bear only 3.9% and 7.7% by weight of CO_2, respectively: this is one reason to evaluate the carbonate (and sulphate, that will be treated in a separate section) content.

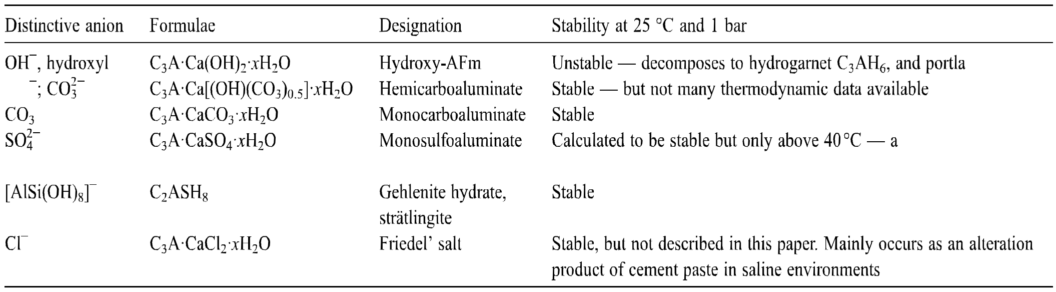

Distinctive anion	Formulae	Designation	Stability at 25 °C and 1 bar
OH^-, hydroxyl	$C_3A{\cdot}Ca(OH)_2{\cdot}xH_2O$	Hydroxy-AFm	Unstable — decomposes to hydrogarnet C_3AH_6, and portla
$^-$; CO_3^{2-}	$C_3A{\cdot}Ca[(OH)(CO_3)_{0.5}]{\cdot}xH_2O$	Hemicarboaluminate	Stable — but not many thermodynamic data available
CO_3	$C_3A{\cdot}CaCO_3{\cdot}xH_2O$	Monocarboaluminate	Stable
SO_4^{2-}	$C_3A{\cdot}CaSO_4{\cdot}xH_2O$	Monosulfoaluminate	Calculated to be stable but only above 40 °C — a
$[AlSi(OH)_8]^-$	C_2ASH_8	Gehlenite hydrate, strätlingite	Stable
Cl^-	$C_3A{\cdot}CaCl_2{\cdot}xH_2O$	Friedel' salt	Stable, but not described in this paper. Mainly occurs as an alteration product of cement paste in saline environments

Table 1.5: thermodynamic stability features of main AFm phases at 25°C [11].

Certain AFM phases show polytypism due to the different piling of structural units. A wide compositional range, linked with marked instability and poor crystallinity, lead to a difficult distinction among the hydrous phases during the cement hydration process. For example, in $CaO - Al_2O_3 - H_2O$ ternary system, up to 50°C the equilibrium phase is C_4AH_{19}, for which 2 polytypes are known (α 1 and a α2). The interlayer water content decreases with decreasing relative humidity and increasing temperature: 81% of relative humidity is sufficient to produce C_4AH_{13}. C_4AH_{19} can be obtained adding a layer of water molecules to C_4AH_{13}.

C_3AH_6 – Hexahydrate tricalcium aluminate – Hydrogarnet

This phase is the result of the hydration of C3A and its structure is very similar of Grossular ($Ca_3Al_2Si_3O_{12}$), in which Si, Al and Ca have tetrahedral, octahedral and distorted cubic coordination, respectively. Each oxygen is bond to 1 Si atom, 1 Al and 2 Ca. The absence of a some Si atoms (up to all atoms), in hydrogarnet, lead to a negative charge increase balanced by the substitution of O atoms, previously bonded to Si, with $(OH)^-$. The $Ca_3[Al(OH)_6]_2$ crystal structure is cubic, with a = 12.57 Å, space group I a 3 d and Z = 8 [6]. The icosytetrahedron habitus is clearly visible and cubic symmetry is easily detectable (figure 1.8).

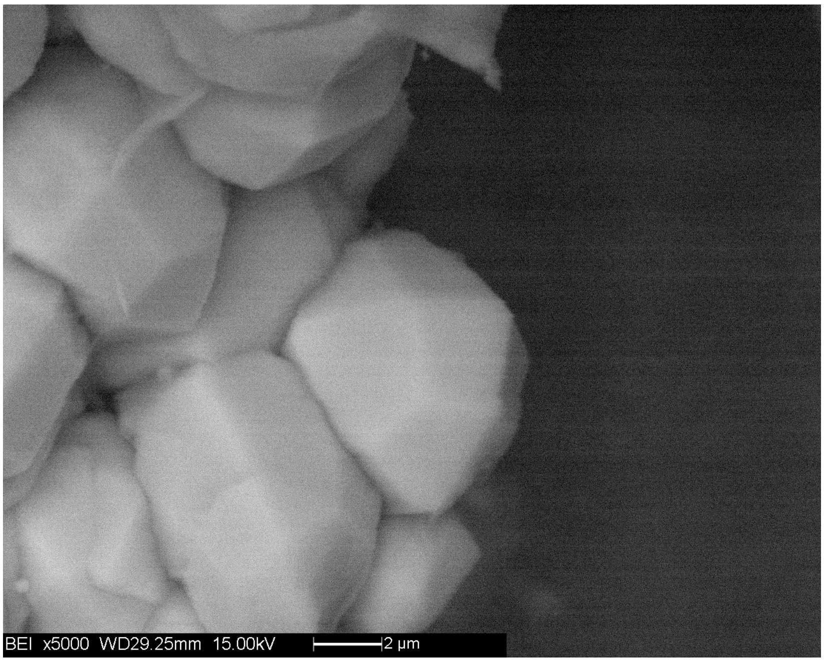

Figure 1.4: Hydrogarnet SEM micrograph in back-scattered electrons (scale in figure).

Al^{3+} anion can be partly substituted by Fe^{3+}. Hydrogrossular (another name for hydrogarnet) is the only stable phase at ambient temperature in the chemical CaO – Al_2O_3 – H_2O system. Other aluminate hydrated phases grow at lower temperature, with an hexagonal structure (AFm) and tend to transform to the more stable hydrogarnet with increasing temperature and time of hydration.

1.3.3. The role of gypsum

In the presence of gypsum, C_3A dissolves to produce ettringite, following the reaction:

$$C_3A + 26H_2O + 3C\check{S}H_2 \rightarrow C_6A\check{S}_3H_{32} \qquad \text{ettringite (Calcium trisulphate, AFt)}$$

Primary ettringite precipitation forms a thin barrier of needles over C_3A surface, stopping or delaying C-A-H formation. Anions $(SO_4)^{2-}$ content become extremely important, especially if the pore water solution is saturated about sulphate content after the paste hardening: secondary ettringite precipitation can occur, leading to the formation of pervasive cracks due to the expansive behaviour of ettringite formation.

Ettringite is a stable phase until the solution is saturated in respect of $(SO_4)^{2-}$. The saturation character is guaranteed by the continuous dissolution of sulphate phases: when all of them are completely disappeared, ettringite is converted into monosulphoaluminate (or monosulphate, AFm phase):

$$2C_3A + C_6A\check{S}_3H_{32} + 4H \rightarrow 3C_4A\check{S}H_{12} \qquad \text{monosulphoaluminate} \qquad (1.4)$$

The conversion of ettringite into monosulphoaluminate breaks the barrier and C_3A can hydrate originating Ca-Al hydrates. $C_4A\check{S}H_{12}$ produces solid solutions in which more than half of $(SO_4)^{2-}$ anions are substituted by $(OH)^-$ anions. It is still debated if $C_4A\check{S}H_{12}$ and C_4AH_{13} can form a solid solution: optical microscopy shows a complete solid solution while XRPD shows a miscibility gap.

Concerning about the crystal structure, monosulphate is well described by the natural mineral Kuzelite which shows trigonal system, space group R 3, with cell parameters a = 5.76 Å and c = 53.66 Å, Z = 3. The first three most intense peaks appears at 9.89°, 20.13° and 40.71° 2θ. The crystal shape is very similar to that of micas, showing platy microcrystals.

Ettringite crystal structure is also well established: it grows in prismatic or needle-like hexagonal-based crystals, belonging to the trigonal system, with a = 11.23 Å and c = 21.50 Å, space group $P\ 3_1\ c$ and Z = 8 [12]. The structure is composed by columns parallel to c axis made of octahedra $[Al(OH)_6]^{3-}$ each followed by groups of CaO_8 polyhedra. Each Ca^{2+} is bonded to 4 $(OH)^-$ and 4 H_2O molecules; columns have empirical formula $\{Ca_6[Al(OH)_6]\cdot 12H_2O\}^3$. Every 2 columns there are 4 sites, three of them filled by $(SO_4)^{2+}$ and one occupied by 1 or 2 H_2O molecules [13, 14]. This structure lead to write the ettringite formula as $\{Ca_6[Al(OH)_6]\cdot 12H_2O\}\cdot 3SO_4\cdot 2H_2O$, with columns repetition period along c axis of about 10.75 Å.

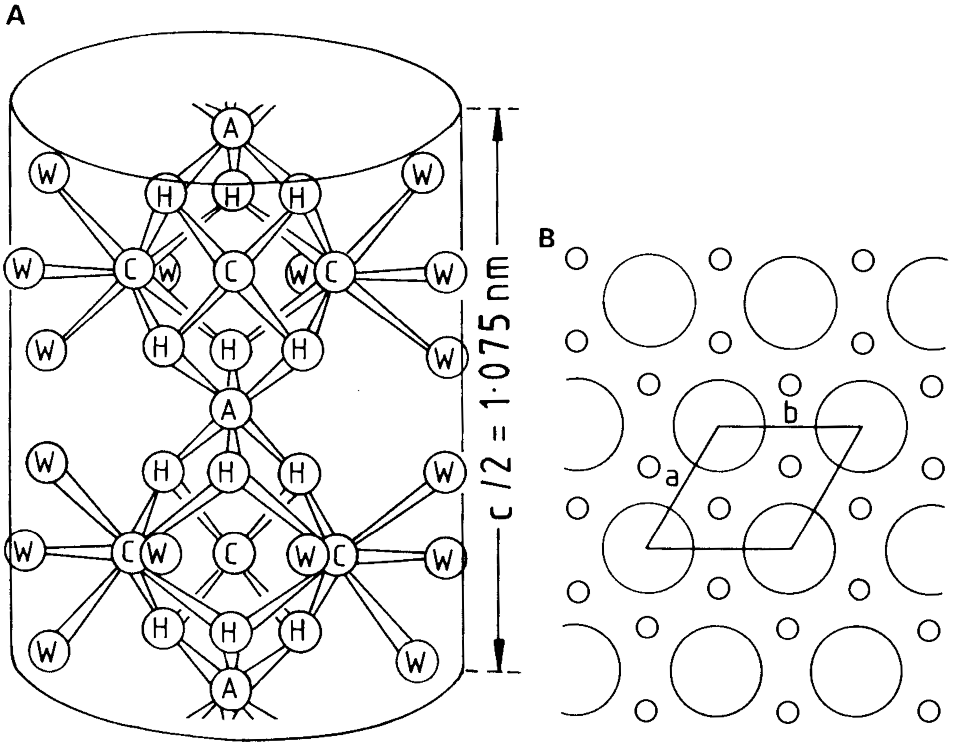

Figure 1.5: crystal structure of ettringite. (A) projection of a part of single column. (11-20). A=Al, C=Ca, H=O of one OH group, W=O of one water molecule. Hydrogen atoms and water molecules bonded to Ca atoms in the middle of the vertical line have been omitted. (B) a-b projection that shows columns (big circles) channels (small circles). Unit cell with a = 11.23 Å is drawn in the middle of the figure [6, 12].

Ettringite can bear Fe^{3+} in substitution of Al^{3+} at low amounts. Other important substitutions involve $(CO_3)^{2-}$ in place of $(SO_4)^{2-}$ and Si in place of Al until reaching the composition of Thaumasite ($C_3S\check{S}\check{C}H_{15}$), which has a crystal structure very similar to ettringite but showing the peculiar Si^{4+} in octahedral coordination. The 2 phases are not completely miscible, but they probably constitute a partial solid solution.

The upper thermal stability limit for ettringite stands at 110°C, but in many cements its content decreases at increasing temperature: over 50°C AFm phase is favoured.

Water content in ettringite reaches 50% in weight, giving a density of 1.77 g/cm^3. C3A-gypsum hydration can give different products when the $C\check{S}H_2/C_3A$ molar ratio is considered (table 1.8). Such information can become useful when we are not able to discriminate which Ca-Al hydrates grow in the presence of gypsum.

$C\bar{S}H_2/C_3A$ molar ratio	Stable hydration products formed
3.0	$C_6A\bar{S}_3H_{32}$
3.0 - 1.0	$C_6A\bar{S}_3H_{32} + C_4A\bar{S}H_{12}$
1.0	$C_4A\bar{S}H_{12}$
< 1.0	$C_4A\bar{S}H_{12}$ - C_4AH_{13} solid solution
0	C_3AH_6

Table 1.6: comparative table which indicates the stable hydrate phase that precipitates depending on the molar ratio $C\check{S}H_2/C_3A$ [5].

1.3.4. State of the art about C_3A – Gypsum hydration

As previously described, C3A hydration in the presence of gypsum lead to the formation of Afm and Aft sulphoaluminates. Hampson and Bailey [14] consider pH the fundamental parameter to discriminate the formation of different products. When pH increases (form 11.5 to 12.8) ettringite forms in low amounts but it remains for a long time without dissolving. TEM micrographs show C3A grains enveloped by small sulphoaluminates fibres [14]. Moreover, SEM micrographs on solutions at different pH show that such fibres remains stuck at C3A for pH values between 12.6 and 13.0. At pH = 13 fibres are smaller than that observed at lower pH. At pH = 13.2 no fibres are present, after 30 minutes of hydration [14]. At pH ≤ 12.4 foils or platelets are observed and interpreted as Afm belonging to the C_2AH_8-C_4AH_{19} – $C_4A\check{S}H_{12}$ solid solution: these phases dissolve to precipitate ettringite from the solution [14]. The authors also used a gypsum/portlandite solution to hydrate C3A, where small platelets similar to that described by Breval [13] have been observed; such platelets are rapidly substituted or covered by a layer of thin fibres of dimensions 0.2 μm x 0.5 μm. Finally at 4 hours of hydration such thin layer brakes and underneath bigger hexagonal fibres become visible. There are no evidence about Ca-sulphoaluminate hydrates tubular fibres seen in Portland cement [14]. These hexagonal phases are clearly metastable [15] and the natural development of the reaction should go into the formation of ettringite and C_3HA_6,effectively observed after 60 days of hydration. Actually, at low pH platelets of C_2AH_8 can precipitate while at high pH values it is expected to find a mix of C_4AH_{19} and $Ca(OH)_2$.

Jensen, Christensen e Hanson [16] tried to characterize the aluminate in-situ hydration in hydrothermal conditions. They used C_3A (but also CA and C_2A) to produce C_2AH_8 and C_4AH_{19}. The principal chemical reaction responsible for this transformation is:

$$2C_3A + 27H \rightarrow C_2AH_8 + C_4AH_{19} \tag{1.4}$$

Actually, C_3A hydration lead to the formation of different compounds with general formula C_4AH_x ($x = 11$, 13 or 19) and amorphous Al-hydroxides [16]. X-ray powder diffraction data C_2AH_8 – C_4AH_{19} are detectable until the temperature is below 70°C; over this temperature C_3AH_6 (hydrogarnet) become the stable phase also caused by the presence of amorphous Al-hydroxides:

$$3C_4AH_{19} + Al(OH)_3 \rightarrow 4C_3AH_6 + 36H \tag{1.5}$$

$$2C_2AH_8 \rightarrow C_4AH_{13} + 2Al(OH)_3 \tag{1.6}$$

In their experiments Jensen et al. [16] state that to have hydrogarnet the intermediate step, with formation of C_2AH_x and C_4AH_x, is required. Moreover, amorphous gibbsite $Al(OH)_3$ is necessary to complete the transformation to hydrogarnet.

Matschei, Lothenbach and Glasser [11] reviewed the composition, synthesis and stability of AFm phases, excluding iron-bearing AFm. In literature the solid solution within various AFm phases is still debated, especially for such phases containing OH and SO_4. Several authors claim the complete solid solution [15], [17–19], some others describe only a partial solid solution [20–23] while Zhang [24] states there is no solid solution at long hydration times. Within the complete solid solution supporters there are some incompatibilities, for example Turriziani [18] support this theory only on the basis of optical microscopy, in some ways ignoring his x-ray data. Zhang [24] states that, even after long hydration times, no solid solution is clearly detectable even if this hypothesis cannot be excluded when applied to the first steps of hydration process. Matschei et al. [11] start from the hypothesis of a solid solution, even partial, that lasts for the whole experiment time and sufficient to produce an hydration model. Purpose of that work is to verify if a real solid solution can occur on $C_4A\check{S}H_x$ – C_4AH_x, $C_4A\check{S}H_x$ – $C_4A\check{C}H_x$, $C_4A\check{C}H_x$ – C_4AH_x systems. In the first case they considered the general compound C_4AH_x, since both x = 13 and x = 19 can precipitate. A miscibility gap between these 2 compounds have already been described [11] at constant pH values. In the second case no solid solution can form; in the third case a partial solid solution occurs. Analyzing further details, authors came to the conclusion that AFm phases bearing $(OH)^-$, $(SO_4)^{2-}$ and $(CO_3)^{2-}$ as principal anions are not completely combinable [11]. Furthermore, some thermodynamic parameters have been calculated during the work because literature lacked these parameters. Even if it is not specifically mentioned, iron leads to a slight miscibility between AFm phases bearing $(OH)^-$, $(SO_4)^{2-}$ and $(CO_3)^{2-}$.

Christensen, Jensen, Scarlett, Madsen and Hanson [25] provide a more precise explanation about the possible aluminate hydration products, either as single phases or in a clinker. They identified firstly C_4AH_{19} rather than C_2AH_8 using the intensity ratio between the first two diffraction peaks. At 55°C they observed the maximum C_4AH_{19} content (that remain stable till > 170°C) when more stable products as C_4AH_{12} and C_3AH_6 starts to appear. Hydrogarnet can also derive from a the transformation of $C_{12}A_7$, passing through C_4AH_{19} as intermediate step. The investigation of aluminates present in the clinker the first hydration products were C_4AH_{19} and C_4AH_{13} [25]. After the decomposition of C_4AH_{13}, which grows over C_4AH_{19}, C_4AH_{11} starts to grow. C_3AH_6 stands in 43°C – 170°C temperature range and grows consuming C_4AH_{19} and C_4AH_{13} [25]. C_4AH_{19} shows a multi-layered structure: the water loss from such layers lead to the formation of C_4AH_{13}, C_4AH_{11}, C_4AH_7 [25, 26]. An amorphous phase can be also qualitatively detected looking at the background values visible on diffraction data, mostly at low 2θ values, probably responsible for the transformation of all the hydrated aluminates into C_3AH_6 [25]. Christensen, Jensen and Hanson [27] studied the formation of ettringite and monosulphoaluminate in the CaO – Al_2O_3 – $CaSO_4$ – H_2O system. From literature, in this system ettringite can grow very rapidly [27, 28]. Reaction products AFm-14 and C_4AH_{19} are produced only when ettringite starts to dissolve and their content depends on gypsum initial amount: this limit the temperature range at which C_4AH_{19} can precipitate [27]. AFm-14 is apparently stable for temperature > 170°C; C_3AH_6 grows typically at 85°C and remains stable up to > 170°C [27]. Ettringite has been shown hydrating a white Portland cement at T > 48°C, after the conversion of AFm-14 caused by increased temperature.

If we then consider a Portland cement with SO_3 content of 3.37%, ettringite is stable in the temperature range 25°C < T < 75°C [29]. Ettringite precipitates in CaO – Al_2O_3 – $CaSO_4$ only if sufficient C3A and gypsum content are present. If this condition is not satisfied, ettringite already formed will be converted into monosulphate when gypsum is completely depleted. If C3A and gypsum are unsufficient from the beginning, monosulphate is the first phase which precipitates (AFm-14). The intermediate aluminate hydrate formed has been detected as C4AH19 [27].

1.4. Tricalcium Silicate

1.4.1. Crystal Structure

C_3S is a synthetic phase that crystallize during the industrial process of clinker production. The crystal structure of the most abundant cement phase is very complex and many researchers are still involved in refining existent structures or to solve new ones. Due to the different thermal regime suffered by raw materials, different polymorphs can form during the clinkerization process. Three types of polymorphs can form: triclinic, monoclinic and rhombohedral. Such polymorphs crystallize undergoing the following temperature regime [5]: T_1 620°C→ T_2 920°C→ T_3 980°C→ M_1 990°C→ M_2 1060°C→ M_3 1070°C→ R. All of these phase transitions are temperature-reversible. The more stable polymorph seems to be T_1 but, since C_3S occurs mostly as an impure phase (Mg, Al, Zn can enter and stabilize the structure [30]), at room temperature the most frequent polymorphs at become M_1 and M_3. When impurities substitute part of the original cations, we call C_3S as Alite

The first crystal structure determination was performed by Jeffery [31]: he showed that T_1, M_3 and R had closely similar structures and he was able to solve them using an approximate pseudo-structure with space group R 3 m. Ca^{2+}, $(SiO_4)^{4-}$ and O^{2-} are the constituent ions, the latter bond only to six Ca^{2+}, as in CaO. Several works aimed at improving the knowledge of C_3S crystal structure: the known structures are all closely similar as regards the positions of the Ca^{2+}, O^{2-} ions and Si atoms, but differ markedly in the orientations of the $(SiO_4)^{4-}$ tetrahedra, which in some case are disordered [5], [30]. For each polymorph, there are different crystallographic Ca^{2+} sites with different coordination; sometimes, for each given site, the coordination number varies because of the differences in $(SiO_4)^{4-}$ tetrahedra orientations.

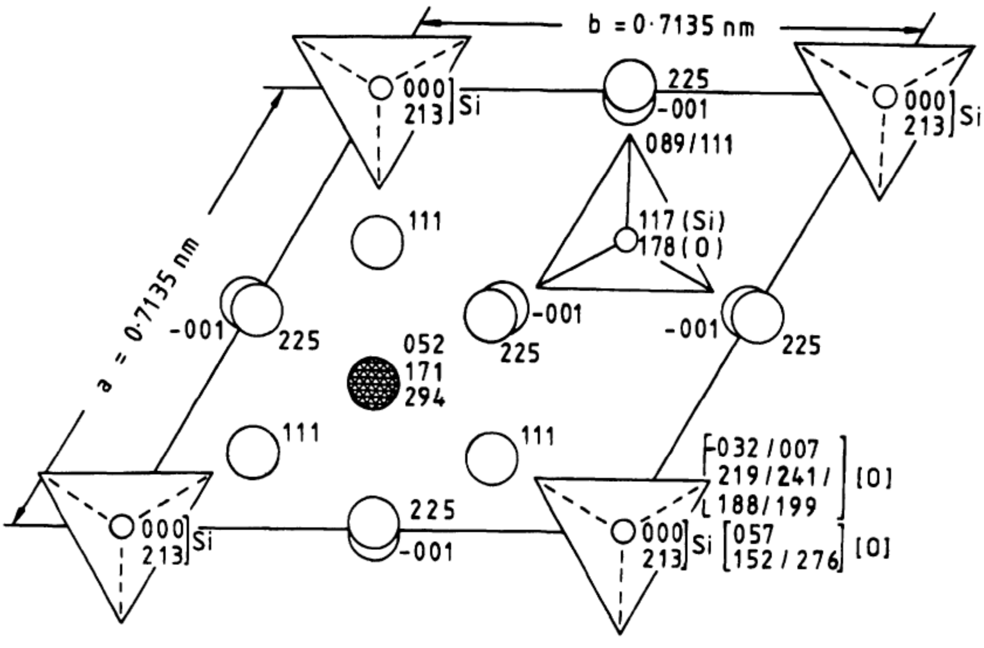

Figure 1.6: Crystal structure of R modification of C_3S, showing Ca atoms (large open circles), Si atoms (small open circles), oxide ions (large hatched circle) and oxygen tetrahedra (triangles). Heights of atoms are in thousandths of the cell height (c = 2-5586nm), slashes denoting statistical alternatives [5].

During the years, data coming from single crystal have been joined with improved powder diffraction data to have a summary table on crystallographic parameters of all the known structures, from pure C_3S to different kind of Alite.

Polymorph	Symmetry group	Type of data	a (Å)	b (Å)	c (Å)	α (°)	β (°)	γ (°)
R	*R3m*	SC	7.135	7.135	25.586	90	90	120
		SC	7.0567	7.0567	24.974			
M_3	*Cm*	SC	33.083	7.027	18.499	90	94.12	90
	Cm	PWD/SR	33.1078	7.0355	18.5211	90	94.137	90
	Cm	PWD	33.0577	7.0330	18.5179	90	94.18	90
M_3: <M>	*Cm*	SC	12.235	7.073	9.298	90	116.31	90
M_2	(pOH)	PWD	12.342	7.143	25.434	90	90	90
		PWD	12.333	7.137	25.442			
M_1	(pOH)	PWD	12.332	7.142	25.420	90	89.85	90
	Pc	PWD	27.8736	7.0590	12.2575	90	116.030	90
T_3	(pOH)	PWD	24.633	14.290	25.412	90.06	89.86	89.91
T_3: <T>	$P\bar{1}$	PWD/SR	11.6389	14.1716	13.6434	104.982	94.622	90.107
T_2	(pOH)	PWD	24.528	14.270	25.298	89.98	89.75	89.82
T_2: <T>	$P\bar{1}$	PWD/SR	11.7417	14.2785	13.7732	105.129	94.415	89.889
T_1	(pOH)	PWD	24.398	14.212	25.103	89.91	89.69	89.69
<T>	$P\bar{1}$	SC	11.67	14.24	13.72	105.5	94.33	90.0

Table 1.7: summary table on C_3S crystallographic parameters [30].

1.4.2. Hydration products

C_3S hydration can be expressed as a quite simple reaction, in which tricalcium silicate dissolves to produce Ca-Si hydrates (C-S-H) and portlandite. The following reaction explain this dissolution:

$$3(CaO)_3(SiO_2) + 16H_2O \rightarrow 4Ca(OH)_2 + 3(CaO)_{1.7}(SiO_2)\square 4H_2O \qquad (1.7)$$

In spite of this apparent simplicity, the C-S-H is a wide family of very different products, crystalline only at the nanoscale, expressing a huge stoichiometry and structure variability. Generally speaking, crystalline C-S-H are characterized by a layer structure composed of silicate tetrahedra that are coordinated to Ca^{2+} in a repetitive pattern as to form a kinked pattern [32]. Such pattern is composed of three tetrahedra, two of them sharing a O-O edge (Paired tetrahedra) with the central Ca-O octahedron and linked together by the third tetrahedron (Bridge tetrahedron). Intensive research is justified by its importance for cement and concrete science: C-S-H are the main responsible for mechanical strength performance of cements. Being aware of the different microstructures can give a definitive insight on the mechanisms which dominate the mechanical strength increase in mature cements and concretes.

An extensive and exhaustive review has been written by Richardson [32], where he gathered synthetic and natural C-S-H into 7 groups, depending on the crystal structure type identified: Wollastonite, Tobermorite, Jennite, Gyrolite, γ-C_2S, various phases, various phases at high temperature. It is underlined that C-S-H can bear also Na, K, Al, F and Mn, providing a further complexity on the comprehension of the structures. In the review the author stressed the attention to 2 of the most implemented models, Tobermorite and Tobermorite-Jennite, mostly because the structure of 1.4 nm Tobermorite has been solved by Merlino et al. [33, 34, 35] and becomes a significant base for any structural model.

1.4.3. State of the art about C_3S – Gypsum hydration

In despite of C_3S + gypsum hydration does not show any clear hydration product, several experiments have been performed to understand the interactions between C_3S hydration products (especially C-S-H) and gypsum. Authors reports about different theories and results, which are briefly summarized in next paragraphs.

Fu et al. [36] investigated the role of C-S-H as reservoir of sulphate anions for delayed ettringite formation with a particular insight into the temperature effect on the sorption process. Practically, they demonstrated that C-S-H acts as a source for $(SO_4)^{2-}$ even when all gypsum is depleted from the solution: introducing C_3A in the hydrated C_3S solution led to the precipitation of ettringite. Such precipitation is followed by a consumption and a secondary precipitation of ettringite itself. C-S-H gel adsorbs $(SO_4)^{2-}$ anions faster at higher temperatures but releasing slower at long hydration age (6 months), leading to retarded ettringite formation.

Gunay et al. [37] focused the attention on the optimum gypsum quantity to add to a cementitious system in order to have the best compressive strength values. The interactions between C_3A and gypsum are well described in literature [38], as well as some theories are proposed for C_3S + C_3A interactions [33, 34], C_3S hydration in the presence of gypsum is not so well investigated, especially if this hydration process is then related to mechanical strength properties.

Gypsum increases the growth rates of C-S-H and its permeability leading to a greater degree of hydration for the same curing time [37] of a paste composed only by hydrating C_3S: this is well explained by an anisotropic growth model. An optimum gypsum content is established to be true only for early age (3 days) mechanical strength, when a water/(C_3S + gypsum) ratio remain constant because an increase of the degree of hydration is observed at early ages when gypsum is added to the C_3S hydrating system. When water/C_3S ratio is considered, a lower mechanical strength is detected at 28 days, even if the degree of hydration remains constant. Considering that all the sulphate is being adsorbed at 28 days [41], the loss on mechanical strength is described by measuring the C-S-H interparticle forces, which are smaller than that measured for C-S-H with no sulphate adsorbed, resulting in a lowering of the measured compressive strength.

They investigated the alite hydration (since it is responsible for the 80% of cement hydration) compared to type I, II and III Portland cements and then alite plus gypsum mixes, at two different fineness grades. From the determination of time setting using ASTM C266 and C186 methods they found that alite hydrated alone shows delayed initial time setting in respect of Portland cements, while these timings become comparable when 3% of gypsum is added and an acceleration become visible: 3 hours for Portland cement, 8.5 hours for alite, 3.5 hours for alite + 3% gypsum. A reason for such a different behaviour is given claiming C_3A acting as an accelerator for setting in Portland cements. It is not the same story when 6% of gypsum is put in, because even if an acceleration is still detectable, this is not of the same amount: 5 hours of initial time setting. This could be due to more than an optimum gypsum quantity present in the system [42]. Another important evidence come from the heat of hydration measure, which revealed how alite + gypsum showed an higher heat release in respect to Portland cements. X-ray diffraction data confirmed that alite hydrates faster when gypsum is added, because the alite most intense peak shows a lower intensity in alite + 3% gypsum mix while with 6% gypsum the diminution of intensity is smaller. The free lime content shows an increase when 3% gypsum is put in, in respect to the amount detected when only alite is hydrated. Early strengths of mortars and concretes made with alite cements were generally higher than Portland cements of the same fineness, however the behaviour becomes opposite at later ages. Addition of 6% of gypsum to alite cements caused significant deterioration in the strength characteristic [42].

Menetrier et al. [43] report again previous literature experiments, where a certain amount of $(SO_4)^{2-}$ can be incorporated into C-S-H, the main C_3S hydration product. From their experiments, the CaO concentration in solution for C_3S + gypsum system reaches the saturation level considerably before the C_3S hydrated alone: with gypsum, the C_3S dissolution rate increases during the acceleration period. This led to the observation of different C-S-H shapes: with gypsum Ca-Si hydrates morphology are more similar to that observed in a lime saturated solution (since gypsum dissolves and Ca^{2+} saturation is reached faster, this is quite reasonable) than shapes observed when C_3S is hydrated in deionized water. From EDS microanalysis, authors suggest that some (SO4)2- can be incorporated somehow into C-S-H [43], which is clearly in contrast with the adsorption theory [37].

Barbarulo et al. [44] propose a different approach, studying mixes of C-S-H and ettringite at different temperatures, evaluating the kinetics of ettringite precipitation and the importance of sulphate bound to C-S-H. In a preliminary study, from the same authors, they found that sulphate binding to C-S-H increases with the sulphate concentration in solution but also with increasing Ca/Si ratio in C-S-H. First of all it can be clearly seen that ettringite dissolution is favoured at high temperature (85°C) instead of low temperature (20°C). Before ettringite precipitation, no other sulphate-bearing crystalline phase can be detected by XRD. This result is a good indication that below ettringite equilibrium, sulphate present in the solid phase is bound to the C-S-H only [44]. Even if these are synthetic systems, some discussion are useful: the amount of sulphate anions bound to C-S-H can be measured and the authors report that 13% of the total sulphate initially present in the cement would be fixed by C-S-H at 20°C. This values increases to 26% at 85°C. These are the maximum quantity that can be bound for a Ca/Si = 1.5, as chosen by the researchers when synthetizing C-S-H. At high temperature (85°C) ettringite introduced in the system is completely dissolved and part of the sulphate is incorporated into C-S-H in a non-negligible quantity. When the return kinetics are considered (85°C → 20°C), C-S-H releases $(SO_4)^{2-}$ to precipitate again ettringite, showing a very slow precipitation rate (more than 1 month to complete the reaction). This model seems to be quite useful to explain the undesired effect of Delayed Ettringite Formation (DEF) in steam-cured cements.

Bentur [45] describe the effect of different amount of gypsum in the hydration of C_3S pastes. Mainly from x-ray data, he points out the existence of an optimum quantity of gypsum, because the degree of hydration and compressive strength show a maximum at a certain gypsum quantity. Such quantity decreases with ageing of the material. Looking at the plot of degree of hydration vs. compressive strength, it becomes evident that gypsum has a dominant role, in respect to C_3S pastes: when gypsum is added, degree of hydration increases in respect to pure C_3S paste. This can be due to the quantity and quality of C-S-H gel and its intrinsic strength: the optimum gypsum content is the value at which the optimum combination of quantity and quality occurs. As hydration proceeds, the quality factor becomes more dominant and, as a result, the optimum gypsum content decreases [45].

Brown el al. [46] studied the effect of different salts dissolved in water in C_3S hydration. Salts involved were $CaCl_2$, NaOH, NaCl, $CaSO_4$. Generally speaking, all the dissolved salts provoked an acceleration in C3S hydration, possibly due to hydroxyl suppression mainly caused by $Ca(OH)_2$ precipitation. Considering only $CaSO_4$, from calorimetric measurements authors detected an initial delaying in hydration (within 5 hours) and later an increase in the C_3S dissolution rate. Researchers cited that the role of anions in accelerating C_3S hydration may be related to their ability to flocculate hydrophilic colloids, that coupled with the morphological differences on C-S-H seen in $CaCl_2$ saturated solutions, led to the conclusion the depression of hydroxyl ion concentration in solution may be a contributing factor to explain C_3S hydration acceleration [46].

1.5. State Of The Art About C_3S – C_3A – Gypsum Blends

Since the main object of my Ph.D. project is to provide insights in C_3S – C_3A – Gypsum simplified cement systems, a general overview on the literature can be a solid standpoint to make further considerations on new data.

As previously mentioned, Portland cement is a very complex system that undergoes several transformations when mixed with water. It is well known [5] that the main actors of cement hydration at early age are tricalcium silicate and tricalcium aluminate, with gypsum especially that regulates the so-called set timings. In spite of these evidence, not many authors decided in the past to get rid of minor components and those phases which reacts at later age (C_2S and C_4AF). One of them was Tenoutasse [40], who studied the effect of calcium chloride and calcium sulphate addition to C_3S and C_3A by means of x-ray diffraction and isothermal calorimetry. He found that different amount of gypsum influence not only the time of appearance of thermal phenomenon related to C_3A dissolution but also the amplitude of the peak: with increasing gypsum concentration the rate of hydration decreases. When this thermal peak occurs, gypsum is completely depleted [40] and so the time needed for complete consumption can be measured. Adding 5%, 15%, 17.5%, 20% of gypsum to C_3A the time occurred to consume all the gypsum is linear dependent to the square of initial gypsum content: this suggests that it reacts by a diffusion mechanism [40]. He states that during C_3A dissolution in presence of gypsum, the only hydration product formed is Ettringite following the reaction:

$$C_3A + CaSO_4 + 32H_2O \rightarrow C_3A\cdot CaSO_4\cdot 32H_2O \qquad (1.8)$$

But when all the gypsum has been dissolved, the remaining C_3A is hydrated to give C_4AH_{13} and ettringite is converted into monosulphoaluminate:

$$C_3A\cdot CaSO_4\cdot 32H_2O + 2C_3A\cdot Ca(OH)_2\cdot 12H_2O \rightarrow C_3A\cdot CaSO_4\cdot 12H_2O + 20H_2O + 2CH_2 \quad (1.9)$$

Indeed, the author claims the existence of a solid solution between monosulphoaluminate and C_4AH_{13}.

C_3S hydration is also influenced by the addition of C_3A: in fact, it becomes slower than the hydration of C_3S alone. From calorimetric data, when the peak related to C_3A dissolution lies before the peak related to C_3S, the latter is greatly retarded and showing a slow rate of hydration [40].

Garrault et al. [39] studied the Alite – C_3A – Gy system in order to evaluate Alite hydration and mechanical strength. Firstly focusing on Alite – C_3A hydration (without any sulphate addiction), they verified that the hydration of C_3A is not modified by Alite. Furthermore, they state that Al ions have a negative effect on the growth rate of C-S-H but also that AFm can give a useful surface for C-S-H growth. As a fact, it has been shown that the mechanical efficiency decreases when a tricalcium silicate paste is hydrated in a solution containing aluminate ions [47]. At early ages the storage modulus is higher when C_3A is present more than 5% in the mix: AFm phases are the main responsible for the stiffening of the paste. Considering Alite-C_3A-Gy hydration, authors have seen a slowing down of AFm formation when both alite and gypsum are present and this is not observed with only gypsum or with only alite. Here again a thermal peak due to all sulphate consumption is observed and the greater the quantity of gypsum, the later the time of appearance of such peak. Finally, when C3A alone is hydrated with gypsum, the thermal phenomenon related to sulphate depletion occurs before the silicate hydration peak, leading to a delayed ettringite formation. Concerning alite hydration, it is practically unchanged in the presence of C3A and gypsum, even if a slower hydration rate is observed (in respect to C3A alone). In the presence of gypsum there is formation of ettringite in place of C-A-H and ettringite does not seem to act as a precipitation surface for C-S-H [39]. In Alite-C_3A-Gy systems the mechanical efficiency of C-S-H increases with increasing gypsum and the effect is emphasized also with C_3A increase. A possible explanation of the increase of mechanical efficiency is given by the presence of solid gypsum when this quantity is measured. In Alite-C_3A-Gypsum the hydration path seems very similar to that of alite: C_3A seems not to affect the hydration process and ettringite does not interact with C-S-H nucleation and growth.

More recently, Hesse et al. [48] worked on a synthetic cement made of polyphase clinker of C_3S, C_3A and a sulphate carrier. They used especially XRD and isothermal calorimetry to investigate this material. From calorimetric data, the authors proposed an already published explanation for the induction period: this period is a result of slowdown of C_3A dissolution due to the increase of sulphate content in the pore solution. Furthermore, they claim for the existence of an amorphous aluminate phase which can serve as a reservoir for ettringite formation when the sulphate carrier is completely dissolved. The constant rate of formation during the acceleration period can be attributed to these amorphous phases consumption. When the pore solution becomes free of sulphate ions, ettringite should start the conversion to monosulphate, but this is not visible at 23°C and ettringite remains stable even when no sulphate is available to grow [48].

Also C_3S hydration contribute to the onset of the induction period: Julliand et al. [49] concluded that the induction period is mainly controlled by alite hydration. Thomas et al. [50] state that the duration of the period is expression of the availability of reactive nuclei. With the addition of synthetic C-S-H seeds they have shown a shortening of the dormant period.

In the last few days, a very important work has been published by Quennoz et al. [51], who worked on alite and C_3A-gypsum hydration on model cements. The hydration kinetics have been measured by means of XRD, SEM and isothermal calorimetry. They take into account the concept of "proper sulphation" content: when the gypsum content is too low, precipitation of monosulphate due to C_3A dissolution occurs before alite reaction, which is delayed and lowered in consequence. Undersulphation is still a matter of interest because certain cements properly sulphated when hydrated with water become undersulphated when additives are used [51]. Minard [47] found that C_3S hydration was observed to be accelerated in presence of gypsum while the alite in decelerated when Al ions are present into the solution. More generally speaking, the heat evolution of alite-

C_3A-gypsum systems is very influenced by gypsum content, alternatively behaving as undersulphated (aluminate reaction before silicate reaction) or properly sulphated (silicate reaction first, aluminate reaction second). In this last case, alite hydration rate has been observed to be faster during the acceleration period than the same period of plain alite hydration [51]. Studying alite-water and alite-gypsum-water systems, the authors related this acceleratory effect to the entrance of gypsum in the hydration process. Minard [47] observed a similar effect for C_3S and suggested a modification on C-S-H growth due to the absorption of $(SO_4)^{2-}$ that increases the nucleation and growth velocity of Ca-Si hydrates. On the other hand, the hydration of alite is retarded in the presence of gypsum, but this is otherwise explained evoking a negative effect of Al on the rate of hydration. Also Garrault [52] reported Al-bearing alite may be at the origin of the difference in the reaction rate observed between pure C_3S and alite pastes. Quennoz detected sulphate ions absorbed on C-S-H of both alite and C_3S by means of energy-dispersive x-ray spectroscopy (EDS) which discard the gypsum effect on acceleration and support the Al suppression effect: alite hydration rate is slowed down by the presence of aluminium in solution. In the presence of gypsum, such aluminium is removed from solution and incorporated into ettringite, resulting in an acceleration of alite hydration rate. From isothermal calorimetry, in undersulphated systems the alite hydration shows a very broad peak: this should be the effect of Al in the solution, but the physics of the phenomenon is not completely clear. Possible explanations given are: 1) the previous dissolution of some C_3A and consequent precipitation of Ca-Al hydrates removes space for nucleation and growth of C-S-H; 2) the presence of Al in pore solution or incorporated in C-S-H structure. EDS measurements on C-S-H precipitated in undersulphated systems revealed an higher Al content than C-S-H grown in proper sulphated systems, supporting the Al negative effect [51].

Another possible effect of gypsum is that it leads to the highest strength values at early age acting on alite much more than on C_3A [51].

The presence of alite in C_3A-gypsum system changes the time of appearance of the thermal peak due to aluminate reaction: for the same C_3A/gypsum ratio it is suggested that about 17% of the added gypsum is not available for the reaction with C_3A. This peak is usually very sharp and intense for the pure C_3A-gypsum system but it becomes broader and lower with increasing gypsum in model cements. A possible justification is given considering the free specific surface: in C_3A-gypsum system the free specific surface is higher than in alite-C_3A-gypsum systems, where the matrix is filled up by C-S-H and CH, at the time of corresponding to aluminate reaction [51]. For such reasons the peak is lower and broader.

The EDS analysis on C-S-H shell associated to ettringite formation, during the deceleration period revealed a desorption of sulphate anions from C-S-H that are then available to form more ettringite after gypsum depletion.

Talking about the temperature effect, the authors evaluated cement kinetics at different temperature, in order to obtain reliable activation energy values. They observed a typical Arrhenius effect: reactions occur faster with increasing temperature and the peak intensities are higher. Another interesting feature it that the "sulphation feature" of each cement is a temperature-dependent variable, because an undersulphated cement at 20°C become proper sulphated at 15°C [51]. This means that cements can be considered "properly sulphated" only within a certain range of temperature values. Such a behaviour can be explained with the higher sensitivity to temperature of aluminate reaction, in respect to silicate reaction, which seems to be less affected to temperature changes. The activation energy of alite is higher when gypsum is present in the system, confirming the sulphate acting as a sink for Al which leads to ettringite precipitation. Values of 35 KJ/mol for alite and 40-45 KJ/mol for cements are similar to those reported in the literature [53, 54]. Activation energy for aluminate reaction seems to show an increasing trend with increasing gypsum quantity; moreover, absolute values are higher than those of alite, confirming an higher temperature sensitivity than alite reaction.

When I will discuss my data, we will see how there are some agreement with published theories and data. But such agreement is not complete and further discussion is needed to have an exhaustive comprehension of the kinetic processes.

REFERENCES

[1] F. Ridi, E. Fratini, and P. Baglioni, “Cement: a two thousand year old nano-colloid.,” *Journal of colloid and interface science*, vol. 357, no. 2, pp. 255–64, May 2011.

[2] S. Sismondo, *An Introduction to Science and Technology Studies*, 2nd editio. 2009, p. 256.

[3] C. Mukerji, *Impossible engineering: technology and territoriality on the Canal du Midi*, Illustrate. 2009, p. 121.

[4] P. C. Hewlett, *Lea's Chemistry of Cement and Concrete*, Fourth Edi., no. January. 2010.

[5] H. F. W. Taylor, *Cement chemistry*. Thomas Telford, 1997.

[6] H. F. W. Taylor, *Cement chemistry*, Second Edi. Thomas Telford, 1997.

[7] V. K. Peterson, “Diffraction Investigations of Cement Clinker and Tricalcium Silicate using Rietveld Analysis,” University of Technology, Sydney, 2003.

[8] Y. Takeuchi, F. Nishi, and I. Maki, “Crystal-chemical characterization of the 3 CaO · Al2O3–Na2O solid-solution series,” *Zeitschrift für Kristallographie*, vol. 152, no. 3–4, pp. 259–307, 1980.

[9] S. J. Ahmed, D. Glasser, and H. F. W. Taylor, “No Title,” in *International Symposium on the Chemistry of Cement, ISCC*, 1969, p. 118.

[10] S. J. AHMED and H. F. W. TAYLOR, “Crystal Structures of the Lamellar Calcium Aluminate Hydrates,” *Nature*, vol. 215, no. 5101, pp. 622–623, Aug. 1967.

[11] T. Matschei, B. Lothenbach, and F. Glasser, “The AFm phase in Portland cement,” *Cement and Concrete Research*, vol. 37, no. 2, pp. 118–130, Feb. 2007.

[12] L. J. Strumble, “No Title,” in *8th International Conference on the Chemistry of Cement, ICCC*, 1986, p. 582.

[13] E. Breval, “C3A hydration,” *Cement and Concrete Research*, vol. 6, no. 1, pp. 129–137, 1976.

[14] C. J. Hampson and J. E. Bailey, “The microstructure of the hydration products of the tricalcium aluminate in the presence of gypsum,” *Journal of Materials Science*, vol. 18, pp. 402–410, 1983.

[15] F. E. Jones, “The Quaternary System CaO–Al2O3–CaSO4–H2O at 25°C. Equilibria with Crystalline Al2O3–3H2O, Alumina Gel, and Solid Solution,” *Journal of Physical Chemistry*, vol. 48, no. 6, pp. 311–356, 1944.

[16] T. R. Jensen, A. N. Christensen, and J. C. Hanson, “Hydrotermal transformation of the calcium aluminium oxide hydrates CaAl2O4•10H2O and Ca2Al2O5•8H2O to Ca3Al2(OH)12 investigated by in situ synchrotron X-ray powder diffraction,” *Cement and Concrete Research*, pp. 2300–2309, 2005.

[17] J. D’Ans and H. Eick, “Das System CaO – Al2O3 – CaSO4 – H2O bei 20°C,” *Zement-Kalk-Gips*, vol. 6, no. 9, pp. 302–311, 1953.

[18] R. Turriziani and G. Schippa, “Riconoscimento all’ATD ed ai raggi X dei solidi quaternari CaO – Al2O3 – CaSO4 – H2O,” *La ricerca scientifica*, vol. 24, no. 11, pp. 2356–2363, 1955.

[19] G. L. Kalousek, “Sulfoaluminates of calcium as stable and metastable phases, and a study of a portion of the five-component system CaO – SO3 – Al2O3 – Na2O – H2O at 25°C.,” University of Maryland, 1941.

[20] M. H. Roberts, “Calcium aluminate hydrates and related basic salt solid solutions,” in *V International Symposium on the Chemistry of cements, vol II*, 1969, pp. 104–117.

[21] P. Seiligmann and N. R. Greening, “Phase equilibria of cement-water,” in *V International Symposium on the Chemistry of cements, vol II*, 1969, pp. 179–200.

[22] H. Poelmann, “Solid solution in the system 3CaO•Al2O3•CaSO4•aq - 3CaO•Al2O3•Ca(OH)2•aq,” *Neues Jahrbuch fur Mineralogie. Abhandlungen*, vol. 161, pp. 27–41, 1969.

[23] F. Glasser, A. Kindness, and S. Stronach, "Stability and solubility relationships in AFm phases: Part I. Chloride, sulfate and hydroxide," *Cement and Concrete Research*, vol. 29, pp. 861–866, 1999.

[24] M. Zhang, "Incorporation of Oxyanionic B, Cr, Mo and Se into hydrocalumite and ettringite: Application to cementitious system," University of Waterloo, 2000.

[25] A. N. Christensen, T. R. Jensen, N. V. Y. Scarlett, I. C. Madsen, and J. C. Hanson, "Hydrolysis of Pure and Sodium Substituted Calcium Aluminates and Cement Clinker Components Investigated by in Situ Synchrotron X-ray Powder Diffraction," *Journal of American Ceramic Society*, vol. 87, no. 8, pp. 1488–1493, 2004.

[26] E. Aruja, "Unit cell and Space-Group Determination of Tetra- and di-Calcium Aluminate Hydrates," *Acta Crystallographica*, vol. 13, p. 1018, 1960.

[27] A. N. Christensen, T. R. Jensen, and J. C. Hanson, "Formation of ettringite, Ca6Al2(SO4)3•26H2O, AFt, e monosulfate, Ca4Al2O6(SO4)•14H2O, AFm-14, in hydrothermal hydration of Portland cement and of calcium aluminium oxide-calcium sulfate dihydrate mixtures studied by in situ synchrotron X-ray powder diffra," *Journal of Solid State Chemistry*, vol. 177, pp. 1944–1951, 2004.

[28] P. Barnes, X. Turrillas, A. C. Jupe, S. L. Colston, D. O'Connor, R. J. Cernik, P. Livesey, C. Hall, D. Bates, and R. Dennis, "Applied crystallography solutions to problems in industrial solid-state chemistry. Case examples with ceramics, cements and zeolites," *Journal of the Chemical Society, Faraday Transactions*, vol. 92, no. 12, p. 2187, 1996.

[29] A. Nørlund Christensen, N. V. Y. Scarlett, I. C. Madsen, T. René Jensen, and J. C. Hanson, "Real time study of cement and clinker phases hydration," *Dalton Transactions*, no. 8, pp. 1529–1536, Apr. 2003.

[30] M.-N. de Noirfontaine, M. Courtial, F. Dunstetter, G. Gasecki, and M. Signes-Frehel, "Tricalcium silicate Ca3SiO5 superstructure analysis: a route towards the structure of the M1 polymorph," *Zeitschrift für Kristallographie - Crystalline Materials*, vol. 227, no. 2, pp. 102–112, 2011.

[31] J. W. Jeffery, "The crystal structure of tricalcium silicate," *Acta Crystallographica*, vol. 5, p. 26, 1952.

[32] I. G. Richardson, "The calcium silicate hydrates," *Transactions Of The Faraday Society*, vol. 38, pp. 137 – 158, 2008.

[33] S. MERLINO, E. BONACCORSI, and T. ARMBRUSTER, “The real structures of clinotobermorite and tobermorite 9 Å: OD character, polytypes, and structural relationships ,” *European Journal of Mineralogy* , vol. 12 , no. 2 , pp. 411–429.

[34] S. MERLINO, E. BONACCORSI, and T. ARMBRUSTER, “The real structure of tobermorite 11Å: normal and anomalous forms, OD character and polytypic modifications ,” *European Journal of Mineralogy* , vol. 13 , no. 3 , pp. 577–590.

[35] E. Bonaccorsi, S. Merlino, and A. R. Kampf, “The Crystal Structure of Tobermorite 14 Å (Plombierite), a C–S–H Phase,” *Journal of the American Ceramic Society*, vol. 88, no. 3, pp. 505–512, 2005.

[36] Y. Fu, P. Xie, P. Gu, and J. Beaudoin, “Effect of temperature on sulphate adsorption/desorption by tricalcium silicate hydrates,” *Cement and concrete research*, vol. 24, no. 8, pp. 1428–1432, 1994.

[37] S. Gunay, S. Garrault, A. Nonat, and P. Termkhajornkit, “Influence of calcium sulphate on hydration and mechanical strength of tricalcium silicate,” *Unpublished*, 2012.

[38] S. Pourchet, L. Regnaud, J. P. Perez, and A. Nonat, “Cement and Concrete Research Early C 3 A hydration in the presence of different kinds of calcium sulfate,” *Cement and Concrete Research*, vol. 39, no. 11, pp. 989–996, 2009.

[39] S. Garrault, H. Minard, and A. Nonat, “Hydration of silicate phase and mechanical evolution in’alite-tricalcium aluminate-gypsum'complex system,” *12 th International …*, 2007.

[40] N. Tenoutasse, “The Hydratation Mechanism of C3A and C3S in the Presence of Calcium Chloride and Calcium Sulphate,” pp. 372–378, 1969.

[41] Medala, “Etude des interactions entre les phases minerales constituant le ciment Portland et des solutions alcalines concentrees,” Université de Bourgogne, 2005.

[42] P. Mehta, D. Pirtz, and M. Polivka, “Properties of alite cements,” *Cement and concrete research*, pp. 439–450, 1979.

[43] D. Menetrier, I. Jawed, and J. Skalny, “Effect of gypsum on C 3 S hydration,” *Cement and Concrete Research*, vol. I, no. c, pp. 697–701, 1980.

[44] R. Barbarulo, H. Peycelon, and S. Leclercq, "Chemical equilibria between C–S–H and ettringite, at 20 and 85 °C," *Cement and Concrete Research*, vol. 37, no. 8, pp. 1176–1181, Aug. 2007.

[45] A. Bentur, "Effect of Gypsum on the Hydration and Strength of C3S Pastes," *Journal of the American Ceramic Society*, 1976.

[46] P. Brown, C. Harner, and E. Prosen, "The effect of inorganic salts on tricalcium silicate hydration," *Cement and Concrete Research*, vol. 16, pp. 17–22, 1986.

[47] H. Minard, "Etude intégrée des processus d'hydratation, de coagulation, de rigidification et de prise pour un système C3S-C3A-sulfates-alcalins," Université de Bourgogne, 2003.

[48] C. Hesse, F. Goetz-Neunhoeffer, and J. Neubauer, "A new approach in quantitative in-situ XRD of cement pastes: Correlation of heat flow curves with early hydration reactions," *Cement and Concrete Research*, vol. 41, no. 1, pp. 123–128, Jan. 2011.

[49] P. Julliand, E. Gallucci, R. Flatt, and K. L. Scrivener, "Dissolution theory applied to the induction period of in alite hydration," *Cement and Concrete Research*, vol. 40, pp. 831–844, 2010.

[50] J. J. Thomas, H. M. Jennings, and J. J. Chen, "Influence of nucleation seeding on the hydration mechanism s of tricalcium silicate and cement," *Journal of Physical Chemistry C*, vol. 113, pp. 4327–4334, 2009.

[51] A. Quennoz and K. L. Scrivener, "Interactions between alite and C3A-gypsum hydrations in model cements," *Cement and Concrete Research*, vol. 44, pp. 46–54, Feb. 2013.

[52] S. Garrault, A. Nonat, Y. Sallier, and L. Nicoleau, "On the origin of the dormant period of cement hydration," in *13th International Congress on the Chemistry of Cement*, 2011.

[53] L. D'Aloia and G. Chanvillard, "Determining the 'apparent' activation energy of concrete: Ea—numerical simulations of the heat of hydration of cement," *Cement and Concrete Research*, vol. 32, pp. 1277–1289, 2002.

[54] J. Poole, K. Riding, and K. Folliard, "Methods for calculating activation energy for Portland cement," *ACI materials …*, no. 104, 2007.

2. Analytical methods

The aim of this chapter is to describe the analytical methods used during this thesis work.

2.1. X-ray Diffraction

X-ray diffraction (XRD) is an analytical technique based on the x-ray scattering produced when passing through the matter. The scattering phenomenon occurs when x-ray photons interacts with the electrons present in the studying material. Electrons behave as diffusion centers for X radiation of the same wavelength (coherent scattering) or different wavelength (incoherent scattering) of incident radiation. Diffraction is related to the coherent part of the scattering phenomenon: a crystalline solid covered by an x-ray beam produces diffracted x-rays along those directions where all the waves diffused by atoms in the crystal lattice are in phase concordance (constructing interference). To obtain a diffracted beam, certain geometric conditions have to be satisfied and such conditions are well described by Bragg's law:

$$2d_{hkl} \sin \theta = n\lambda$$

Where d_{hkl} is the interplanar distance between a family of *hkl* planes, θ is the angle between the direction of incident x-ray beam and the lattice planes *hkl* (figure 2.1.1), λ is the incident radiation wavelength and n is an integer number. Figure 2.1.1 underlines that the difference in the optical path between parallel and contiguous lattice planes is:

$$AB + BC = 2d_{hkl} \text{ sen } \theta$$

Constructive interference occurs only when the difference path is equal to an integer number of wavelengths, from which diffracted beams (Bragg reflections) are possible just for discrete θ values that satisfy the Bragg equation. In this way, diffraction can be stated as a selective reflection because it occurs only for certain incident angle values between x-rays and lattice planes.

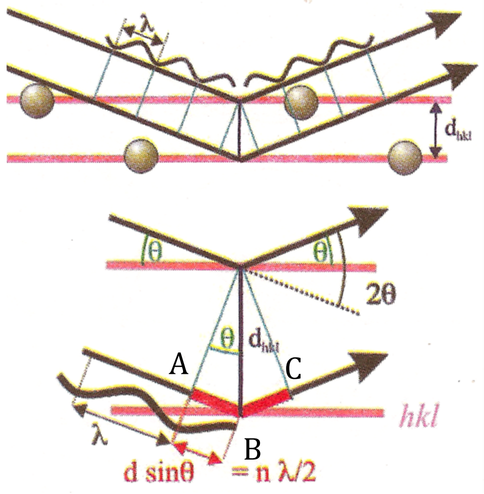

Figure 2.1.1.: coherent scattering of the incident x-rays on a crystalline material and the geometric construction that represents the Bragg's law [redrawn from 1]

The crystal cell parameters can be calculated from the positions of Bragg reflections while the type of atoms and their distribution in crystal cell can be inferred by the measured integrated intensities. The scattering power of any single atom controls the amplitude of scattered waves. The diffusion amplitude depends on the number of electrons that diffuse x-rays at the same time and so the diffusion power is related to the atomic number Z. The diffusion amplitude is defined as the atomic scattering factor, f_s, which is controlled also by the scattering angle, the wavelength and it can be limited by the vibrational movement of atoms in the crystal cell. The highest the thermal motion (atomic motion factor or Debye-Waller Factor) the lowest will be the scattering power. To describe the intensity of a single *hkl* reflection, all atoms that contribute to that single reflection have to be considered. The intensity of a Bragg reflection is proportional the square of the amplitude of the resulting wave produced by the scattering contributions of all atoms in the primitive cell. The amplitude of the resulting wave is described by the magnitude of the structure factor F_{hkl}:

$$I \propto A^2 \equiv |F_{hkl}|^2$$

$$F_{hkl} = \sum_{a=1}^{n} f_s \, t_a \exp[2\pi \, i \, (hx_a + ky_a + lz_a)]$$

where

n = total number of atoms in the primitive cell

f_s = atomic scattering factor

$t_a = \exp[-B_a (\sin^2\theta / \lambda^2)]$ is the atomic motion factor, with

$B_a = 8\pi^2 (u^2)_a$

u^2 = mean square deviation of the a-th atom expressed as $Å^2$ from the equilibrium position x,y,z

$i = \sqrt{-1}$

h, k, l = Miller indices

x_a, y_a, z_a = fraction coordinates of the a-th atom

$2\pi (hx_a + ky_a + lz_a)$ is the phase of the resulting wave.

Experimentally, it is possible to measure the intensity of the resulting wave and subsequently to calculate the amplitude A, but it the phase is not directly accessible. If we were able to solve the phase wave, we would determine the atomic coordinates in the primitive cell and so we would solve the crystal structure.

The problem of the phase in *ab-initio* structure determination is treated and solved using different approaches, e.g. direct methods and Patterson methods.

2.2. X-ray Powder Diffraction (XRPD)

An ideal powder is a polycrystalline material composed by an infinite number of crystallites randomly distributed, with desirable dimension lower than 10 μm. Each crystallite is linked to a reciprocal lattice and the random distribution of many crystallites is the basic condition to observe the diffraction phenomenon for all the reticular planes simultaneously. For each family of reticular planes having the same interplanar distance d, diffracted rays form different cones (Debye-Scherrer cones) of different 4θ angular apertures (figure 2.2.1).

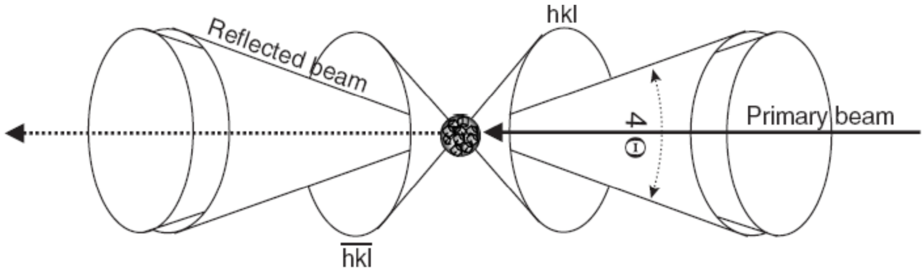

Figure 2.2.1. schematic representation of Debye-Scherrer cones in powder diffraction [readapted from 2].

If the scattered beams are collected in photographic screen (area detector), it can be seen that diffraction is a “portray” of concentric circles which diameters are strictly related to the Bragg diffraction angles. If a cylinder chamber would be employed (Debye chamber), with radius R, measuring the distance S between the circle sectors on the screen and applying the relation:

$$S / 2\pi R = 4\theta / 360°$$

Bragg diffraction angles can be immediately determined for many reticular planes and finally cell parameters can be calculated. Alternative detectors are photon counters (point detectors) used in modern automated diffractometers. Such diffractometers measure step-by-step the selected 2θ range, which is a completely different approach in respect of simultaneous diffraction detection. The result of the diffraction phenomenon for an ideal powder is a distribution of intensities (count of diffracted radiation exiting from a sample) as a function of 2θ, where 2θ is the angle between the direction of the incident beam and the direction of the diffracted beam. Plotting the total measured counts versus the 2θ angle, the so-called diffraction pattern can be observed: above a background noise (coming from air and/or sample holder scattering), peaks of maximum intensities reveal that the Bragg's equations is satisfied for that 2θ angle. The diffraction pattern of a monophasic powder represents the complete map of its microstructure and crystal structure in the reciprocal space. With this technique, the problem of peaks overlapping cannot be avoided as in single crystal diffraction: in fact, all the diffracted intensities bear information on the three dimensions of reciprocal space which are projected along only one direction. To deconvolve the contribution of every single peak, it is necessary to describe properly the shape of the peaks with mathematical expressions. Peaks position (in terms of the interplanar distance *d*) depends on the primitive cell dimensions of the investigated phase and, eventually, on instrumental errors. Peaks intensity depends on the structure factor, which is actually the type of atoms and their distribution in the unit cell, but also on preferred orientations effect and beam polarization effect. Peaks shape is related to instrumental factors and physic features of the sample (strain, dimension of diffraction domains). On the basis of such relations, the detailed study of a diffractogram can give information on: unit cell dimension, space group, atomic structure and dimension of diffracting domains. Particular attention and correction have to be posed on instrumental effects related to different measuring strategies: such effects have to be absolutely corrected.

2.2.1. Experimental geometries in x-ray powder diffraction

An x-ray powder diffractometer is essentially constituted by an x-ray source, a sample holder and a detector that measure diffracted x-rays intensities and positions. Different experimental geometries are obtained varying the reciprocal position of these elements. A first big classification is between reflection and transmission geometries.

In flat-stage reflection geometry measurements, the diffracted radiation is measured as if it were “reflected” by the sample surface (actually such radiation is diffracted by a certain volume, since x-ray can penetrate the sample). In transmission geometry measurements, both for flat-stage or capillary samples, the diffracted radiation, which passes through the sample, is directly detected. This is a fundamental difference because different instrumental effects are produced and such effects have to be treated and corrected in different ways.

Generally speaking, in reflection geometry a divergent beam incident onto the sample results in a convergent diffracted beam; in transmission geometry an incident divergent beam will diverge a lot more when diffracted while an incident convergent beam will result in a more convergent diffracted beam (figure 2.2.2). To increase instrumental resolution (measured peak width), a divergent diffracted beam that reaches the detector is a huge source of problems.

The most diffuse geometry implemented in a laboratory instrument is the so-called “Bragg-Brentano”, described in figure 2.2.3. Such geometry is also called focussing because the divergent incident beam into the sample switch to a diffracted beam focussed on the detector that lies at the intersection between the goniometric circle and the focussing circle. Actually, it should be indicated as parafocusing, because to have a complete focussing diffracted beam the sample should stay always on the focussing circle: this condition would have satisfied only with a curve sample. The focussing circle radius changes accordingly to the variation of 2θ angles while the distances source-sample and sample detector remain constant. During a measurement, source and detector move along the goniometric circle with the same angular velocity. The sample stays at the centre of the goniometric circle, with its surface tangent to the focussing circle.

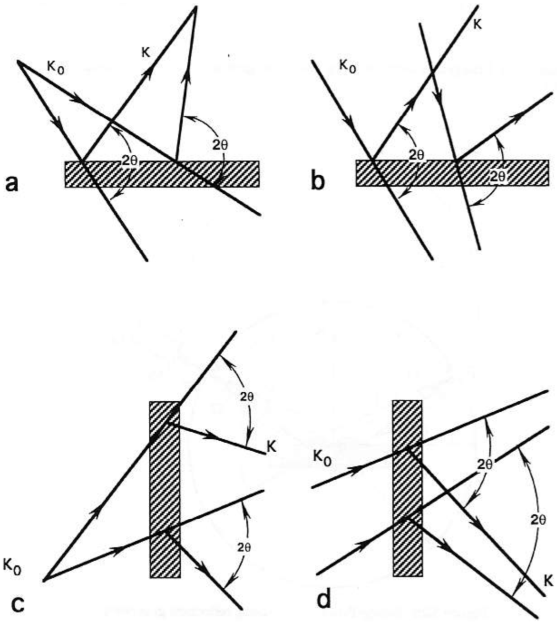

Figure 2.2.2: schematic portray of reflection (a, b) and transmission (c, d) geometries. In transmission geometry, a divergent beam will result in a more divergent diffracted beam. On the contrary, convergent x-rays will be diffracted as more convergent by the sample [2].

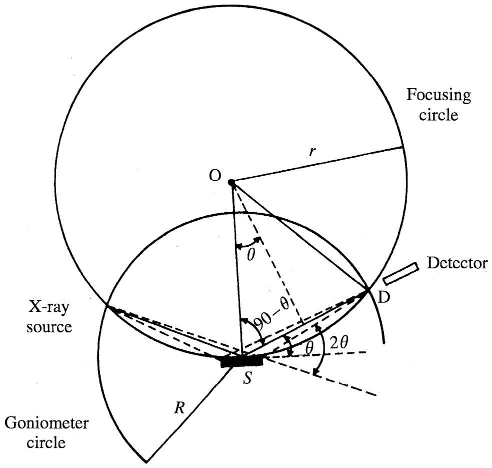

Figure 2.2.3: schematic representation of Bragg-Brentano geometry. All the most important features are plotted with their angular dependence [2].

Bragg-Brentano setup bears the advantage of very good instrumental resolution (narrow peaks) but the disadvantage of double x-ray wavelength ($\alpha_{1,2}$). Strictly monochromatic radiation can be obtained by means of monochromator crystals with a certain loss of intensity. In modern diffractometers, acquisition time is dramatically reduced through linear detectors, which are able to investigate a small 2θ ranges without loosing the improved experimental resolution.

A comparable Bragg-Brentano setup exists also in transmission, where the incident beam has to be convergent: in this way the sample will diffract a convergent beam recordable on the focussing circle by the detector (figure 2.2.4) but to obtain a convergent beam, a monochromatic crystal or a focussing mirror is needed. While in Bragg-Brentano the diffracting planes are parallel to the sample surface, in transmission setup the reticular planes that contributes to the diffraction phenomenon have to be perpendicular to the sample surface.

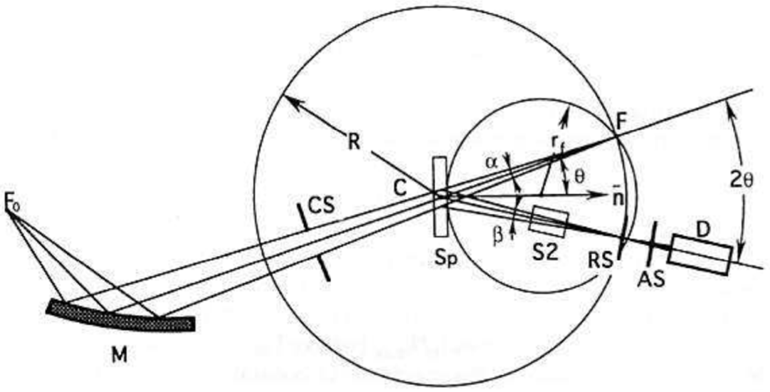

Figure 2.2.4: transmission analogue of Bragg-Brentano setup [2]. M: focussing mirror. CS: convergent slits. Sp: sample. S2: Soller slits. RS: receiving slits. AS: antiscatter slits. D: detector.

A critical parameter in transmission measurements is the absorption caused by sample thickness that has to be optimized to avoid wrong measurements of diffracted intensities. The ideal thickness (t_0) depends on the linear absorption coefficient of the analysed material that varies with the θ angle (figure 2.2.5):

$$t_0 = \cos\theta / \mu$$

In the plot of figure 2.2.5, I_t is the measured diffraction intensity of a certain reflection and I_{max} is the maximum detectable intensity of the same reflection. Form the same plot, it can be seen that too thin and too thick samples suffer up to 30% errors in peak intensity measure.

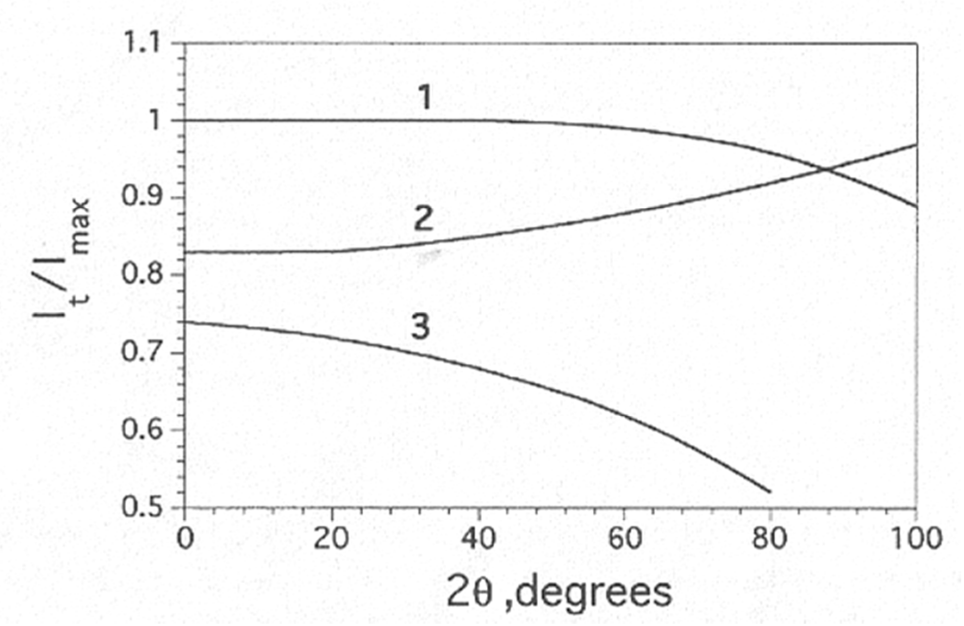

Figure 2.2.5: relative intensities in transmission geometry for samples of different thickness t. t = μ^{-1}(1); t = 0.5 μ^{-1} (2) e t = 2 μ^{-1} (3) [2].

For limited 2θ range (< 60°) and limited absorbing materials, absorption correction can be independent from θ and for the ideal sample thickness the approximation $t_0 \sim \mu^{-1}$ is still valid. Focussing transmission setup measurements bear advantages and disadvantages, in respect to Bragg-Brentano reflection geometry

Advantages:

- Low instrumental errors at low 2θ angles
- Absorption correction independent from θ
- No surface effects (roughness)
- Confined sample (no carbonation)

Disadvantages:

- Lower diffracted intensities
- Sequential measurements
- Limited 2θ accessible range (max 2θ = 90°)
- Limited sample thickness (to avoid absorption problems)

The most implemented experimental geometries have been briefly described for laboratory instruments, where the x-rays production is demanded to conventional sources (x-ray tube or rotating anode). Unconventional sources can be employed in powder diffraction investigations, such as synchrotron radiation sources (SRS), more briefly referred just as "synchrotron". In a synchrotron source, electrons or positrons are accelerated very close to the speed of light along wide circular orbits. When charged particles are maintained in movement along a circular orbit by strong magnetic fields, along the orbit tangent such particles produce electro-magnetic radiations. The radiation energy depends on the particles velocity and for the velocity range close to the speed of light, particles produces x-rays. When using a synchrotron radiation, instrumental defects are reduced a lot because the incident beam exits the storage ring polarized and travels through a parallel path. How is the radiation intensity measured? The most useful unit of measurement is the brightness (photons number$\cdot s^{-1}\cdot(mm\cdot mrad)^{-2}$): for 3rd generation synchrotron the brightness value reaches 10^{20}, when for a conventional x-ray tube is at maximum 10^{7}. The high photons number permits the use of a monochromator on the primary beam to obtain a strictly monochromatic radiation.

In x-ray powder diffraction, transmission setups are generally used coupled with capillary samples (Debye-Scherrer geometry with parallel incident beam). On the diffraction beam path, one or more analysing crystals can be mounted in order to remove possible fluorescence effects (figure 2.2.6). Area detectors are widely mounted because measurement timings are dramatically reduced without loosing resolution (0.1° – 0.05° 2θ) but point detectors are still implemented coupled with an array of analysing crystals.

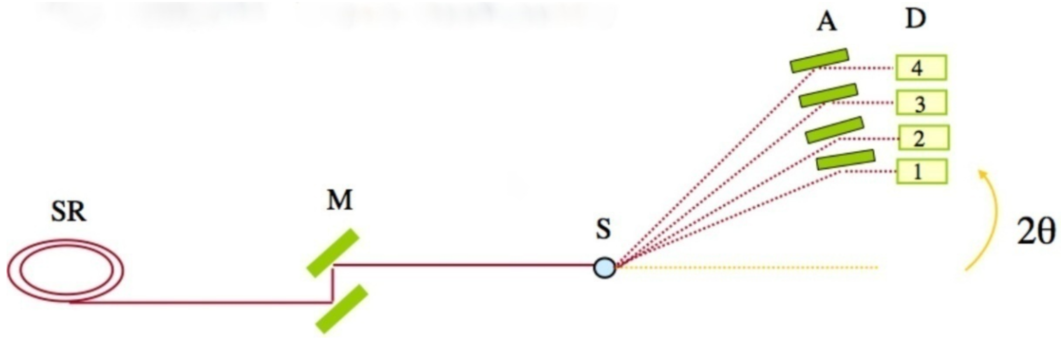

Figure 2.2.6: schematic portray of a synchrotron powder diffraction beamline. The parallel beam exists from the source (SR), it passes through 2 monochromators (M) and heat the sample (S). Diffracted x-rays are deviated to the detector array (D) through a series of analysing crystals (A).

High angular resolution (up to 0.005° 2θ), high counting statistics and non-ambient experimental conditions make the synchrotron sources incomparable facilities where structure solution on powders and *in-situ* time-resolved experiments can be practically developed.

2.2.2. Qualitative analysis of a powder diffraction pattern

The very first step for a correct interpretation of a powder pattern is the phase identification occurring in a sample (qualitative analysis). Each crystalline phase shows a peculiar combination of position and intensity of diffraction peaks. In this way, every diffractogram of crystalline compounds is a sort of “fingerprint” for the compounds, which allow its identification.

The identification process consists firstly in a database search (PDF – Powder Diffraction File) that collects about 300,000 files of inorganic and organic crystalline phases. PDF database is maintained and updated by the International Centre for Diffraction Data (ICDD – http://www.icdd.com). PD Files report information related to the crystalline compound, references and list of d_{hkl} interplanar distances with relative intensities and characteristic Miller indices of each phase.

The correct phase identification procedure applied to a polyphase sample assume different difficult degrees depending on the sample preparation, data collection strategy and the complexity of the phase blend.

2.2.3. Rietveld method

Obtaining detailed structural data (atom positions in the primitive cell, crystallographic site occupancies, thermal motion parameters) from powder diffraction experiments was unconceivable before the groundwork experiments of Hugo Rietveld during the 1960's [3, 4] He is a Dutch physician who demonstrated the possibility to extract accurate structural data from neutron powder diffraction experiments. Later, he extended the same approach to x-ray powder diffraction data, with successful results. The basics of the Rietveld method lays on the complete exploitation of the whole powder profile without extracting the integrated intensities, all the structure and instrumental parameters are refined during the fitting procedure between the calculated and measured data. The refinement procedure implements the least square regression and it requires a reasonable scheme of starting values that approximate the real datum. Such parameters include:

- A function that describe the peak shape
- A function that describe the instrumental effects (on the shape, position and intensity of diffracted peaks)
- Structural parameters as cell dimension, space group and unit cell atomic coordinates

The reliability of the Rietveld method is strictly connected to the quality of powder diffractograms (a well-prepared polycrystalline sample, high counting statistics and limited instrumental problems). During the refinement procedure developed by H. Rietveld, a system of equations is solved using a non-linear leas square regression:

$Y_1^{calc} = k\ Y_1^{obs}$

$Y_n^{calc} = kY_n^{obs}$

Where k: pattern scale factor; n: total number of measured points. The minimized function becomes:

$$\Phi = \sum_{i=1}^{n} w_i \, (\mathrm{Y}_\mathrm{i}^\mathrm{obs} - \mathrm{Y}_\mathrm{i}^\mathrm{calc})^2$$

n is the total number of measured points that depends on the angular range and on the sampling step. The calculated intensity $\mathrm{Y}_\mathrm{i}^\mathrm{calc}$ of the i^th^ point ($1 \leq i \leq n$) in the diffraction pattern is the sum of the background contribution b_i and the whole j^th^ Bragg reflections ($1 \leq j \leq m$) that contribute in that point. Each crystalline phase in the sample adds its own parameters (structure, profile shape) that can be refined. The number of variables is increased when a great amount of phases are involved in the sample: in this case it is not possible to obtain detailed structural parameters due to the strong correlation within the variables. The scale factor K_l of each phase comes to the evidence because this parameter is fundamental in calculating each crystalline fraction in a polycrystalline sample (quantitative analysis):

$$Y_i = \mathrm{b_i} + \sum_{\mathrm{l=1}}^{\mathrm{p}} \mathrm{K_l} \sum_{j=1}^{m} I_j \, \mathrm{y_j(x_j)}$$

Background is an unavoidable contribution in a powder diffraction pattern. It is composed of anelasting scattering, air scattering, fluorescence effects, non-monochromatic beam detector noise. Polynomial, Chebyshev polynomial and Fourier polynomial are the most used analytical functions to describe the background contribution. The peak shape functions describe the intensity distribution around the Bragg position. A peak can assume different shapes (different intensity distributions nearby the central position). To quantify the width of a peak, the parameter Full Width at Half Maximum (FWHM) is calculated. Another fundamental parameter that measure the peak width is the integral breath, which is equivalent to the width of a rectangle having the same height and the same area of the peak. The peak shape function PSF(θ) is the resultant of the convolution of different functions: instrumental broadening, wavelength dispersion, sample contribution. The peak shape can be described following three different approaches:

1. Empirical functions that try to model the peak shape without assigning a physical meaning to the parameters in use
2. A semi-empiric approach based on empiric functions for the instrumental and wavelength functions while to the sample function parameters are given realistic physical meaning
3. Fundamental parameters approach where all the components are associated to a precise physical meaning

Empirical functions employed to describe the peak shape are the Gaussian, the Lorentzian, Pseudo-Voight and Pearson VII. Among these functions, the Pseudo-Voight is often mentioned because data obtained from laboratory instruments are effectively well described by this type of function. It is composed by a gaussian and a lorentzian term in variable proportions, with η as the mixing coefficient that can assume values between 0 (full Lorentzian term) and 1 (full Gaussian term):

$$y(x) = \mathrm{PV(x)} = \eta \frac{\mathrm{C}_{\mathrm{G}}^{1/2}}{\sqrt{\pi} H} + (1 - \eta) \frac{\mathrm{C}_{\mathrm{L}}^{1/2}}{\pi \mathrm{H}} (1 + C_L x^2)^{-1}$$

The lorentzian part is sharper at the maximum but it shows wider tails than the gaussian; both functions are symmetric, G(x) = G(-x). The shape of measured peaks is seldom purely gaussian or lorentzian. Only neutron diffraction data (but not Time-of-flight neutrons) show almost pure gaussian peak shape.

In all the equations the term H determines indirectly the value of the argument x. H depends on the θ angle and its dependence is described by the Caglioti function (an empiric function that describes the peak width at half maximum) where the parameters U, V and W can be refined.

Finally, when authors address to the peak intensity, this is actually the integrated intensity. The observed (and calculated) Bragg reflection intensity depends on multiple variables (experimental setup included) such as the structure factor, the polarization effect, the reflection multiplicity, the magnitude of incident radiation, receiving slits width, the goniometric circle, the radiation wavelength, the absorption effect and preferred orientation effect. The structure effect for a single reflection bears the structural information for that reflection, i.e. type and position of atoms in the primitive cell, thermal motion factor. To extract the structural information it is necessary to describe all the parameters that contribute to the diffracted intensity, in order to isolate the contribution of the structure factor. The structural parameters modified during a Rietveld refinement are: atomic coordinates (x,y,z), crystallographic site occupancy and thermal motion factor. Such parameters are the same factors previously described in the structure factor description.

2.2.4. Quantitative analysis of a powder diffraction pattern

The Rietveld method can be used as a tool to get detailed structural information from powder diffraction data. In this way, monophase samples are easier to treat because each crystalline phase contributes with its own pattern and its own intensities to the resultant pattern, as occurs during a polyphase sample investigation. Furthermore, the peak intensities of each phase are directly proportional to the relative fraction of a certain phase in the sample.

The Rietveld method is one of the possible methods to determine the relative quantity of each phase in a blend.
The other methods are:

- Absorption-diffraction method.
- Internal standard method.

Considering the peak intensity formula in a multiphase system:

$$I_{(hkl)\alpha} = \frac{I_0\lambda^3}{64\pi r}\left(\frac{e^2}{m_e c^2}\right)^2 \frac{M_{(hkl)}}{V_\alpha^2}\left|F_{(hkl)\alpha}\right|^2\left(\frac{1+cos^2(2\theta)cos^2(2\theta_m)}{sin^2\theta\cos\theta}\right)_{hkl}\frac{\nu_a}{\mu_s}$$

The first terms $\frac{I_0\lambda^3}{64\pi r}\left(\frac{e^2}{m_e c^2}\right)^2$ are constants that describe the experimental setup contribution. The second group of terms $\frac{M_{(hkl)}}{V_\alpha^2}\left|F_{(hkl)\alpha}\right|^2\left(\frac{1+cos^2(2\theta)cos^2(2\theta_m)}{sin^2\theta\cos\theta}\right)_{hkl}$ are constants for the *hkl* reflection of the phase α (M_{hkl} is the reflection multiplicity, V is the cell volume and F_{hkl} the structure factor). The last term $\frac{\nu_a}{\mu_s}$ is the ratio between the volume fraction of phase α and the linear absorption coefficient of the whole sample. The same formula can be reduced expressing the phase quantity as weight fraction:

$$I_{(hkl)\alpha} = \frac{K_e K_{(hkl)\alpha} X_\alpha}{\rho_\alpha(\mu/\rho)_s}$$

Where X_α is the weight fraction of phase α, ρ_α is the phase density, $(\mu/\rho)_s$ is the mass absorption coefficient of the sample. In this equation there are two unknown variables: X and the mass absorption coefficient of the sample. The different methods used to quantify a phase try to calculate or to simplify the unknown quantity $(\mu/\rho)_s$.

Absorption-diffraction method.

The equation intensity for each *hkl* reflection has to be differently considered when treating a pure phase or the single phase in a multi phase system. When considering the ratio between these two different intensities, the resulting formula is:

$$\frac{I_{(hkl)\alpha}}{I^{0}_{(hkl)\alpha}} = \frac{(\mu/\rho)_\alpha}{(\mu/\rho)_s} X_\alpha$$

If the multiphase system is constituted only by polymorphs (n number of phases with the same linear absorption coefficient), $(\mu/\rho)_\alpha = (\mu/\rho)_s = (\mu/\rho)_n$ and the formula becomes:

$$\frac{I_{(hkl)\alpha}}{I^{0}_{(hkl)\alpha}} = X_\alpha$$

This linear relation is applied for the quantitative phase analysis of SiO_2 polymorphs (Quartz, Cristobalite, amorphous silica) systems, TiO_2 polymorphs systems (Anatase, Brookite, Rutile) ZrO_2 polymorphs (monoclinic, cubic, tetragonal).

In a binary system with two phases of different $(\mu/\rho)_\alpha$, when $(\mu/\rho)_\alpha$ is different from $(\mu/\rho)_s$, the following relation is used:

$$\frac{I_{(hkl)\alpha}}{I^{0}_{(hkl)}} = \frac{X_\alpha (\mu/\rho)_\alpha}{X_\alpha\left[(\mu/\rho)_\alpha - (\mu/\rho)_\beta\right] + (\mu/\rho)_\beta}$$

Mass absorption coefficient calibration curves are extracted measuring systems for which the composition is well known and determined; alternatively, μ/ρ values published in literature can be still useful. This last formula is applicable only to binary systems. When calibration curves deduced from literature μ/ρ values, microabsorption effects can be ignored and the analysis can be affected by systematic errors. In the absorption-diffraction method, the absolute intensity values are used, both for a pure phase reflections and for the reflections of the same pure phase in a in a multiphase system. The method is greatly affected by the starting experimental conditions.

Internal standard method

The internal standard method avoid the sample absorption coefficient $(\mu/\rho)_s$ dividing two equations as following:

$$I_{(hkl)\alpha} = \frac{K_e K_{(hkl)\alpha} X_\alpha}{\rho_\alpha (\mu/\rho)_s}$$

$$\frac{I_{(hkl)\alpha}}{I_{(hkl)'\beta}} = \mathrm{k}\frac{X_\alpha}{X_\beta}$$

Where α is the unknown phase, β the internal standard, k is the calibration constant calculated from the plot I_α / I_β vs X_α / X_β. When k is defined, adding a precise amount of standard β in a system, the weight fraction of every phase can be calculated, also for amorphous compounds. Multiphase systems have to be accurately prepared to obtain the calibration curves and the standard has to have non-overlapping peaks to be reliable.

If k is generated from the intensity ratio between the most intense reflection of phase α and the most intense reflection of corundum (reference standard) in a system composed of 50% α and 50% corundum, the method is called RIR (Reference Intensity Ratio). For most of the crystalline phases, RIR values are referred into the PDF database.

Generalized RIR method

With this method, different reflections can be chosen, both for the α phase and corundum: the most intense reflection is not essential. Another internal standard, different from corundum, is also allowed.

$$RIR_{\alpha,\beta} = \left(\frac{I_{(hkl)\alpha}}{I_{(hkl)'\beta}}\right)\left(\frac{I^{rel}_{(hkl)'\beta}}{I^{rel}_{(hkl)\alpha}}\right)\left(\frac{X_\beta}{X_\alpha}\right)$$

Normalized RIR method

The weight fractions ratio between two phases, for which RIR is known, can be calculated. Considering a blend of n phases, with known RIR values in respect of corundum, and the sum of each weight fractions equals to 1, it is possible to arrange a system of (n-1) equations that can be solved. If the blend is constituted only by crystalline phases, the system of (n-1) equations can be solved without adding any internal standard.

Limitations on traditional methods

The accuracy on quantitative phase analysis performed with traditional methods depends on the way the intensity values are determined. If the maximum intensity, instead of the integrated area of peak, is considered the potential error is huge. Furthermore, extracting reliable intensity values becomes difficult if reflections are overlapped. Preferred orientation and microabsorption are two of the most effective problems in determining the right peak intensity value. The use of published RIR and I_{rel} values does not guarantee reliable results because often for a certain phase more than one RIR value is published.

Quantitative phase analysis (QPA) with the Rietveld method

Quantitative phase analysis methods discussed in the previous paragraphs are based on the evaluation of integrated intensity of one or a couple of reflections for each phase. If the investigated system shows more than two phases, with an high degree of overlapping peaks, quantitative phase analysis becomes much more difficult. Quantitative phase analysis with the Rietveld method is based on the whole diffraction profile analysis for each phase. The parameter proportional to the weight fraction of a phase in the system is the scale factor of that phase. The expression for the calculated intensity of one phase α can be considered:

$$Y_{i,c} = S_{\alpha} \sum_{(hkl)} K_{(hkl)\alpha} G_{(\Delta\theta i)} P_{(hkl)\alpha} + I_{i,b}$$

G: profile function, P: preferred orientation, S: scale factor.

For each Bragg reflection, the integration and a background correction are performed:

$$S_\alpha = \frac{I_{(hkl)\alpha}}{K_{(hkl)\alpha}}$$

In a multiphase system:

$$Y_{i,c} = I_{i,b} + \sum_{\alpha=1}^{n} S_\alpha \sum_{(hkl)} K_{(hkl)\alpha} G_{(\Delta\theta i)} P_{(hkl)\alpha}$$

Comparing scale factor and intensity:

$$S_\alpha = \frac{I_{(hkl)\alpha}}{k_{(hkl)\alpha}} \qquad I_{(hkl)\alpha} = \frac{K_e K_{(hkl)\alpha} X_\alpha}{\rho_\alpha (\mu/\rho)_s}$$

The final formula for the scale factor of phase α is:

$$S_\alpha = K_e \frac{X_\alpha}{\rho_\alpha (\mu/\rho)_s}$$

The Rietveld scale factor of phase α is related to the absolute value of diffracted intensity of that phase corrected for the absorption effect gave by the sample. Compared to traditional methods, the Rietveld scale factor behaves as the integrated intensity value of one reflection.

The mass attenuation coefficient of the sample still remains unknown. The internal standard method is applied; otherwise the normalization method is used forcing the sum of weight fractions to equal to 1 (if no amorphous phases are present).

Internal standard method normalized with the Rietveld method

The normalization equation (sum of all phases = 1) applied to the scale factor returns the following equation:

$$X_\alpha = \frac{S_\alpha \rho_\alpha}{\sum_n S_n \rho_n}$$

Quantitative phase analysis with Rietveld method is similar to normalized RIR, but while the normalized RIR method calculate the coefficients $K_{(hkl)\alpha}$ from the published RIR values, the Rietveld method uses the structural model for each phase to obtain the same values. True Rietveld quantitative phase analyses are possible only if reliable structural models are available for any crystalline phase present in a sample. One important database for structural models is the ICSD (Inorganic Crystal Structure Database - http://icsd.ill.fr/icsd/index.html).

2.2.5. Cement hydration investigation through diffraction techniques

Several works on cement hydration products have been carried on through *in-situ* synchrotron radiation experiments or conventional sources experiments, principally on synthetized pure phases. There are still some problems in performing quantitative phase analyses with Rietveld method on hydrating cement systems since some hydrated phases, among which there are C-S-H and hydroxyl-AFm, don't have reliable structural models. Lots of research groups used x-ray powder diffraction to determine CH, AFt, AFm and other hydration products content as a function of time. This technique became useful to improve the comprehension of chemical reactions and reactivity of cements [5].

Table 2.2.1 reports the main diffraction techniques employed in hydrated phases of cements research.

Sample	XRD Method	Reference

Synthetic ettringite, monosulphate	R	Fullmann et al. (1999) [6, 7]
Mexican OPC	C	Escalante-Garcia and Sharp [8]
		Emanuelson et al. [9, 10]
Ferrite hydrates	C	Yang et al. [11]
		Kuzel [12]
Ettringite	C	Omotoso et al. [13]
C_3A hydrates	R	Talero [14]
C_3A paste	C	Clark and Barnes [15]
Ettringite	C	
OPC cement (XRD, synchrotron, neutron). Time resolved powder diffraction	Profile fitting	Liang and Narru [16]
Calcium aluminoferrite hydrates	C	Kuzel and Pollmann [17] Parrot et al. [18]
C_3A hydrates	XRD identification	Ftikos and Philippou [19]
OPC hydration	C	
Rich C_2S cements	C	

Table 2.2.1: main diffraction techniques used in hydrated cement phases research. R: Rietveld method [20], C: XRD conventional method [5].

2.3. Scanning Electron Microscopy (SEM)

Scanning electron microscope (SEM, same acronym of microscopy) is a powerful instrument especially suited for high-resolution imaging applied to the investigation of morphological and compositional contrast between different compounds. Images are produced by means of an electron beam that scans the sample surface. Secondary electrons (SE) and backscattered electrons (BSE) are emitted by the sample after the interaction between the sample surface and the incident beam: such emission during beam scanning constitutes the basis of imaging reconstruction. A high-energy electronic beam produced by an electron gun operating at high voltages constitutes the scanning probe. The most used electron source is a Tungsten wire, with diameter ~ 0.01 mm, which produces electrons because of the thermoionic emission. The spatial resolution is dependent on the electronic beam diameter as a first approximation; however, when diameter decreases, an energy loss is expected to occur. To avoid such problem, a LaB_6 crystal can substitute the Tungsten filament, which shows a 10 times higher brightness than Tungsten. Certain instruments mount the so-called Field Emission Gun (FEG), which is made of a sharp and thin Tungsten filament tip: from such tip electrons are accelerated by an intense electric field. Electrons are focussed on the sample through electromagnetic lenses: these lenses are source of instrumental aberrations that reduce the instrumental precision.

SE – Secondary Electrons

The very first surface layer (a few mm) produces Secondary Electrons (SE) and their energy is lower than 50 eV. These electrons are previously born in the atoms and later released when the incident electrons strike into the surface. The number of ejected electrons per incident electron is generally 0.1 – 0.2 at 10 – 30 KeV incident electrons energy. This value doesn't change with the variation of the mean atomic number in the surface volume of interaction. An increase in secondary electrons can occur when the angle between the incident beam and the surface becomes lower or when the incident beam energy is lower than 5 KeV. Secondary electrons are responsible for three-dimensional surface images with the best spatial resolution of 10 nm, wide depth of field and not affected by the chemical contrast between the chemical species occurring in the sample.

BSE – BackScattered Electrons

Backscattered electrons are high-energy electrons (> 50 eV) which penetrate into the sample and re-emerge after a certain number of collisions. The fraction of re-emerging electrons is strictly dependent from the mean atomic number in the interaction area of the sample. Such relation stands at the basis of high-contrast images when chemical species with different mean atomic number are present. To discover compositional contrasts at the micron scale, the sample surface has to be properly flattened and accurately polished in order to avoid shadow effects that modify the quality of the images.

2.4. Isothermal Calorimetry (IC)

The thermal exchange between the sample and the heat sink, the measure of the temperature difference between the sample and the surrounding environment stand at the basis of this technique. The heat generated by the thermal events occurring in the reaction cell can freely flow in the surrounding environment through an Aluminium cage, in a way to keep constant the sample temperature. The thermal sensors, typically thermopiles, can detect the heat flow and can convert it into an electric signal proportional to the thermal power of the reaction. Two twin sites, one for the sample and one for the reference, constitute the calorimeter cell. The reference is necessary because it reduces the noise level in the measure (and increase the signal/noise ratio) and because if a perturbation occurs, this will affect both the sample and the reference at the same way and the effects can be discarded. With this technique, the cement hydration heat flow is measured directly, monitoring the sample when either the sample or the environment is kept in isothermal conditions. One critical condition stands in measuring the released heat flow during the first hydration phases. This particular aspect succeeds in a possible solution in the internal mixing apparatus of calorimeters, which is able to acquire the whole heat flow signal.

In the last twenty years a variety of cements and blends have been studied: Portland cement mixed with high alumina cements, effects of lithium salts in cement mixes, organic additives as retarders [21]. In principle all chemical processes are either exothermic or endothermic and the released/acquired heat can be monitored and measured: the reaction rate is proportional to the production or consumption of heat. Working at isothermal conditions, IC is very sensitive both to small and huge variations in exchanged heat, with the possibility to monitor very slow as very fast reactions. IC is a laboratory technique where the heat reaction rate (mJ/sec = mW) and cumulative heat reaction (mJ) of hydrating cement can be measured in real-time mode at a constant temperature. The produced/consumed heat is proportional to the chemical and physical changes occurring on the sample and the heat flow is proportional to the aggregate rate of changes taking place at a given time. IC is thus a means for dynamic, quantitative evaluation of the rates and energetics of a broad range of rate processes.

REFERENCES

[1] R. E. Dinnebier and S. J. L. Billinge, *Powder Diffraction Theory and Practice*. 2008.

[2] L. S. Zevin and G. Kimmel, *Quantitative X-ray Diffractometry*, Inez Murei. New York: Springer-Verlag, 1995.

[3] H. M. Rietveld, “Line profiles of neutron powder-diffraction peaks for structure refinement,” *Acta Crystallographica*, vol. 22, no. 1, pp. 151–152, Jan. 1967.

[4] H. M. Rietveld, “A profile refinement method for nuclear and magnetic structures,” *Journal of Applied Crystallography*, vol. 2, no. 2, pp. 65–71, Jun. 1969.

[5] P. Barnes and J. Bensted, *Structure and performance of cements*, Second Edi. Spoon Press - Taylor & Francis Group, 2001.

[6] T. Fullmann, J. Neubauer, and G. Walenta, “Quantitative Rietveld phase analysis of hydrated Portland cements. I. Quantitative analysis of synthetic AFm and AFt phases,” in *21st International Conference of Cement Microscopy Association*, 1999, pp. 103–113.

[7] T. Fullmann, G. Walenta, T. Bier, B. Espinosa, and K. Scrivener, “Quantitative Rietveld phase analysis of calcium aluminium cements,” *World Cement Research*, vol. 30, no. 6, pp. 91–96, 1999.

[8] J. I. Escalante-Garcia and J. H. Sharp, “Effect of temperature on the hydration of the main clinker phases in Portland cements. Part I., neat cements,” *Cement and concrete research*, vol. 28, no. 9, pp. 1245–1257, 1998.

[9] A. Emanuelson, E. Henderson, and S. Hansen, “Hydration of ferrite Ca2AlFeO5 in the presence of sulphates and bases,” *Cement and concrete research*, vol. 26, no. 11, pp. 1689–1694, 1996.

[10] A. Emanuelson and S. Hansen, “Distribution of iron among ferrite hydrates,” *Cement and concrete research*, vol. 27, no. 8, pp. 1167–1177, 1997.

[11] R. Yang, C. D. Lawrence, and J. H. Sharp, “Delayed ettringite formation in 4-year old cement pastes,” *Cement and concrete research*, vol. 26, no. 11, pp. 1649–1659, 1996.

[12] J. H. Kuzel, “Rietveld quantitative XRD analysis of Portland cement: Part I. Theory and application to the hydration of C3A in the presence of gypsum,” in *18th International Conference of Cement Microscopy Association*, 1996, pp. 87–99.

[13] O. Omotoso, D. Ivey, and R. Mikula, “Hexavalent chromium in tricalcium silicate: Part I Quantitative X-ray diffraction analysis of crystalline hydration products,” *Journal of materials science*, vol. 3, pp. 507–513, 1998.

[14] R. Talero, “Comparative XRD analysis of ettringite originating from pozzolan and from Portland cement,” *Cement and concrete research*, vol. 26, no. 8, pp. 1277–1283, 1996.

[15] S. Clark and P. Barnes, “comparison of laboratory, synchrotron and neutron diffraction for the real time study,” *Cement and Concrete Research*, vol. 25, no. 3, pp. 639–646, 1995.

[16] T. Liang and Y. Nanru, “Hydration products of calcium aluminoferrite in the presence of gypsum,” *Cement and concrete research*, vol. 24, pp. 150–158, 1994.

[17] J. H. Kuzel and H. Pöllmann, “Hydration of C3A in the presence of Ca(OH)2, CaSO4·2H2O and CaCO3,” *Cement and concrete research*, vol. 21, pp. 885–895, 1991.

[18] L. J. Parrott, M. Geiker, W. A. Gutteridge, and D. Killoh, “Monitoring Portland cement hydration: comparison of methods,” *Cement and concrete research*, vol. 20, no. 6, pp. 919–926, 1990.

[19] C. Ftikos and T. Philippou, “Preparation and hydration study of rich C2S cements,” *Cement and concrete research*, vol. 20, no. 6, pp. 934–940, 1990.

[20] W. A. Gutteridge, “Quantitative X-ray powder diffraction in the study of some cementive materials,” *Proceedings of the British Ceramic Society*, vol. 35, pp. 11–23, 1984.

[21] C. Evju, “Initial Hydration of Cementitious Systems Using a Simple Isothermal Calorimeter and Dynamic Correction,” *Journal of thermal analysis and calorimetry*, vol. 71, pp. 829–840, 2003.

3. Materials and Methods

Mix NIST were produced after grinding and blending raw materials, synthetized from chemical laboratory grade CaO, SiO_2, Al_2O_3 and Gypsum ($CaSO_4 \cdot 2H_2O$). Alite was synthetized by W.R. Grace while Cubic Tricalcium Aluminate by NIST.

NIST also chose a reagent-grade 99% Gypsum to obtain the final mixes.

3.1 Characterization of raw materials and blends

The first characterization on raw materials has been carried out by NIST. Particle size distribution (PSD) on C_3A returned a d_{50} of 13.2 µm and d_{90} of 49 µm; on Gypsum a d_{50} equals to 11.2 µm and d_{90} of 28.5 µm; C_3S showed a d_{50} of 14 µm and a d_{90} of 39 µm. The goal to produce synthetic cement mixes was to study the proper content of Gypsum: it is reached when the calorimetric peak attributed to C_3S dissolution occurs just before the calorimetric peak due to the complete Gypsum consumption. In order to do so, the work of Tenoutasse [1] has been considered and finally three blends was produced and named Mix 1, 2 and 3. Table 3.1 summarizes the mixtures, in which phases are expressed as mass ratios and as weight percentages.

Mass ratios	C_3S	C_3A	Gypsum	Weight %	C_3S	C_3A	Gypsum
MIX 1	80	20	2.3		78.20	19.55	2.25
MIX 2	80	20	4.3		76.70	19.18	4.12
MIX 3	80	20	6.3		75.26	18.81	5.93

Table 3.2: mass ratios (left side) and weight percentages (right side) of synthetic NIST mixes.

We performed X-ray powder diffraction (XRPD) characterization on Mix 1, 2 and 3 using a PANalytical X'Pert Pro MPD diffractometer. This instrument is very reliable and permits the operator to switch from reflection Bragg-Brentano geometry to focussing transmission capillary geometry in a very easy way, thanks to PreFIX© technology. The diffractometer implements a ceramic x-ray tube with a linear focus and Cu anode, 40 kV and 40 mA, goniometric radius of 240 mm (PW 3050/60), θ/θ mode. When used in reflection geometry, incident beam optics includes divergence slits of ½, Soller slits of 0.04 rad and antiscatter slit of ¼. Diffracted beam optics are composed of antiscatter slits of ¼ and Soller slits of 0.04 rad, Ni-Kβ filter and PIXcel Position Sensitive Detector, with a 3.347° 2θ maximum aperture. We measured the dry powders in Bragg-Brentano reflection geometry between 6° and 76° 2θ, $CuK\alpha_{1,2}$, step size of 0.026° 2θ, counting 80s per step. Every measure lasts 15 minutes and we performed two repetitions in order to improve the counting statistics.

We performed a qualitative phase analysis in order to determine the real powders content: We determined the presence of monoclinic and triclinic C_3S, C_2S, C_3A and Hydrogarnet. Rietveld quantitative phase analysis underlined some peculiarities:

- A small amount of Hydrogarnet (3-4%).
- The structural model of C_3S proposed by Nishi *et al.* [2] does not fit well the experimental diffraction pattern. On the other hand, using the M1 structural model proposed by De Noirfontaine *et al.* [3] and the Triclinic model of Golovastikov *et. al.* [4] the profile fitting become markedly better.
- C_3S and C_3A peaks overlap all the strongest C_2S peaks, making very difficult its determination.

In the following diagrams we show the difficulty on choosing the right C_3S structural model on some 2θ ranges. Figures are all referred to Mix 3, but we found the same problems in Mix 1 and 2 profiles fitting. Refinement strategy considered an initial step to calculate the instrument contribution to line profile fitting measuring the SRM-640c Si NIST standard. This preliminary procedure involved the calculation of the instrumental zero shift, sample displacement, divergence slit and Soller slits values. Fundamental parameters approach [5] has been implemented in Topas v. 4.1 [6] and used in the Rietveld calculations.

Refinement strategy included a continuous background refinement using Chebyshev polynomial function and scale factor, while cell parameters and Lorentzian crystallite size were refined in this order. Neither atomic coordinates nor atomic displacement parameters were considered in the refinement.

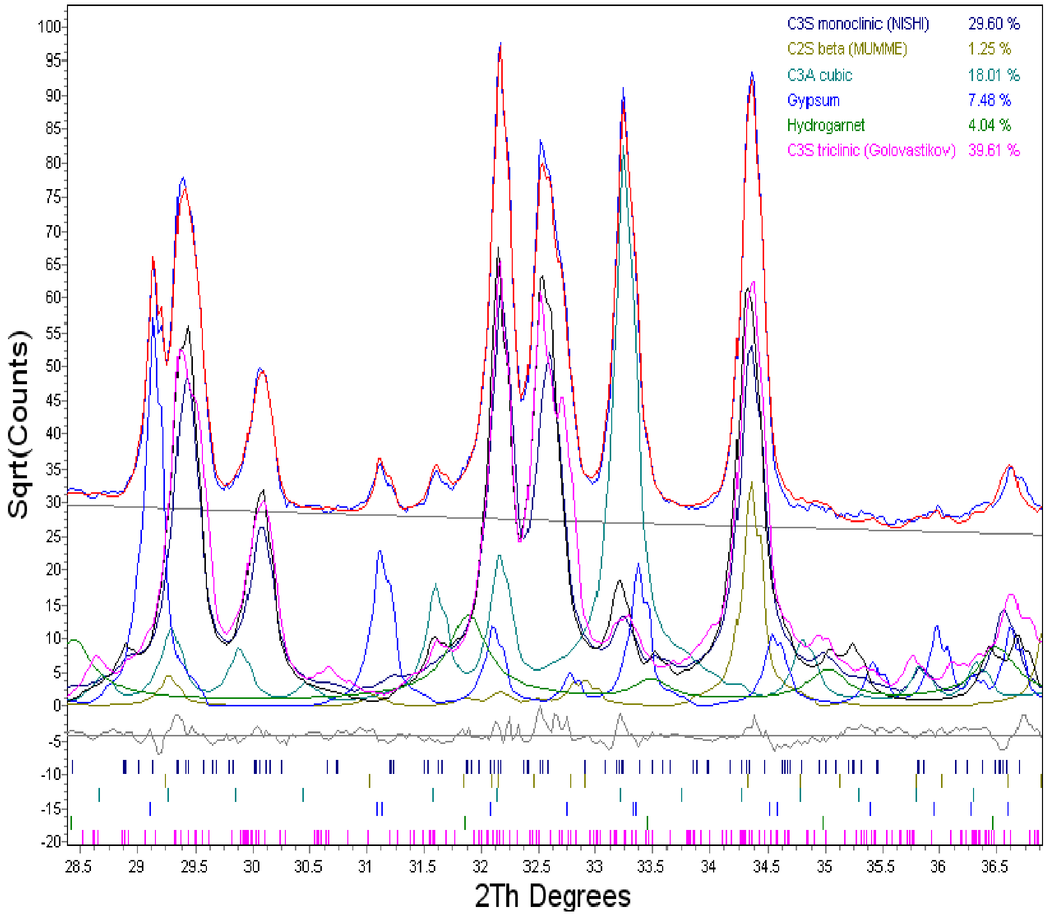

Figure 3.1: profile fitting using the M3 and Triclinic C_3S structural models (28°-36° 2θ range, CuKα)

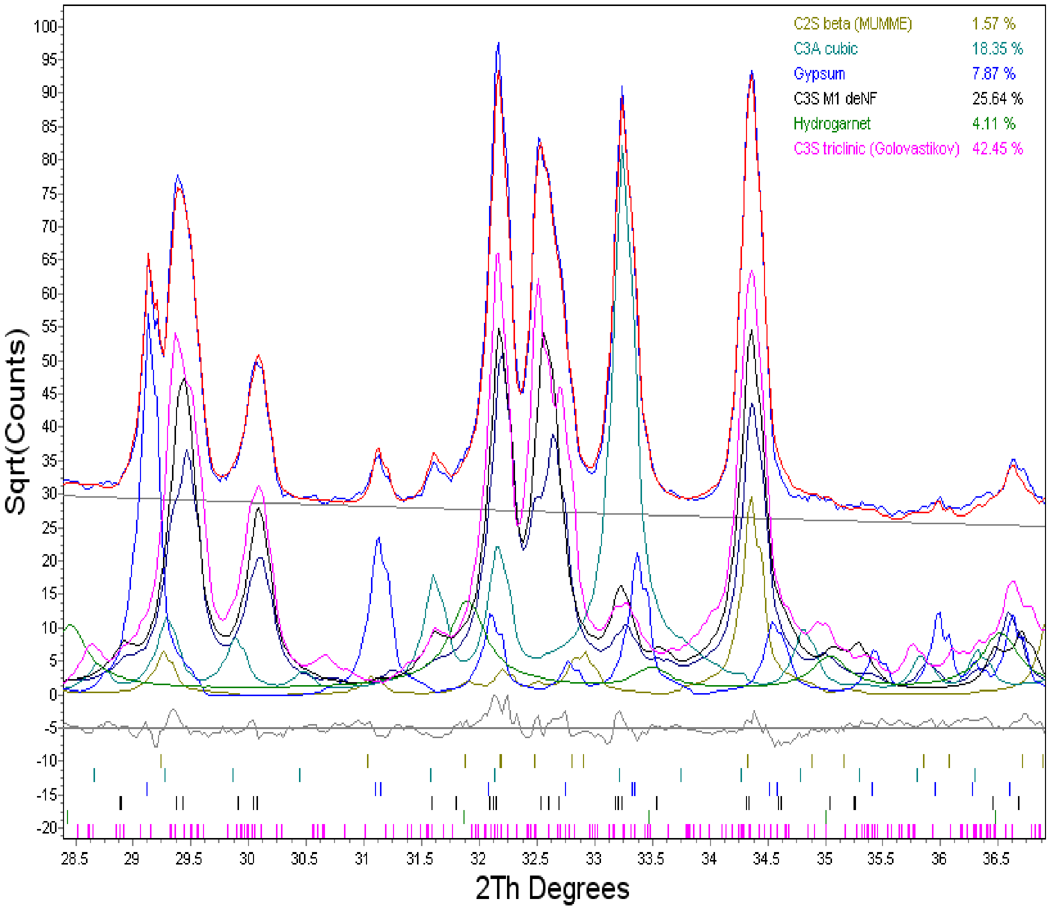

Figure 3.2: profile fitting using the M1 and Triclinic C_3S structural models (28°-36° 2θ range, CuKα)

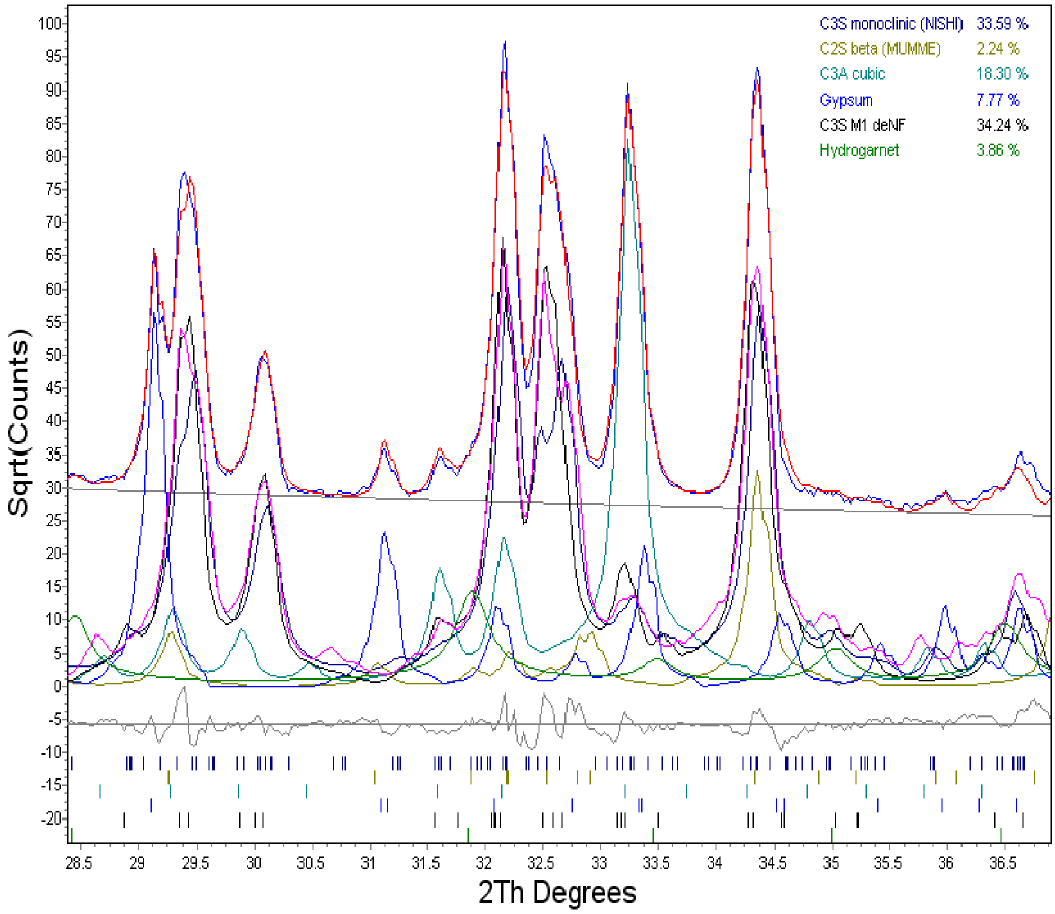

Figure 3.3: profile fitting using the M3 and M1 C_3S structural models (28°-36° 2θ range, CuKα)

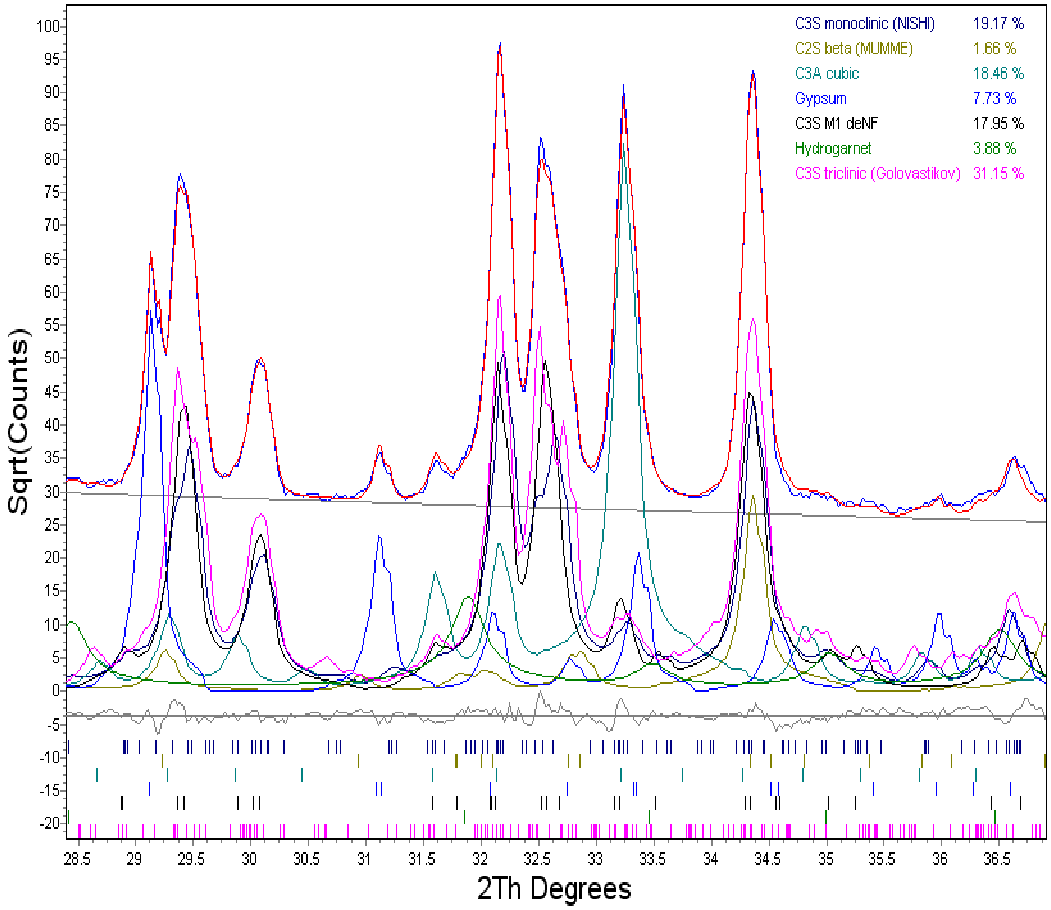

Figure 3.4: profile fitting using the M3, M1 and Triclinic C_3S structural models (28°-36° 2θ range, CuKα)

As we can see from figures 1, 2, 3 and 4, some differences are remarkable. In particular, where the triclinic structural model is not considered the profile fitting worsen (figure 3.3). On the other hand, when triclinic + M3 and/or M1 are considered together the profile fitting becomes markedly better (figures 3.1, 3.2 and 3.4). In particular, the 28.5° and the 32.5° 2θ peaks show a different fit when the Triclinic + M3 and/or M1 structural models are applied. It is difficult to say which combination is the true one.

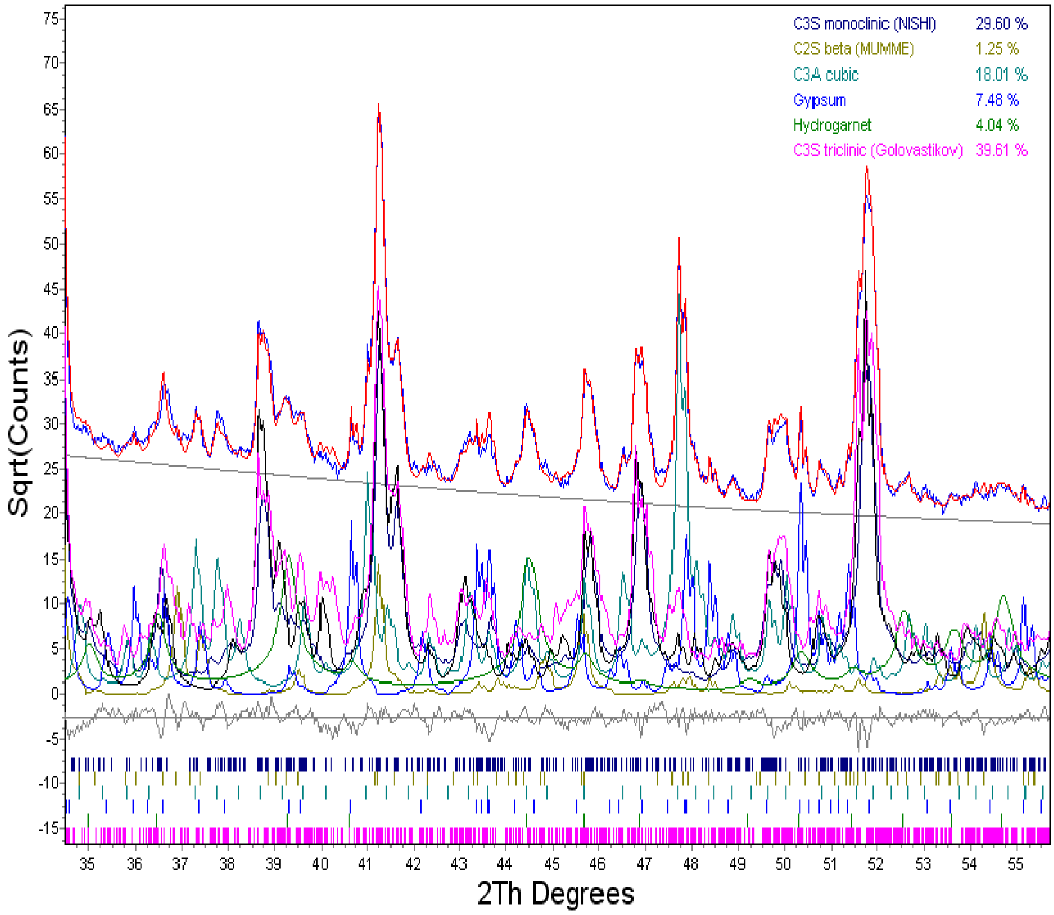

Figure 3.5: profile fitting using the M3 and Triclinic C_3S structural models (35°-55° 2θ range, CuKα)

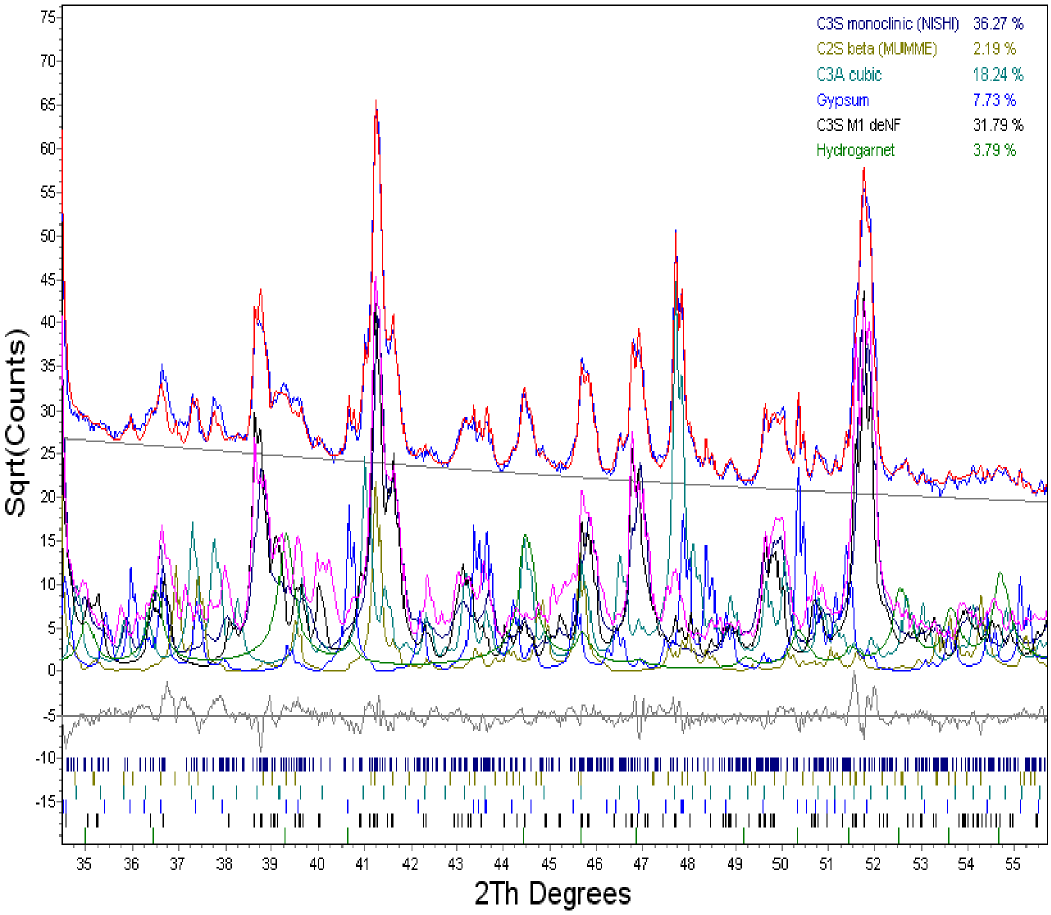

Figure 3.6: profile fitting using the M3 and M1 C_3S structural models (35°-55° 2θ range, CuKα)

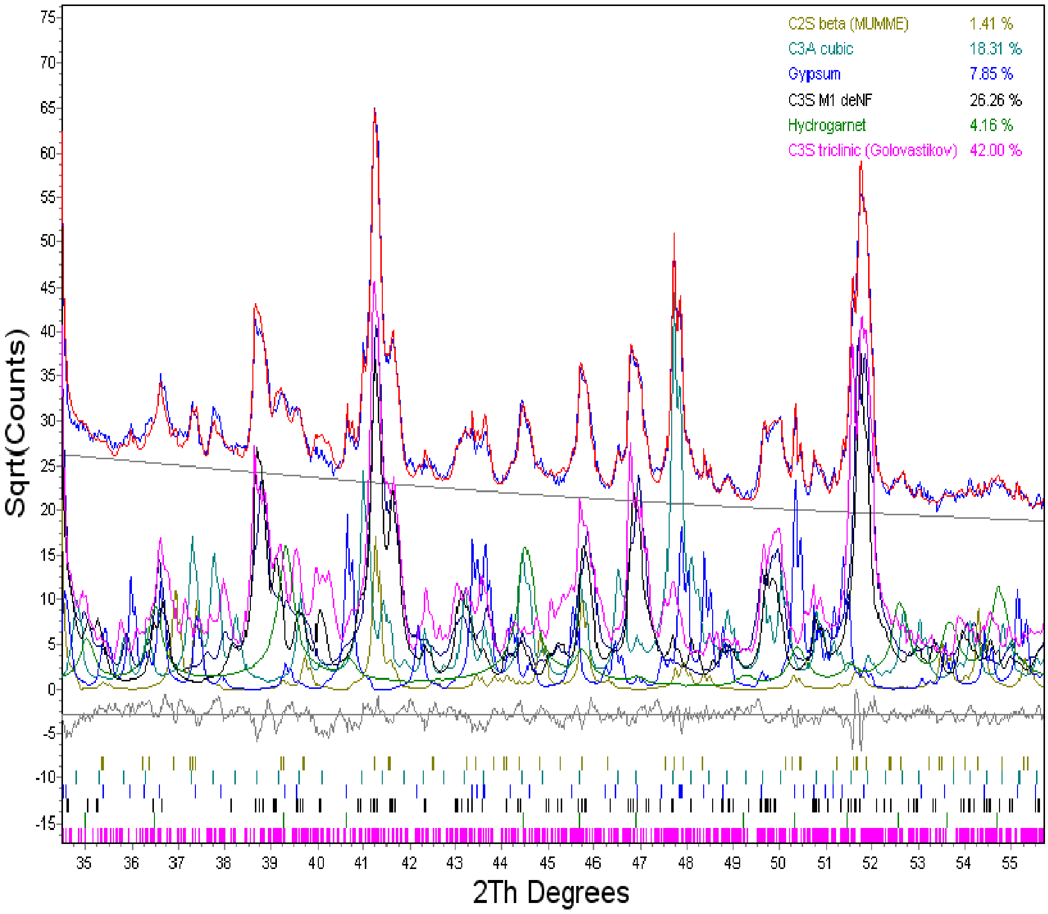

Figure 3.7: profile fitting using the M1 and Triclinic C_3S structural models (35°-55° 2θ range, CuKα)

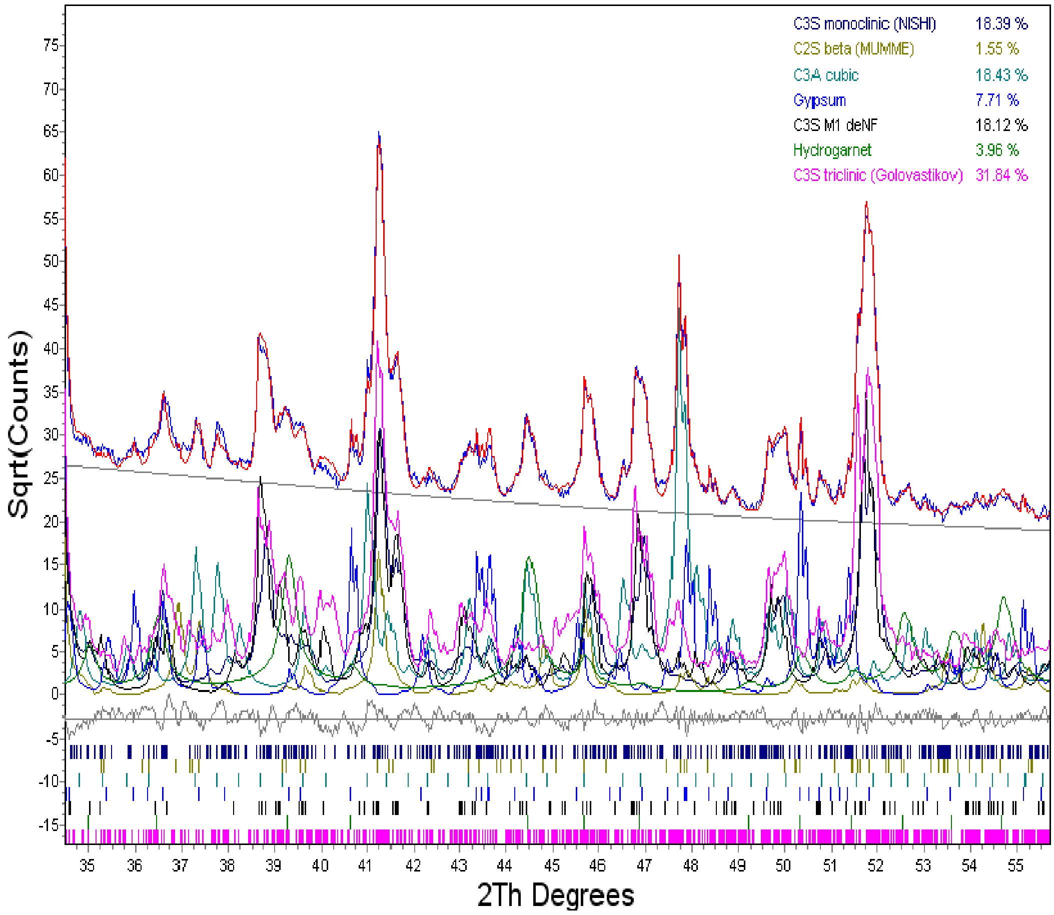

Figure 3.8: profile fitting using the M3, M1 and Triclinic C_3S structural models (35°-55° 2θ range, CuKα)

Figures 3.5, 3.6, 3.7 and 3.8 point out the same situation described before. In these figures we considered the 35° - 55° 2θ range, where the 36.6°, 45.7°, 46.8° and 49.9° peaks are better described when we choose to apply the triclinic structural model in addition to M3 and/or M1 structural models.

In any case, some peaks are still not completely well described by such models.

Taking into account all the information described above, we performed a Rietveld quantitative phase analysis on dry powders, considering the three structural models for C_3S. Results are shown in the table below.

	C_3S-M3	C_3S-M1	C_3S-Tri	C_3S-Tot	C_2S	C_3A	Gypsum	Katoite
MIX 1	23.32	17.12	31.76	72.20	1.84	19.21	3.20	3.54
MIX 2	21.57	18.81	29.33	69.71	1.65	18.45	5.86	4.32
MIX 3	19.17	17.95	31.15	68.27	1.86	18.46	7.73	3.88

Table 3.3: Rietveld quantitative phase analysis performed on Mix 1, 2 and 3.

As we can see from table 3.2, we have a very low amount of C_2S (under the instrument detection limit) and this led us to exclude it from the kinetic calculations. A reason for this choice lays on the parametric quantitative phase analysis, where minor phases (< 3%) and slow reacting phases (as C_2S) are difficult to monitor. On the other hand, Gypsum is overestimated even applying the March-Dollase [7] preferred orientation correction.

One possible choice can be then M1 + Triclinc structural models for C_3S, even if this is not the definitively choice.

3.2 Preparation of pastes for XRD in-situ measurements

There is more than one choice in preparing a cementitious paste for a XRD study. One is well developed in synchrotron radiation facilities where the sample is being hydrated directly during the measure (*in-situ* hydration and measure). A capillary works as sample holder and water is injected by air compression directly into the capillary. A disadvantage of this technique is that the sample is not completely hydrated, becoming non homogeneous.

Another possibility is to hydrate and cure the sample *ex-situ* until the setting time and later cutting the sample in slices at increasing time, stopping the hydration process with chemical solvents or salts and studying the remaining part. Unfortunately, solvents can alter the metastable crystal structure of AFm phases or even making them disappear. A third technique is to hydrate the sample *ex-situ*, seal the paste and follow the hydration through *in-situ* measurements: it is not possible to analyse the paste in the first 15 minutes because and it is no more possible to modify the water to cement ratio after sealing. Actually we decided to use the last described approach, because it assures longer measurements timings, even if the first minutes of hydration cannot be assessed.

To analyse the pastes three different instrumental setups can be used:

1. Reflection Bragg-Brentano with a Kapton ® foil that protect the surface
2. Focussing transmission flat stage, with 2 Kapton ® foils that contain the sample.
3. Focussing transmission capillary.

Kapton ® is a synthetic organic compound produced from the condensation of pyromellitic dianhydride and 4,4'-Oxydianiline [8]. It is manufactured as yellow thin foils and the main feature for our purposes is that it is transparent to x-rays, apart from a unique reflection at 5.5° 2θ, λCu.

In focussing transmission geometry incident beam optics includes a focussing x-ray mirror: it is a multi-layered crystal of W/Si, manufactured to give no diffraction lines and to produce a convergent beam. Another important feature of this mirror is to select the incident wavelength, reducing the Kβ under instrumental resolution, avoiding the use of a Ni filter. Divergence slits and antiscatter slits of ½ and Soller slits of 0.04 rad are equipped using this setup.

Focussing flat-stage requires a very low amount of material (0.02 g) squeezed between two Kapton ® foils, which unfortunately are not able to seal a hydrating ambient and water loss becomes certain. This is the main reason why we avoided the use of flat stage transmission geometry.

Bragg-Brentano samples show a chemical shrinkage due to the evolution of hydration: during XRD measurements we can see a significant left-shift of the whole profile because the sample lays no more on the focussing circle. Moreover, Kapton ® is suspected to be cause of water loss at long hydration time. For these reasons we avoided the use of reflection Bragg-Brentano geometry and we concentrated our attention to focussing capillary geometry.

A common mixing protocol to standardize samples has been developed by W.R. Grace. It consists in using the same power-control mixing unit, holders and scrapes, hydrating pastes with water to cement ratio (w/c) equals to 0.5. Hereafter the necessary equipment and the protocol itself are described.

I. EQUIPMENT

1. Eurostar-power basic (IKA) with hand mixer beater
    2. Lab scissor jack
    3. Lab scrape blade
    4. Lab timer (to plug mixer into)
    5. 20 cl plastic cups

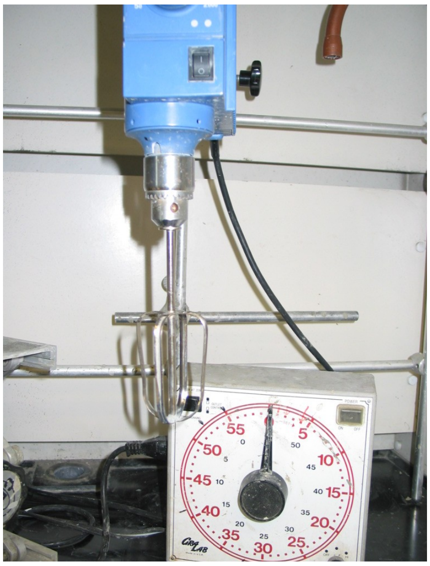

Figure 3.9: Eurostar mixer (power digi-visc, IKA Labotechnic) setup with hand mixer beater and timer connected to the mixer.

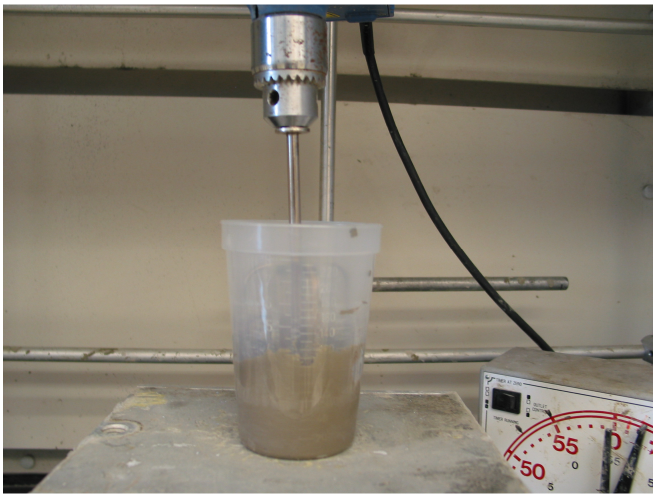

Figure 3.10: Plastic cup with cement paste prepared with Eurostar mixer.

II. PROTOCOL

1) Have equipment ready:

Mixer plugged into lab timer-mixer set to run at 400rpm

Mixer, holding bar and lab jack at proper positions (important to insert cup into notch before and during mixing)

Have mix materials weighed and ready

Have both water and chemical(s) in the same 20 cl cup (make sure they are mixed, using hand vortex technique)

2) Hold plastic mixing cup with cement, in position to mix

- Start mixer (set at 4minutes)
- Pour water into mixing cup at mixing start – there is enough time to rotate mixing cup to get good mixing
- At 30 seconds into mixing stop the mixer (clock is continuing to run) and use scrape blade to scrape bottom and sides of the mixing cup. Scrape for roughly 15 seconds.
- Insert cup back into notch, and begin mixing after scraping.
- At 120 seconds into mixing, stop the mixing and scrape again (clock is still running).

- Insert cup back into notch and let the suspension rest until 180 seconds. Start mixing again at 180 seconds.
- At 240 seconds, the mixer will shut off. Remove cup.

3) To clean mixer blade, place 1 liter cup of water (Labeled “Rinse H_2O”) under mixing support with lab jack and turn timer to 5 minutes. This can be done right after removal of the cup with cement paste suspension.

4) The cleaning water contaminated with cement paste should be poured into the special waste container. The paper towels from wiping the blade should be thrown to the trash container.

We collected data on pastes in 0.3mm boron-glass capillaries to avoid absorption problems, just pushing the hydrating paste in the capillary funnel till the capillary itself seemed to be properly loaded. Capillaries were sealed with vax in order to prevent carbonation. Measures were carried out between 2° and 66° 2θ angle, using a 0.02° step size, counting 120s per step, 20 min/run. This measuring strategy gives us a good compromise within counting statistics, precision on reflections positions and useful time coverage for systems which evolve rapidly during the first hours of hydration.

We stressed our attention on controlling temperature stability in the diffractometer case. Since kinetics are directly influenced by a rising/dropping temperatures, it is fundamental to control the temperature parameter in the case. Reaction temperature can be estimated to be of 23.0°C ± 0.5°C. Table 3.3 resumes experimental setup information on measured pastes.

Mix	Quantity (g)	Mixing method	2th range (°)	Step (°)	Time/step (s)	Meas. Time (min)	Total meas. time
1	5g + 2.5g H_2O	4 min, GRACE protocol	3 - 66	0.026	120	20	26h 53min
2	5g + 2.5g H_2O	4 min, GRACE protocol	3 - 66	0.026	120	20	82h 48min
3	5g + 2.5g H_2O	4 min, GRACE protocol	3 - 66	0.026	120	20	105h 59min

Table 3.4: experimental XRD program

Qualitative phase analysis presents C_3S, C_3A, Gypsum, Portlandite and Ettringite in all pastes.

We also detected Hemicarboaluminate, which can crystallize only when CO_2 is present. Considering that capillaries are sealed with wax during hydration, we excluded the air contamination and so we measured the dissolved CO_2 content in water by chemical titration, which gave a content of 1.50 ± 0.15 mg/l. This acts as a source for Hemicarboaluminate precipitation (thermodynamically more stable) when Ettringite starts to dissolve. Nevertheless, since Hemicarboaluminate has no crystal structure, it has not been considered in Rietveld-QPA. Dissolution/precipitation kinetics are obtained after mass balance recalculation based on the consumption of anhydrous calcium silicate hydrates which produces C-S-H and Portlandite [9].

3.3 Isothermal Conduction Calorimetry (IC) on pastes

First calorimetric measurements was carried out by W.R. Grace to establish the right Gypsum quantity to be added to C_3S-C_3A mix. The final mix result has been shown in table 3.1. Temperature greatly influences the cement hydration kinetics and studying how kinetics change varying the temperature is an important issue to solve. In order to understand the calorimetric effect produced by dissolution/precipitation reactions, we performed 4 different tests for each mix at 4 different curing temperatures: 20°C, 23°C, 26°C, 32°C. 2g of material for each experiment has been hydrated *ex-situ* with 1g of Millipore water in a plastic vial, stirred in an orbital stirrer for 30s (in order to ensure an homogeneous hydration of the powder) and immediately put into the sample cell of the calorimeter. A proper amount of water, with the same heat capacity of the sample, has then put into the reference cell to avoid perturbations and to have a better signal/noise ratio.

In this way we calculated also the apparent activation energy (E_a) for each reaction and for pastes, with a possible interpretation of the reaction rate and the rate limiting factors because the apparent activation energy is the parameter relating the sensitivity of the hydration kinetics of cement to a variation in temperature [10].

REFERENCES

[1] N. Tenoutasse, “The Hydration Mechanism of C3A and C3S in the Presence of Calcium Chloride and Calcium Sulphate,” 1969, pp. 372–378.

[2] F. Nishi, Y. Takéuchi, and I. Maki, “Tricalcium silicate Ca3O[SiO4]: The monoclinic superstructure,” *Zeitschrift für Kristallographie*, vol. 172, pp. 297–314, 1975.

[3] M. De Noirfontaine, “Tricalcium silicate Ca3SiO5 superstructure analysis: a route towards the structure of the M1 polymorph,” *Zeitschrift für Kristallographie*, vol. 2, pp. 102–112, 2012.

[4] N. I. Golovastikov, R. G. Matveeva, and N. V. Belov, “Crystal structure of the tricalcium silicate (CaOSiO2)3=C3S,” *Kristallografiya*, vol. 20, pp. 721–729, 1975.

[5] R. Cheary, A. Coelho, and J. Cline, “Fundamental parameters line profile fitting in laboratory diffractometers,” *Journal of Research of the National Institute of Standards and Technology*, vol. 109, no. 1, pp. 1–25, 2004.

[6] “TOPAS version 4.1.” Bruker AXS, Karlsruhe, Germany, 2007.

[7] W. A. Dollase, “Correction of intensities for preferred orientation in powder diffractometry: application of the March model,” *Journal of Applied Crystallography*, vol. 19, pp. 267–272, 1986.

[8] W. The free enciclopedia, “Kapton,” *26 July 2012, 15.49*. [Online]. Available: http://en.wikipedia.org/wiki/Kapton.

[9] L. Valentini, M. C. Dalconi, M. Parisatto, G. Cruciani, and G. Artioli, “Towards three-dimensional quantitative reconstruction of cement microstructure by X-ray diffraction microtomography,” *Journal of Applied Crystallography*, vol. 44, no. 2, pp. 272–280, 2011.

[10] E. Wirquin, M. Broda, and B. Duthoit, “Determination of the apparent activation energy of one concrete by calorimetric and mechanical means: Influence of a superplasticizer,” *Cement and concrete research*, vol. 32, pp. 1207–1213, 2002.

4. Results e Discussion

4.1. X-ray Powder Diffraction on pastes

In the following sections, the quantitative phase analysis of *in-situ* XRPD on hydrating pastes will be presented and discussed. Qualitative phase analysis showed the presence of C_3S, C_3A, Gypsum, Portlandite, Ettringite and Hemicarboaluminate in all the hydrating pastes. It is possible to follow the dissolution kinetics of the starting phases and the precipitation kinetics of their products. The hydration kinetics have been followed until all the gypsum is depleted and C_3A shows the increase in the dissolution rate.

It is well known that the hydration of cement materials produces amorphous phases, such as C-S-H and C-A-H [1]. Rietveld quantitative phase analysis is based on the assumption that the investigated system is composed only by crystalline phases: in such context, only crystalline phases can be directly quantified. Nevertheless, it is possible to calculate the amorphous content of a system by means of reliable methods, such as internal standard method, external standard [2] method and PONCKS method [3]. In literature there are controversial results about the which internal standard is suitable for cements [4–7]: Al_2O_3 has a linear absorption coefficient too different from the main cement phases while TiO_2 is claimed to be not perfectly unreactive. Another way to quantify the amorphous content is to perform a mass balance. Specifically performed to obtain the C-S-H content, when the initial phase content and the water amount are known, it is possible to recalculate the exact amount of each phase. As described in Valentini *et. al.* [8], C-S-H weight fraction can be calculated starting from Portlandite content following equation (4.1):

$$3C_3S + 16H \rightarrow 3C_{1.7}SH_4 + 4CH \tag{4.1}$$

Assuming that all the amorphous material produced during hydration by unique consumption of C_3S is C-S-H, Ca/Si and water content remaining constant, the C-

S-H content is obtained by mass balance calculation. Young and Hansen [9] proposed a Ca/Si ratio of 1.7 and 4 water molecules for curing conditions closed to water saturation.

All the phase kinetics described below are recalculated from the original Rietveld quantitative phase analysis through the software RieCALc, using the mass balance approach developed by Valentini [8].

4.1.1 Mix 1

Mix 1 is characterized by the lowest amount of gypsum and can be referred also as undersulphated system. In this model cement, C_3A shows a continuous dissolution from the very beginning (0.1%/h), with a sharp increase of the dissolution rate after 4 hours (0.5%/h) that lasts totally 6 hours. Between 10 hours and 20 hours from the beginning of hydration, C_3A dissolution enters the deceleration period (0.08%/h). The kinetics have been monitored until 26 hours after the beginning of hydration (figure 4.1).

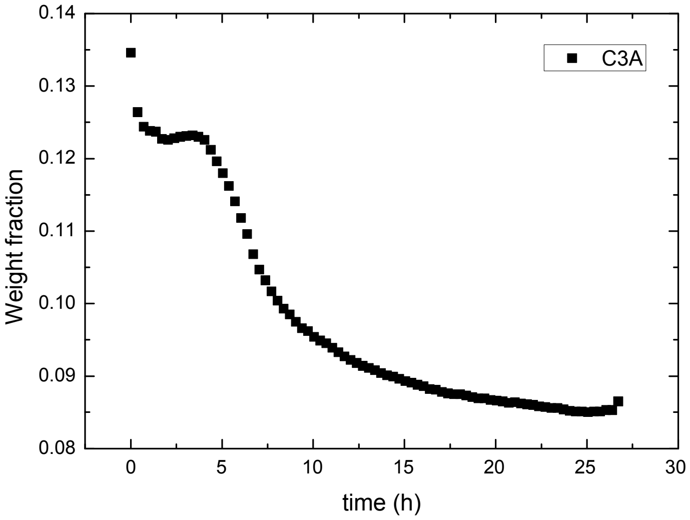

Figure 4.11: dissolution kinetic of C_3A in mix 1.

Gypsum dissolution is also very rapid: after 6 hours it is completely depleted from the system, with a dissolution rate of 1.3% per hour. It can be underlined that there is only a little time gap (2 hours) between the increase in the dissolution rate of C_3A and the complete dissolution of gypsum, possibly related to the uncertainty in measuring the exact moment of complete gypsum depletion (figure 4.2).

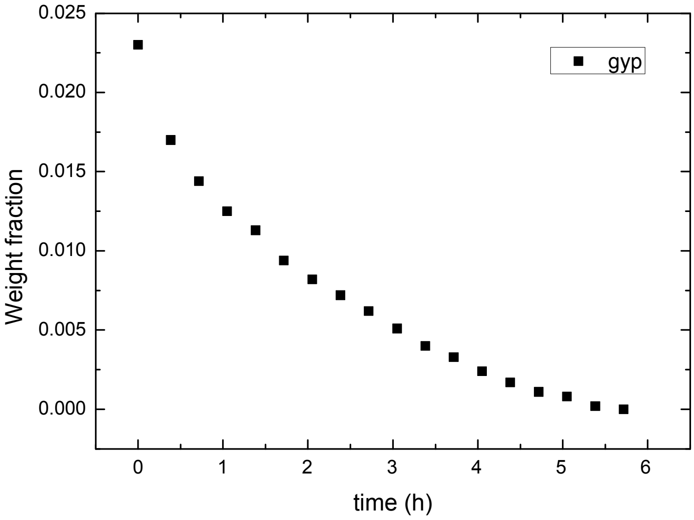

Figure 4.12: dissolution kinetic of Gypsum in mix 1.

From the dissolution of C_3A and gypsum, the precipitation of ettringite occurs. It continues to grow until gypsum is present into the system: indeed, the maximum ettringite content is reached after 7 hours (1 hour later the complete gypsum dissolution). The precipitation rate is fast within the first 3 hours (0.5%/h) but it decreases to 0.13%/h between 3 and 7 hours after hydration (figure 4.3). Subsequently, ettringite dissolves at a rate of 0.02%/h, presumably converting into AFm-14 (not detected).

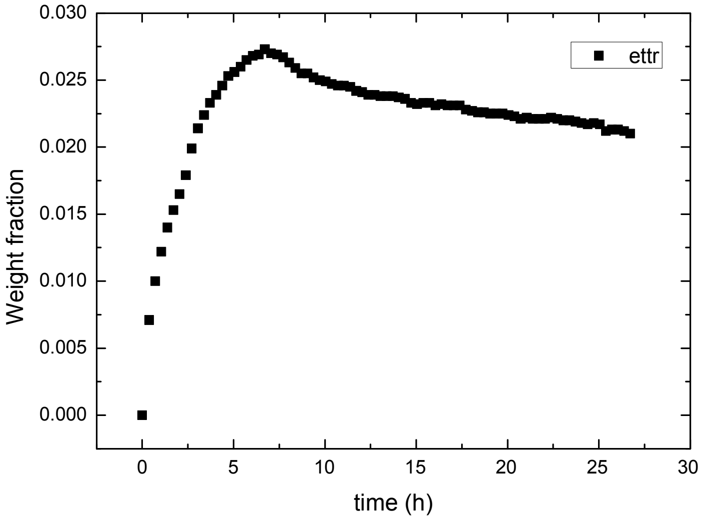

Figure 4.13: precipitation kinetic of Ettringite in mix 1.

C_3S dissolution kinetic is characterized by an initial apparent precipitation which will be discussed in one of the next sections. Actually, a precipitation of C_3S can be excluded and the dissolution has been taken into account as the only possible chemical process that affects the C_3S. In this scenario, the C_3S kinetic is characterized by a dissolution rate of 0.4%/h between 3 and 8 hours, 1%/h between 8 and 20 hours and 0.3%/h between 20 and the of the measure (figure 4.4).

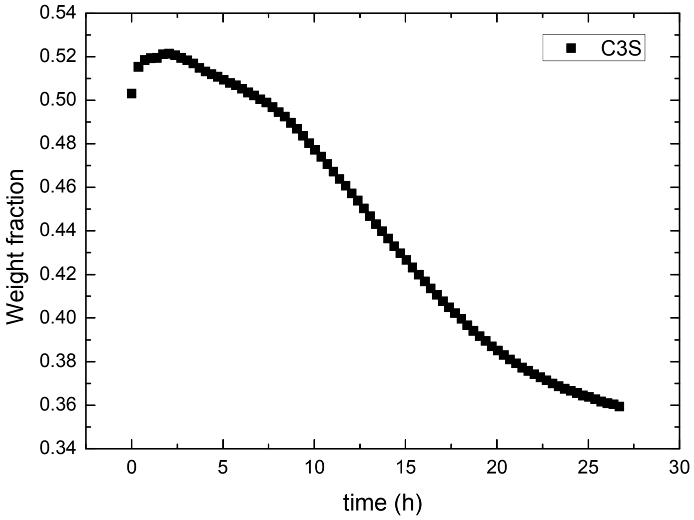

Figure 4.14: dissolution kinetic of C_3S in mix 1.

From equation 4.1, when C_3S dissolution occurs the subsequent precipitation of portlandite can be detected. Ca-Si hydrates is calculated from a mass balance when the initial components are known [8]. Portlandite shows a period between the zero time and 3-5 hours when it is practically undetectable; subsequently, the precipitation rate is almost constant (0.4%/h) until 20 hours, when the rate becomes lower (0.17%/h).

C-S-H precipitation behaviour is practically the same of portlandite, with a precipitation rate between 4 and 20 hours of 1.1%/h and a lower velocity in the last 6 hours (0.5%/h).

Portlandite and C-S-H kinetics are shown in figure 4.5.

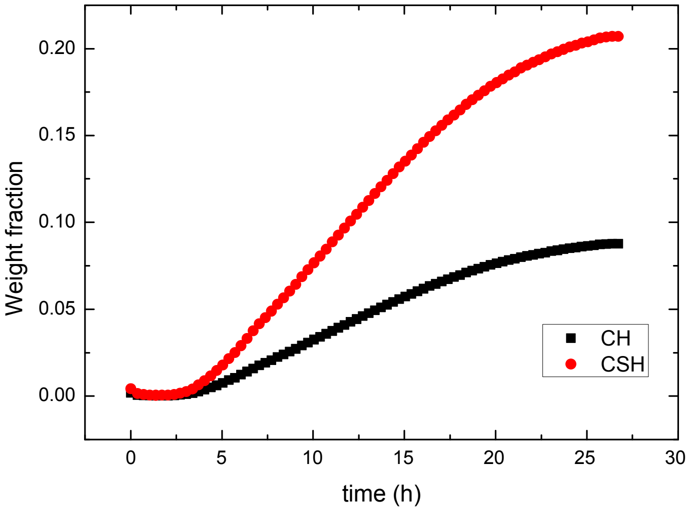

Figure 4.15: Portlandite (black squares) and C-S-H (red dots) precipitation kinetics in mix 1.

4.1.2 Mix 2

Mix 2 is characterized by the intermediate amount of gypsum and indeed considered as the proper sulphated system.

In figure 4.6, C_3A shows an initial dissolution when mixed with water at a rate of 0.125%/h (first 2 hours). Subsequently, an apparent precipitation of C_3A is detected, which finishes 17 hours after hydration, when dissolution re-starts slowly between 17 and 25 hours (0.06%/h), increase its rate up to 0.16%/h till 40 hours and then slows again until the end of detection (0.03%/h).

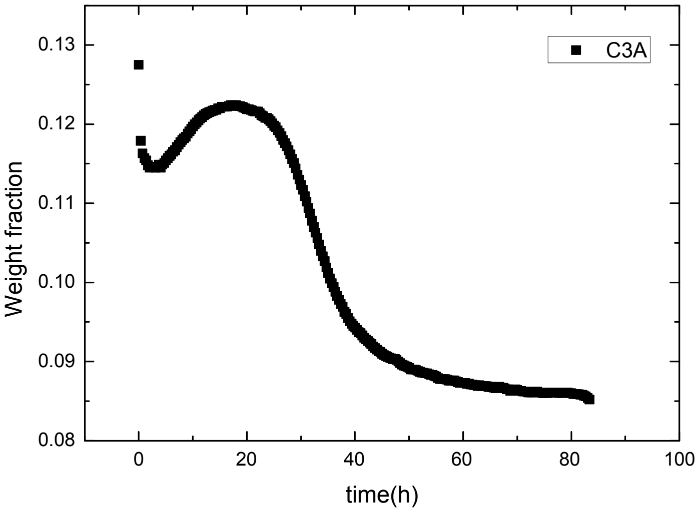

Figure 4.16: dissolution kinetic of C_3A in mix 2.

Gypsum dissolution progress at a rate of 0.17% per hour completing the depletion after 17 hours (figure 4.7). As in mix 1, gypsum depletion signs the increase in C_3A dissolution rate.

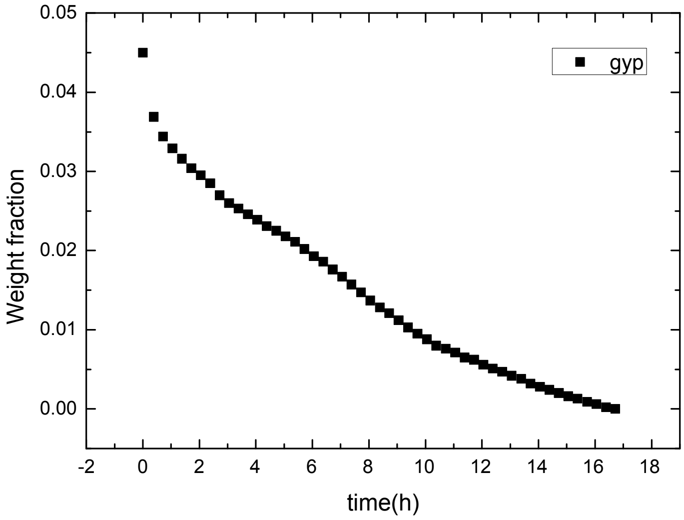

Figure 4.17: dissolution kinetic of gypsum in mix 2.

Ettringite precipitates from the beginning of hydration up to 39 hours, when it starts to dissolve. From 0 to 11 hours the precipitation rate is 0.3%/h while between 11 and 39 hours it decreases to 0.1%/h. The dissolution rate, when all the sulphate source is extinguished, is almost constant (0.014%/h) up to the end of detection (figure 4.8).

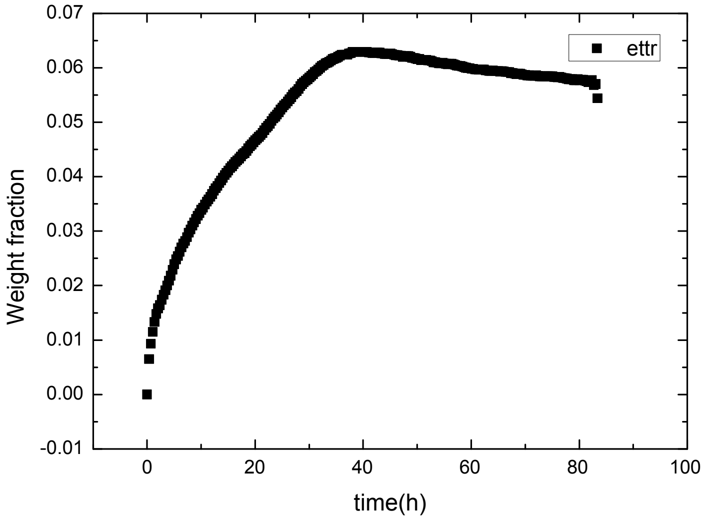

Figure 4.18: precipitation and subsequent dissolution kinetic of ettringite in mix 2.

C_3S kinetic is characterized by an initial apparent precipitation and a subsequent dissolution that starts after 3 hours and lasts till the end of detection. The acceleration in dissolution rate (0.75%/h) lasts 12 hours, from 3 to 15 hours after the beginning of hydration. This period is followed by a deceleration in dissolution rate, 0.25%/h between 15 and 29 hours and 0.03% till the end of detection (figure 4.9).

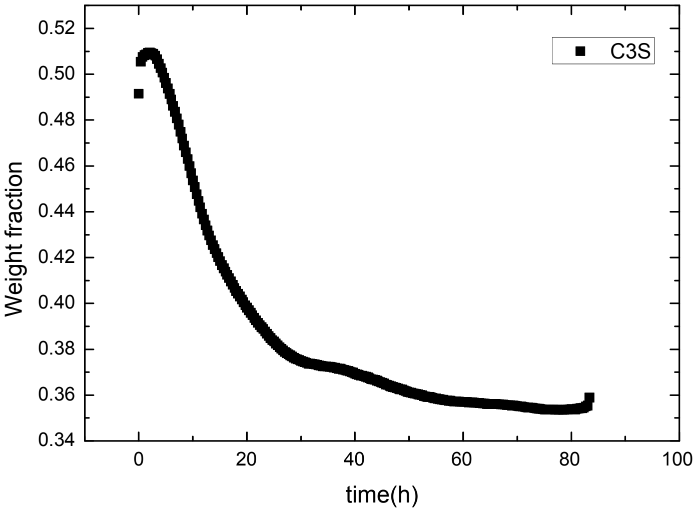

Figure 4.19: dissolution kinetic of C_3S in mix 2.

Portlandite precipitation shows a correlation with the variations in C_3S dissolution rate. The first period (3 – 15 hours) shows a precipitation rate of 0.25% of portlandite per hour; during the second period (15 – 50 hours), portlandite precipitates at a rate of 0.11%/h and finally in the last period the precipitation rate becomes much slower (0.003% per hour).

C-S-H precipitates at a rate of 0.63%/h between 3 and 15 hours; at 0.24%/h between 15 and 39 hours and finally at 0.06% per hour up to the end of detection. Portlandite and C-S-H kinetics are shown in figure 4.10.

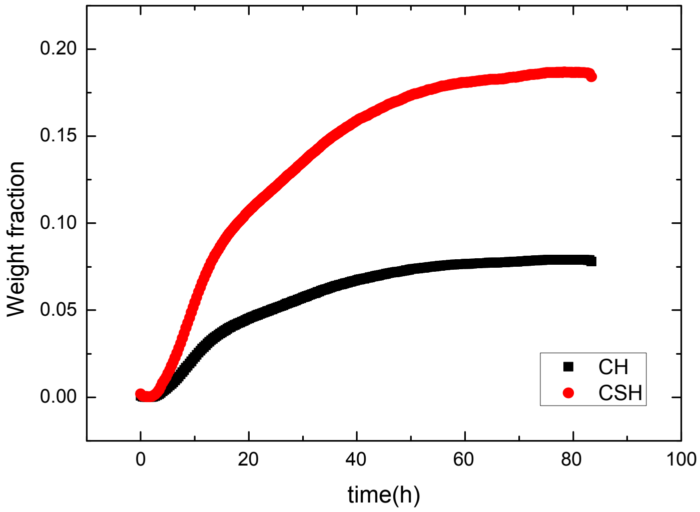

Figure 4.20: Portlandite (black squares) and C-S-H (red dots) precipitation kinetics in mix 2.

4.1.3 Mix 3

In figure 4.11 C_3A dissolution starts when powder is mixed with water but, after 3 hours, it shows an apparent increase, which lasts until all the gypsum is depleted (46 hours). The dissolution becomes visible first at 0.02%/h from 46 hours till 75 hours, when an increase in dissolution rate occurs: 0.13%/h up to 94 hours. The C_3A deceleration period (0.05%/h) starts after 94 hours.

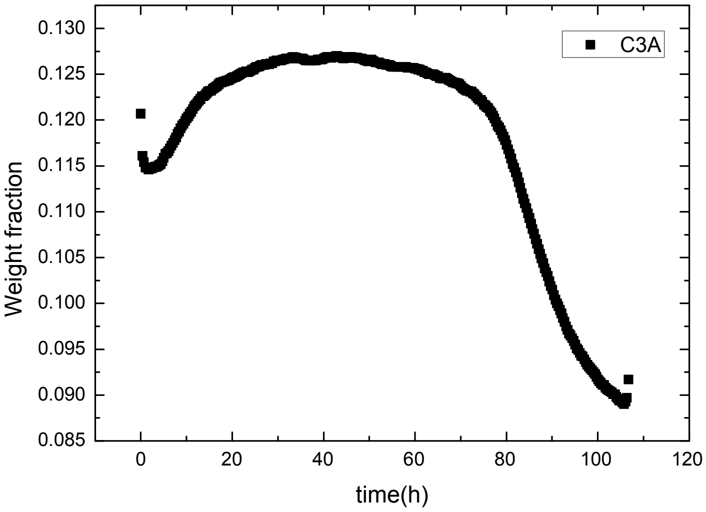

Figure 4.21: dissolution kinetic of C_3A in mix 3.

Gypsum complete depletion occurs after 46 hours. The initial dissolution rate is 0.2% of material per hour within 10 hours. Between 10 and 46 hours this rate is slower: 0.09% of gypsum per hour (figure 4.12).

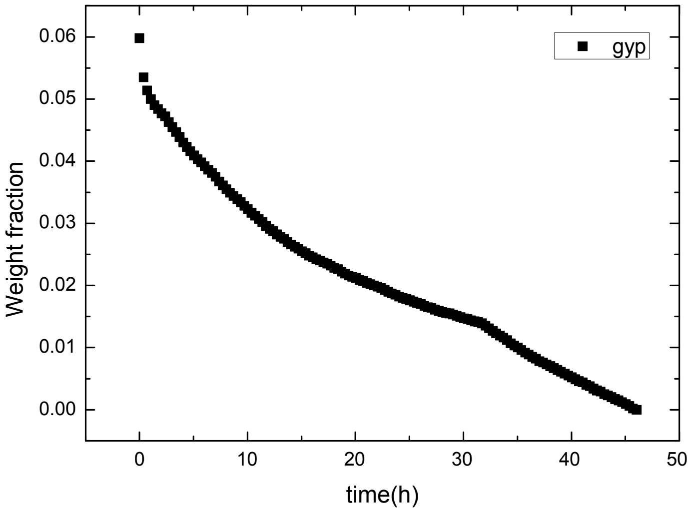

Figure 4.22: dissolution kinetic of gypsum in mix 3.

Ettringite precipitation shows a continuous increase up to 90 hours at 0.09%/h rate. From 90 hours after the beginning of hydration till the end of the measurement, ettringite dissolves with a constant dissolution rate of about 0.03%/h (figure 4.13).

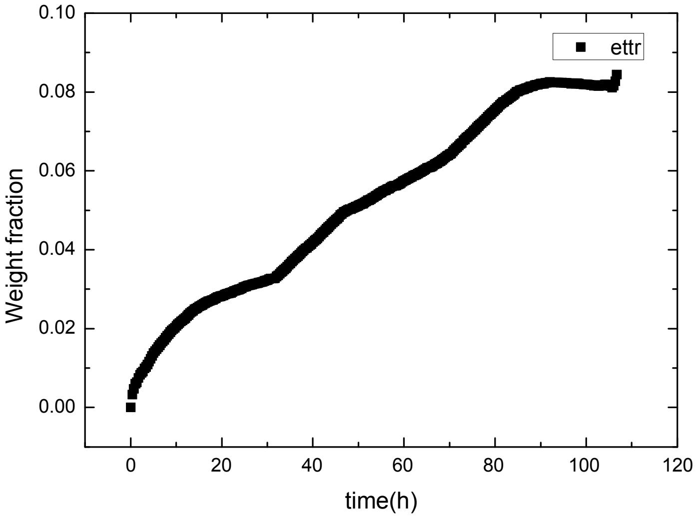

Figure 4.23: precipitation and subsequent dissolution kinetics of ettringite in mix 3.

C_3S kinetic shows an apparent precipitation within the first 3 hours. After this period, the dissolution becomes much evident, showing a dissolution rate of 0.7%/h between 3 and 16 hours. The subsequent deceleration period is characterized by 2 different dissolution velocities: the first period is between 16 and 78 hours, with a dissolution rate of 0.11%/h and the last period, up to the end of the measurement, when the dissolution rate is very close to zero (figure 4.14).

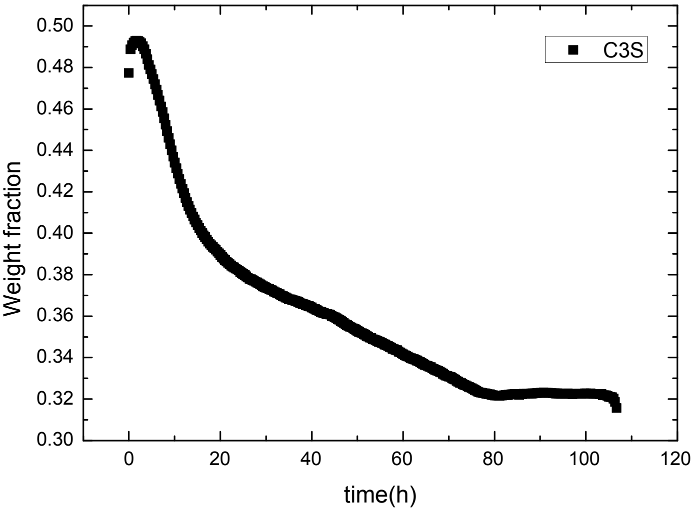

Figure 4.24: dissolution kinetic of C_3S in mix 3.

Portlandite precipitates during the whole measurement. Two periods can be distinguished: between 3 and 15 hours with a precipitation rate of about 0.33%/h and between 15 and 106 hours with a slower precipitation rate of about 0.04%/h. C-S-H shows the same behaviour of portlandite, but assuming higher precipitation rates. During the first period, between 3 and 16 hours, the precipitation rate is 0.65%/h while during the second period (16 – 106 hours) the precipitation rate is much slower: 0.12% of C-S-H per hour.

CH and C-S-H kinetics are shown in figure 4.15.

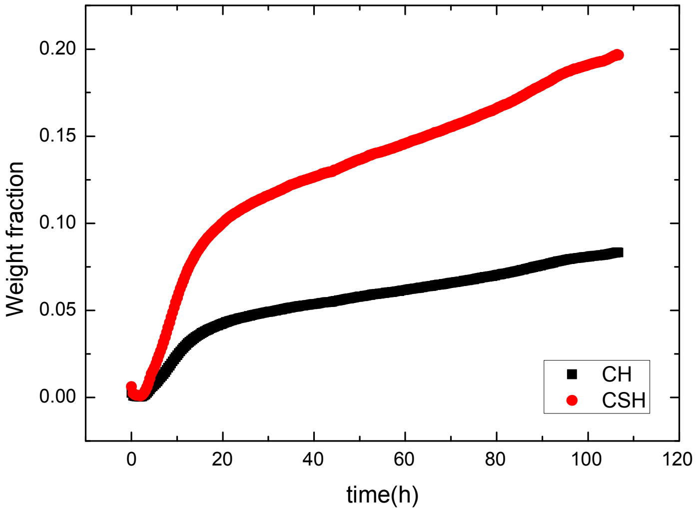

Figure 4.25: Portlandite (black squares) and C-S-H (red dots) precipitation kinetics in mix 3.

4.2. Isothermal calorimetry on pastes

As mentioned in chapter 3, isothermal calorimetry measurements have been performed at four different temperatures. Firstly, the experiment took at 23°C will be described because it is strictly related to XRD measurement and secondly the effect of temperature on dissolution/precipitation kinetics will be treated.

4.2.1 Mix 1

At 23°C the heat flow curve vs. time shows a single intense peak of 12 mW/g after 6.5 hours, with a small shoulder occurring after 10 – 12 hours of about 3 mW/g (figure 4.16). This intense peak can be related to C_3A acceleration in dissolution rate while the small shoulder can be considered as the expression of C_3S increase in dissolution rate.

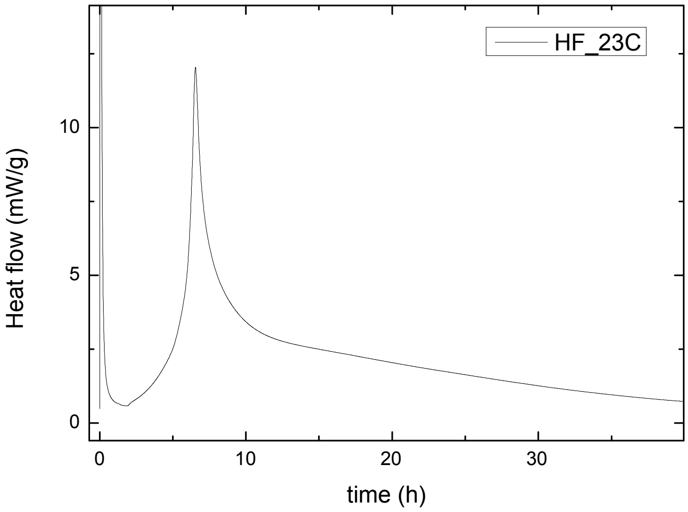

Figure 4.26: heat flow produced by mix 1 hydration at 23°C.

Considering all the measured kinetics at different temperatures (figure 4.17), a typical Arrhenius effect can be observed: at increasing temperatures, kinetics become faster. In fact, when the temperature inside the calorimeter is raised, the acceleration in C_3A dissolution occurs 8.5 hours after the beginning of hydration at 20°C, 6.5 hours at 23°C, 5.9 hours at 26°C and 5.8 hours at 32°C. C_3S acceleration is more difficult to detect, because this "shoulder" on the heat flow is not so evident. It can be deduced after 15 hours at 20°C, 11 hours at 23°C, 10 hours at 26 °C and 4.7 hours at 32°C. At 32°C, it is no more a "shoulder" but a peak with a precise intensity (7.4 mW/g), which occurs even before the same acceleration period of C_3A dissolution, actually inverting the previous order (C_3A acceleration in dissolution first, C_3S second).

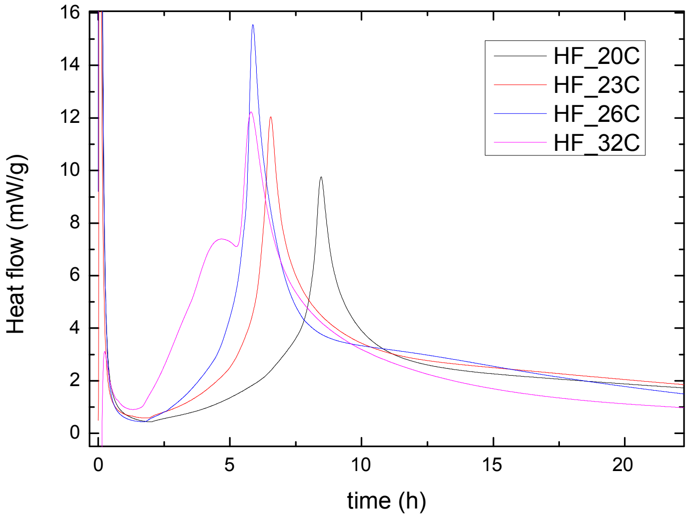

Figure 4.27: measured heat flow of mix 1 hydration at 4 different temperatures: 20°C (black), 23°C (red), 26°C(blue) and 32°C(pink).

4.2.2 Mix 2

At 23°C mix 2 heat flow present two main hydration peaks: the former occurs after 7.6 hours with an intensity of 3.76 mW/g while the latter after 32.9 hours with an intensity of 3.47 mW/g. These two hydration peaks can be easily correlated with C_3S increase in dissolution rate and C_3A increase of dissolution rate, respectively (figure 4.18).

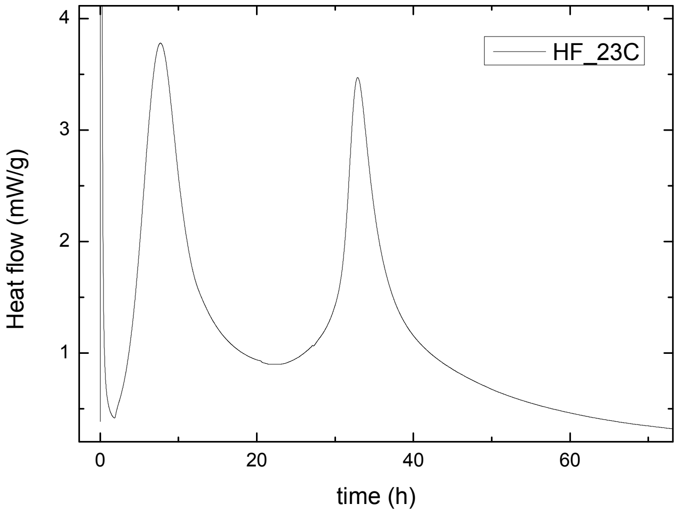

Figure 4.28: heat flow of mix 2 paste measured at 23°C.

As in mix 1, kinetics become faster when temperatures are increased. C_3S calorimetric peak occurs after 9.25 hours with an intensity of 2.96 mW/g at 20°C, after 7.7 hours and 2.8 mW/g at 23°C, after 6.5 hours and 4.4 mW/g at 26°C, after 4.6 hours and 5.7 mW/g at 32°C. Temperature affects these peaks also by increasing their absolute intensities.

C_3A calorimetric peak occurs after 50.4 hours with an intensity of 2.3 mW/g at 20°C, after 32.8 hours and 3.5 mW/g at 23°C, after 25.2 hours and 4.1 mW/g at 26°C, after 15.5 hours and 6.3 mW/g at 32°C. As for C_3S dissolution, Temperature affects these peaks also by increasing their absolute intensities. (figure 4.19).

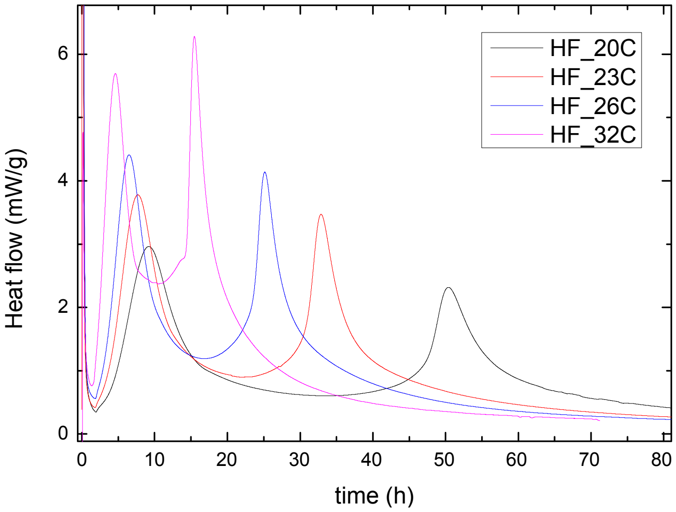

Figure 4.29: measured heat flow at 20°C (black), 23°C (red), 26°C(blue) and 32°C(pink) for mix 2 pastes.

4.2.3 Mix 3

At 23°C, two different calorimetric peaks (as in mix 2 heat flow) can be detected, the first after 7.8 hours with an intensity of 3.7 mW/g and the second after 88.8 hours with the intensity of 2.7 mW/g. The former is related to the increase in C_3S dissolution rate while the second to the increase in dissolution rate of C_3A (figure 4.20).

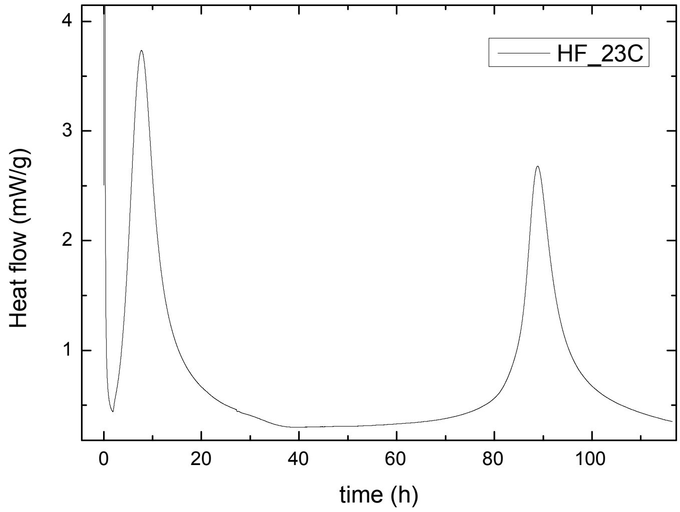

Figure 4.30: heat flow of mix 3 paste measured at 23°C.

As previously described, the same Arrhenius effect can be seen also in mix 3. The calorimetric peak related to C_3S occurs after 9.4 hours and with an intensity of 2.8 mW/g, after 7.8 hours and 3.7 mW/g at 23°C, after 6.5 hours and 4.3 mW/g at 26°C, after 4.7 hours and 5.8 mW/g at 32°C. On the other hand, the peak related to C_3A is occurs much later: after 143.6 hours and 1.7 mW/g at 20°C, after 88.9 hours and 2.7 mW/g at 23°C, after 73.6 hours and 3.3 mW/g at 26°C, after 35.8 hours and 6.3 mW/g at 32°C (figure 4.21).

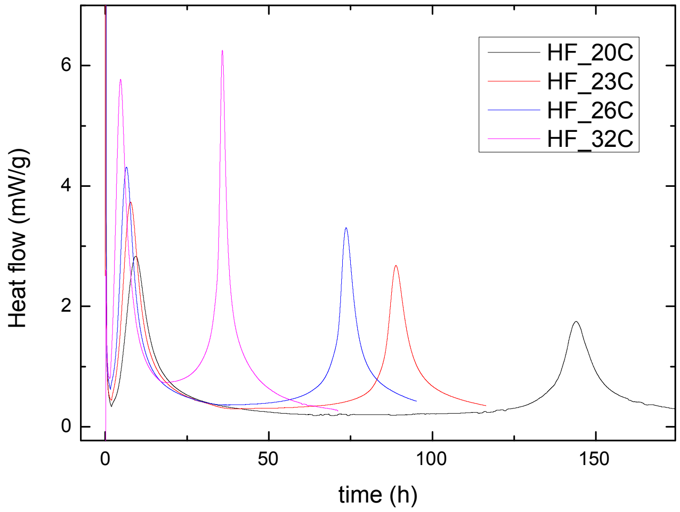

Figure 4.31: measured heat flow generated by mix 3 pastes at 20°C (black), 23°C (red), 26°C(blue) and 32°C(pink).

4.3. Calculation of kinetic parameters

Alexandra Quennotz [10] describes, on chapter 3.6 of her Ph.D. thesis, the influence of temperature on hydration kinetics. In particular, on chapter 3.6.1, she explains how to calculate the activation energy for a C_3A-Gypsum system, but the calculation can be extended to any cementitious system. The method is set on the calculation of equivalent age based on the maturity concept described by Carino [11].

Poole et al. [12] summarize three different methods for activation energy calculation: the first deals with single linear approximation of reaction rate, the second discusses about incremental calculation of activation energy and the third is a modified ASTM C1074 model.

Hardison et al. [13] describe how to calculate the activation energy for ultra-high-molecular-weight polyethylene (UHMWPE) using isothermal calorimetry.

Hereafter a brief explanation about each of above methods will be provided.

Quennotz method

The Quennotz method for activation energy calculation, as described in her Ph.D. thesis, is taken from the maturity method calculation described by Carino [11].

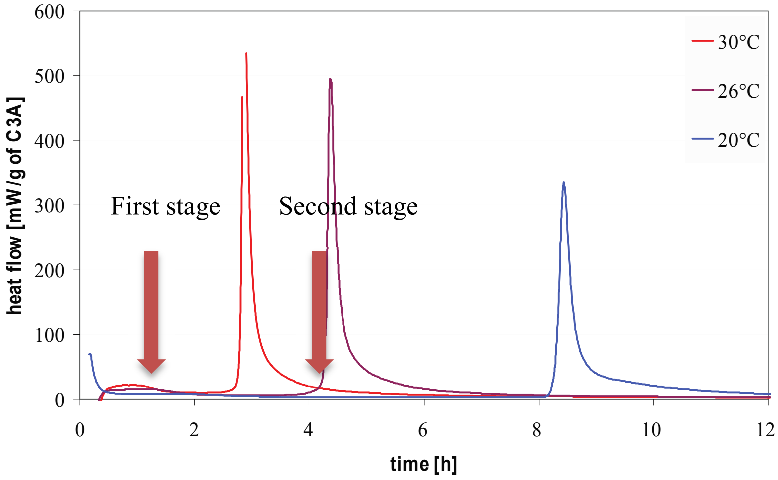

Figure 4.32: first stage (before gypsum consumption) and second stage (after complete gypsum dissolution) isothermal calorimetry for red curve [1] .

The method was developed for modelling the strength behaviour of cements taking into account the combined effects of time and temperature, from the very beginning of hydration process to long term curing. In our calculation, the maturity method becomes useful because it includes some specific equations to calculate the activation energy of cement-water reactions.

The hydration kinetic study is divided into two stages (figure 4.22), the former involving the complete sulphate dissolution while the latter considering the cement hydration with no solid sulphate phase present.

Practically, the first stage calculation is given by mathematic superposing the heat evolution curves using the formula:

$$t_{eq} = \alpha \cdot t \tag{4.2}$$

Where α is the proper age conversion factor to superpose the total heat curves, t is the measured paste age and t_{eq} is the equivalent age: it represents the duration of the curing period at the reference temperature that would result in the same maturity as the curing period at other temperatures [11]. Concerning to the second hydration stage, the heat flow curves are considered and a β coefficient is added to overlap the positive slope of heat peaks:

$$t_{eq} = \alpha \cdot (t + \beta) \tag{4.3}$$

Where α is again the proper age conversion factor to superpose the total heat curves. To calculate the activation energy is sufficient to apply equation (4.4):

$$E_a = -\frac{\ln(\alpha) \cdot R}{\left(\frac{1}{T} - \frac{1}{T_{ref}}\right)} \tag{4.4}$$

Where α is the only calculated parameter. This is how, visually, the curves are mathematically superposed:

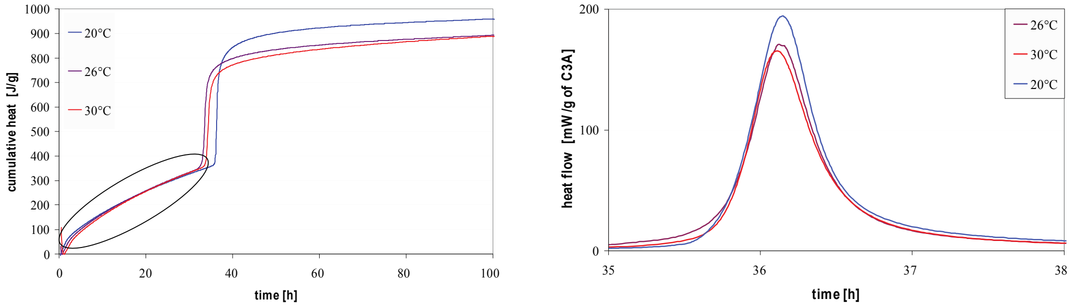

Figure 4.33: mathematical superposition of total heat curves for first stage E_a calculation using equation (4.2) (left) and for the second stage using equation (4.3) (right), [10].

Single linear approximation method of reaction rate

This method is based on the single linear approximation of the acceleration period of a calorimetric peak (figure 4.24).

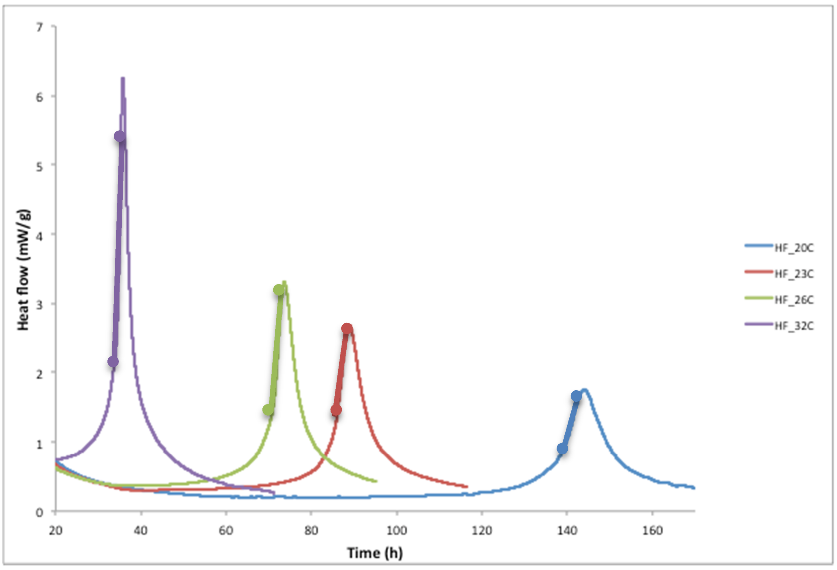

Figure 4.34: visual representation of single linear approximation method

Practically, the best linear fit of acceleration period is performed: the angular coefficient is equal to the maximum reaction rate *k*. A classical Arrhenius plot ln(k) vs. 1/T can be drawn and the linear fit of data can be performed. The negative of the slope multiplied by the gas constant returns the activation energy. The method to obtain k is explained by figure 4.24.

Incremental activation energy method

Since cement hydration is a continuous process, continuously varying activation energy can also be considered, because the dissolution/precipitation processes lead to a variation of phases. The incremental activation energy method consists on calculating the activation energy at any hydration step. The result is a curve that represents the variation of activation energy, which depends on the degree of hydration.

To perform this method is then necessary to measure the heat flow at constant degrees of hydration. In my case the only fixed parameter is temperature and this is the reason why an incremental activation energy calculation is not applicable for my experiments.

Modified ASTM C1074 method

The original ASTM C1074 method, proposed by Tank et al. [14], determines the activation energy using mechanical strength data on mortars cured at three different temperatures. The activation energy can also be calculated using isothermal calorimetry and a similar method has been developed.

The ASTM C1074 method uses an asymptotic approximation to describe the mechanical strength trend data. An important limitation of the asymptotic approximation is that it assumes that the property being studied assumes a zero value since the paste is not set. Such limitation is overcome by using an exponential approximation of this form:

$$\alpha(t_e) = \alpha_u \cdot e^{-[\frac{\tau}{t_e}]^{\beta}} \tag{4.5}$$

Where τ equals the chronological age while t_e is the equivalent age. The relationship between τ at the reference temperature (chosen arbitrary) and τ at the test temperature is equivalent to the relationship between t and t_e:

$$\frac{t_e}{t} = f(T_c) = \frac{k(T_c)}{k(T_{ref})} = \frac{\tau_{ref}}{\tau_c} \tag{4.6}$$

Where τ_c equals the hydration time parameter at temperature of concrete T_c, τ_{ref} is the hydration time parameter at reference temperature T_{ref}, $f(T_c)$ is the age conversion factor, $k(T_c)$ is the reaction rate at the temperature of concrete T_c, $k(T_{ref})$ equals the reaction rate at the reference temperature T_{ref}. From equation (4.6) we can find the relation for calculating the activation energy:

$$E_a = -\frac{\ln(\frac{\tau_{ref}}{\tau_c})}{(\frac{1}{T_{ref}} - \frac{1}{T_c})} \cdot R \tag{4.7}$$

The E_a value is obtained firstly fitting the degree of hydration curve using equation (4), where τ is given by the fit. Secondly, an Arrhenius plot ln(τ) vs. 1/T can be drawn and finally E_a is given by multiplying the negative of the angular coefficient of data fit and the gas constant.

Hardison method

In his paper Hardison et al. [13] describe a very simple way to calculate activation energy. In practice, using the calorimetric peak height as the maximum reaction rate and measuring the same material at different temperatures, it is possible to draw an Arrhenius plot from where an activation energy value can be calculated. In my case I have 2 distinct events, so 2 distinct values of Ea can be obtained. This is not true for mix 1, where the 2 events almost coincide. For this reason only mix 2 and 3 activation energies will be reported.

The high amount of Gypsum induces two well-separated heat peaks, the former related to C_3S dissolution while the latter to C_3A dissolution, and this is the reason why the modified ASTM C1074 method cannot be applicable to these systems.

I used the isothermal calorimetry technique to measure the hydration kinetics. For each mix the heat flow and the total heat of hydration have been measured until the two calorimetric peaks appeared.

To summarize better the results, hereafter they will be subdivided starting from the method used.

Quennotz Method

With this method for each calorimetric measurement, activation energy has been calculated, excluding the measurement taken at the reference temperature (20°C). Results are summarized in table 1:

	FIRST STAGE (KJ/mol)	SECOND STAGE (KJ/mol)	MEAN VALUE (KJ/mol)
MIX 1	62	3	32.5
MIX 2	62	24	43
MIX 3	65	6	35.5

Table 4.5: Quennotz method data for mix NIST. First stage: before gypsum consumption. Second stage: when gypsum is totally ended up into solution.

For mix 1, first stage, I had only one reasonable datum while all the others are mean values between the three different values related to each different temperature measured. Considering the first stage, activation energy is almost constant for all mixtures while for the second stage it becomes very different from a mix to another. For mix 1 and 3 transport controlled reactions (<20 kJ/mol, [10]) seem to act while in mix 2 a surface controlled mechanism (>20 KJ/mol, [10]) seems to be more reasonable.

Single linear approximation method

As described on the introduction, activation energy calculation is performed for two stages: the first is related to the system before Gypsum dissolution, the second to the system when the Gypsum dissolution has come to an end. In particular, the single linear approximation method is applied to the positive slope of every single, well-separated, peak.

Results are summarized in table 2:

	FIRST STAGE (KJ/mol)	SECOND STAGE (KJ/mol)	MEAN VALUE (KJ/mol)
MIX 1		121	101 (hypothetical)
MIX 2	81	123	102
MIX 3	82	167	124.5

Table 4.6: Single linear approximation method data for mix NIST. First stage: before gypsum consumption. Second stage: when gypsum is totally ended up into solution.

Activation energy calculation for mix 1 first stage cannot be performed because peaks are not separated and the contribution to heat flow from C_3A dissolution is much higher than C_3S dissolution within 5 hours. It can be noted that for the first stage the activation energy remain constant while for the second stage it increases at increasing Gypsum content.

Modified ASTM C1074 method

Although this is the most efficient method, since it models all the degree of hydration trend, it can be applied only to mix 1. It shows the most similar degree of hydration evolution of a Portland cement and this trend is well fitted by equation (4.5). Mix 2 and 3 show a degree of hydration that cannot be modelled by an exponential function.

Finally, the activation energy for mix 1 is 33 KJ/mol.

Hardison Method

In table 3 I summarized the activation energies calculated using the Hardison method.

	FIRST STAGE (KJ/mol)	SECOND STAGE (KJ/mol)	MEAN VALUE (KJ/mol)
MIX 1			
MIX 2	39	59	49
MIX 3	41	81	61

Table 4.7: Hardison method data for mix NIST. First stage: before gypsum consumption. Second stage: when gypsum is totally ended up into solution.

Even if not reported, an estimate of second stage E_a for mix 1 returned an overestimated (because the contribution of first stage reactions cannot be removed) value of 57 KJ/mol.

Both first and second stages seem to be dominated by surface controlled reactions (>20 KJ/mol) [10]. Again while for the first stage reactions the E_a values are almost constant, for second stage reactions activation energy values increase with increasing Gypsum content.

Mean values obtained from these calculations can be considered within usual values published in literature for ordinary Portland cements.

Avrami kinetic model

The Avrami model can be used to model nucleation and growth reaction kinetics in order to determine the general morphology of reaction products and the rate-limiting step of the reaction [15–18]. It has to be noted that the Avrami model fits well the acceleration stage of a dissolution reaction. When the nucleation and growth process switch into a diffusion controlled regime, the model is no longer valid [18–20]. The basic Avrami equation is:

$$\alpha(t) = 1 + \alpha_0 - e^{-k \cdot t^M} \tag{4.8}$$

Where α_0 is the degree of reaction at the time to when this nucleation and growth process becomes dominant and k is a rate constant that combines the effects of nucleation, multidimensional growth, geometric shape factors, and diffusion. The exponent M is related to the nature of the reaction through the parameters P, Q, and S:

$$M = \frac{P}{S} + Q \qquad (4.9)$$

where P is related to the dimensionality of the product phase: P = 3, P = 2, and P = 1 corresponding to the growth of polygonal forms, sheets, and fibres (needles), respectively. Similarly, S describes the type of growth, with S = 1 corresponding to interfacial or phase boundary growth and S = 2 corresponding to diffusion of components though the liquid phase. Finally, Q is related to the nucleation rate: Q = 0 for no nucleation and Q = 1 for constant nucleation.

The application of the Avrami model to our blends has been divided in two parts, one for each acceleration period observed. Measuring the hydrating pastes at different temperature permits to calculate the activation energy of each dissolution reaction: three temperature are sufficient to produce an Arrhenius plot and to calculate the activation energy. In the next table the whole set of parameters is shown.

	Temp	Heat flow first acceleration			Heat flow second acceleration		
	°C	k	M	E_a (KJ/mol)	k	M	E_a (KJ/mol)
Mix 1	20	5.19E-04	2.4	52.5			
	23	4.03E-04	2.8				
	26	3.37E-04	3.0				
	32	1.67E-02	1.4				
Mix 2	20	3.67E-04	2.3	87.4	4.58E-03	1.1	48.2
	23	3.97E-04	2.4		8.80E-03	1.3	
	26	8.75E-04	2.3		9.71E-03	1.2	
	32	1.35E-03	2.4		9.92E-03	1.4	
Mix 3	20	4.46E-04	2.3	85.5	2.68E-03	1.2	64.6
	23	4.69E-04	2.5		5.17E-03	1.2	
	26	1.41E-03	2.1		4.81E-03	1.3	
	32	1.63E-03	2.5		8.60E-03	1.2	

Table 4.8: summary data of Avrami fit on the acceleration part of the degree of hydration of mix 1, 2 and 3, as calculated from isothermal calorimetry.

It has to be noted that mix 1 kinetic parameters are obtained considering only one acceleration period, because only one definite peak can be detected. Avoiding kinetic data calculated at 32°C (when a more definite peak starts to appear), the constant *k* decreases with increasing temperature. It is a strange behaviour probably because the model is applied to two competitive systems (C_3A dissolution and C_3S dissolution) which cannot be treated separately. The *M* value is close to 3, which is consistent with (P, S, Q) = (3, 1, 0) that is polygonal product phase, phase boundary growth with no nucleation. It is also consistent with (P, S, Q) = (2, 1, 1) that is plate-type product phase and phase boundary growth with constant nucleation.

Mix 2 data, related to the first acceleration period, show an increase in of *k* values with increasing temperature. The *M* value can be approximated to 2, which is consistent with (P, S, Q) = (2, 1, 0) and (P, S, Q) = (2, 2, 1) that is plate-type product phase and phase boundary growth with constant nucleation or diffusion controlled growth with no nucleation. It is also consistent with (P, S, Q) = (1, 1, 1); needle-type product phase morphology, phase boundary growth, and constant nucleation.

The fit of second acceleration period of mix 2 conducts to *M* = 1, with (P, S, Q) = (1, 1, 0) or (P, S, Q) = (2, 2, 0) that is fibres products and phase boundary growth with no nucleation or sheet products with diffusion of components through the liquid phase and no nucleation.

Mix 3 data, related to the first acceleration period, show an increase in of *k* values with increasing temperature. The *M* value can be approximated to 2, which is consistent with (P, S, Q) = (2, 1, 0) and (P, S, Q) = (2, 2, 1) that is plate-type product phase and phase boundary growth with constant nucleation or diffusion controlled growth with no nucleation. It is also consistent with (P, S, Q) = (1, 1, 1); needle-type product phase morphology, phase boundary growth, and constant nucleation.

The fit of second acceleration period of mix 2 conducts to *M* = 1, with (P, S, Q) = (1, 1, 0) or (P, S, Q) = (2, 2, 0) that is fibres products and phase boundary growth with no nucleation or sheet products with diffusion of components through the liquid phase and no nucleation.

Excluding mix 1, it is possible to see that the activation energy related to the first acceleration period is similar between mix 2 and 3 while an increase is seen passing from mix 2 to mix 3 activation energy of the second acceleration period.

4.4. Recalculation of heat flow from XRD data

In cement research and, in particular, in industrial applications one of the most effective and easiest technique to use is isothermal calorimetry. In general, the proper way to obtain effective kinetic data is to investigate the hydrating pastes by means of calorimetric techniques. Recently it has been introduced by some authors [21–23] the possibility to obtain qualitative calorimetric data by using the kinetics derived from *in-situ* x-ray powder diffraction and thermodynamic data. These calculations are based on the quantitative phase analysis with the external standard procedure described by O’Connor and Raven [2] by which all the crystalline phases and the sum of non-crystalline compounds can be determined. Two of the cited studies are performed on pure alite: a monophase system is more simple to be treated because the C_3S dissolution and portlandite/C-S-H precipitation is the only reaction involved.

When multiple reactions are involved, such as in our experiments, the interactions between the dissolving phases present problems that are not completely understood.

We decided to use a different approach based on the Rietveld scale factor, which is a direct measure of the kinetic of a phase. Isothermal calorimetry data are the reference to see how our calculations differ from the true values.

The degree of hydration α_{IC} of a paste, in isothermal calorimetry, is the ratio between the measured total heat H(t) (J/g) from time 0 to time t and the total amount of heat that can be potentially released by the considered paste, H_u (J/g) [4, 11–15]:

$$\alpha_{IC}\,(t) = \frac{H(t)}{H_u} \tag{4.10}$$

The value H_u is a function of cement composition and amount and type of supplementary cementing materials (SCMs) and may be calculated as follows [4, 11]:

$$H_u = H_{cem} \cdot P_{cem} + 461 \cdot P_{slag} + 1800 \cdot P_{FA-CeO} \cdot P_{FA} \tag{4.11}$$

where P_{slag} equals slag mass to total cementitious content ratio, P_{FA} equals fly ash mass to total cementitious content ratio, $P_{FA\text{-}CaO}$ equals fly ash CaO mass to total fly ash content ratio, P_{cem} equals cement mass to total cementitious content ratio, and H_{cem} equals heat of hydration of the cement (J/gram). The value H_{cem} can be calculated as shown in equation 4.12 [29]:

$$H_{cem} = 500 \cdot P_{C_3S} + 260 \cdot P_{C_2S} + 866 \cdot P_{C_3A} + 420 \cdot P_{C_4AF} + 624 \cdot P_{SO_3} + 1186 \cdot P_{FreeCa} + 850 \cdot P_{MgO} \tag{4.12}$$

where H_{cem} equals the total heat of hydration of Portland cement (J/gram) at $\alpha = 1.0$, and p_i equals the mass of i^{th} component to total cement content ratio [12]. Since in our blends no SCMs are added, equation (4.11) becomes:

$$H_u = H_{cem} \cdot P_{cem} \tag{4.13}$$

While equation (4.12), without all that phases that are absent from our systems, becomes:

$$H_{cem} = 500 \cdot P_{C_3S} + 866 \cdot P_{C_3A} + 624 \cdot P_{SO_3} \tag{4.14}$$

Degree of hydration can be directly calculated from calorimetric data but if we are able to obtain the same degree of hydration from XRD data, a recalculation of the generated heat flow can be performed. The initial assumptions are that the main contributors to the heat flow production are C_3S and C_3A dissolutions: these two kinetics are used for the calculation of heat flow.

Using the degree of hydration calculated from isothermal calorimetry, α_{IC}, as a reference we found the following relationships.

We can assume that the degree of hydration calculated from the Rietveld scale factor, α_{SF}, for each phase is:

$$\alpha_{SF}\,(t) = SF(t_0) - \frac{SF\,(t)}{SF(t_0)} \tag{4.15}$$

Where $SF(t_0)$ is the scale factor at the initial time t_0 and SF(t) is the scale factor at time *t*. In this way, both C_3S and C_3A degree of hydration can be calculated. It has to be proven which is the relationship (e.g., simple sum of the 2 degree of hydration, cumulative sum) that stands at the basis of the reference degree of hydration. Finally, with the calculated degree of hydration, it is possible to recalculate the generated heat flow.

If the degree of hydration calculated from isothermal calorimetry, α_{IC}, is equal to the degree of hydration calculated from the scale factor, α_{SF}:

$$\alpha_{IC} = \alpha_{SF} \tag{4.16}$$

And the measured heat flow (from isothermal calorimetry) is:

$$HF_{IC} = \alpha_{IC} \cdot H_u \tag{4.17}$$

Then, the calculated heat flow results:

$$HF_{SF} = \alpha_{SF} \cdot H_u \tag{4.18}$$

In the following sections we will refer to the degree of hydration calculated from the scale factors of both C_3S and C_3A with α_{C_3S} for and α_{C_3A}, respectively. All the calculated α_{SF} are affected by the "apparent precipitation" effect, which will be treated in the discussion section, that alters the initial part of the hydration, causing an apparent negative degree of hydration.

4.4.1 Mix 1

Comparing α_{IC} with α_{C_3A} and α_{C_3S}, we can see that up to 13 hours the hydration is completely dominated by C_3A dissolution and the contribution of C_3S seems not to be relevant. This further confirm what previously stated about the correlation of the first calorimetric peak with the dissolution of C_3A.

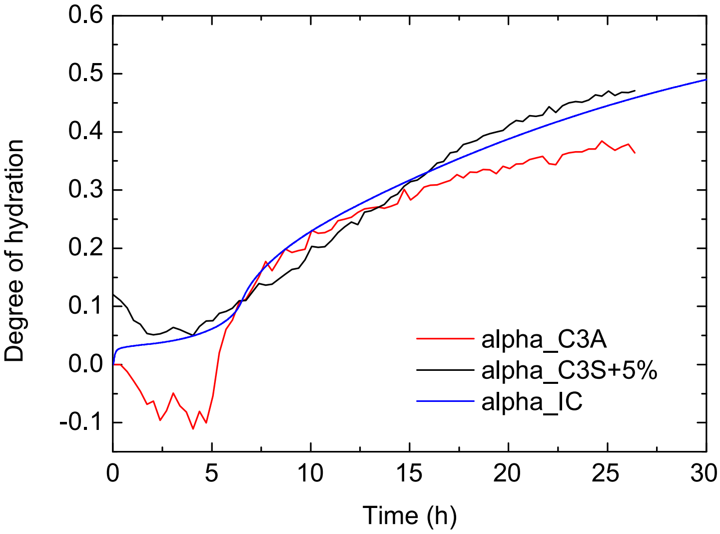

Figure 4.35: comparison between the degree of hydration calculated from isothermal calorimetry (alpha_IC) and the degree of hydration (alpha_C3A and alpha_C3S) calculated from the Rietveld scale factors.

The contribution of C_3S dissolution becomes remarkable after 13 hours, as we can see from figure 4.28. The total α_{SF} is not the simple sum of both α_{C_3A} and α_{C_3S}. We had to consider to split the contributions: up to 13 hours it is all α_{C_3A} while from 13 hours to 26 hours α_{C_3S} is the dominant part, but with a further contribution of α_{C_3A} of 5%. This means that during the hydration of C_3S, C_3A dissolution still influences the cumulative heat released.

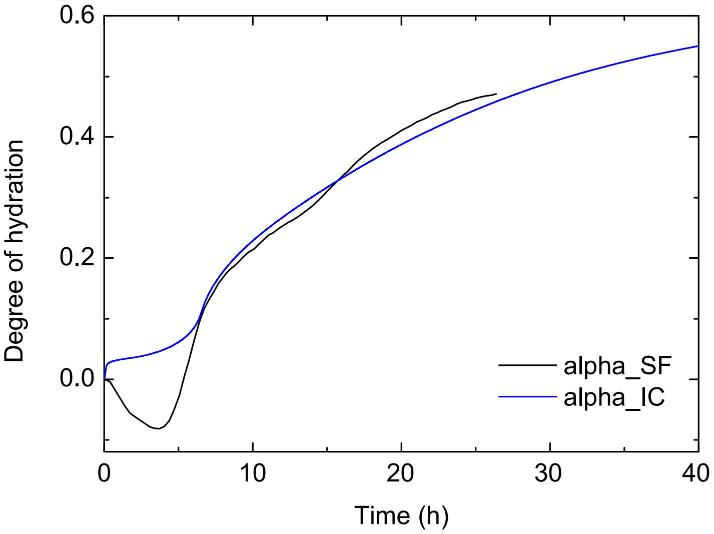

Figure 4.36: comparison between the degree of hydration calculated from isothermal calorimetry (blue) and from Rietveld scale factors (black). Adjacent-averaging smooth has been performed for the black curve.

With the calculated α_{SF}, it is now possible to recalculate the generated heat flow during the hydration of mix 1 (figure 4.30).

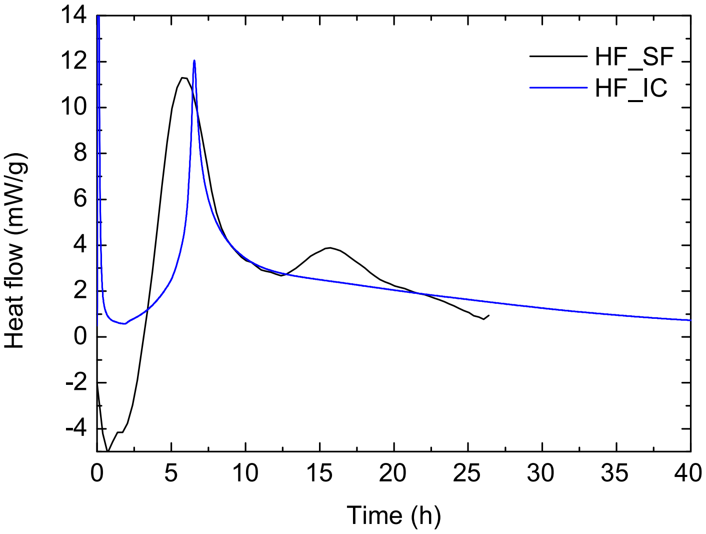

Figure 4.37: recalculation of generated heat flow starting from Rietveld scale factor (black) and comparison with measured heat flow through isothermal calorimetry (blue).

On one hand, it is possible to see a consistent difference between the measured heat flow and the calculated one (figure 4.30). It has to be noted that no further parameter (such as particle size distribution and specific surface) has been considered to calculate the heat flow. On the other hand, it is interesting to note that the peak height (especially for C_3A) is very close to the measured value: this means that the kinetic derived from x-ray diffraction is reliable.

4.4.2 Mix 2

Comparing α_{IC} with α_{C_3A} and α_{C_3S}, we can see that also here the hydration process can be split into two stages, each dominated by one of the considered dissolving phases. Such stages can be defined as follow:

- First stage starts at the beginning of hydration up to the first deceleration period
- Second stage lasts from the second acceleration period up to the end of the measurement

The first stage is dominated by the hydration of C_3S up to 30 hours, when the second acceleration occurs caused by C_3A (figure 4.31).

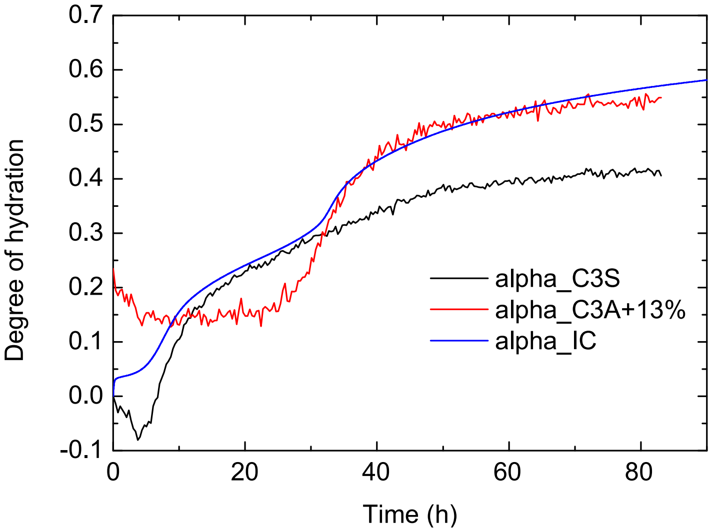

Figure 4.38: comparison between the degree of hydration calculated from isothermal calorimetry (alpha_IC) and the degree of hydration (alpha_C3A and alpha_C3S) calculated from the Rietveld scale factors.

After 30 hours the dominating phase results C_3A but C_3S continues to contribute to the total degree of hydration: such contribution is quantified to be of 13% of the total degree of hydration of the second stage (figure 4.32).

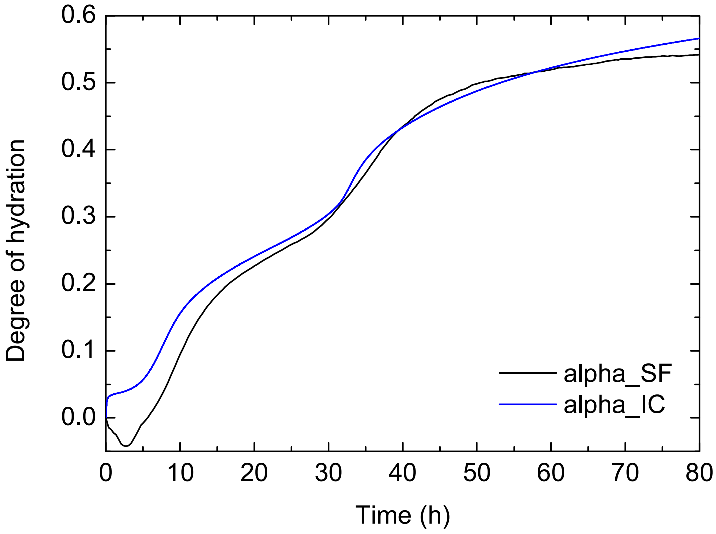

Figure 4.39: comparison between the degree of hydration calculated from isothermal calorimetry (blue) and from Rietveld scale factors (black). Adjacent-averaging smooth has been performed for the black curve.

With the calculated α_{SF}, it is now possible to recalculate the generated heat flow during the hydration of mix 2 (figure 4.33).

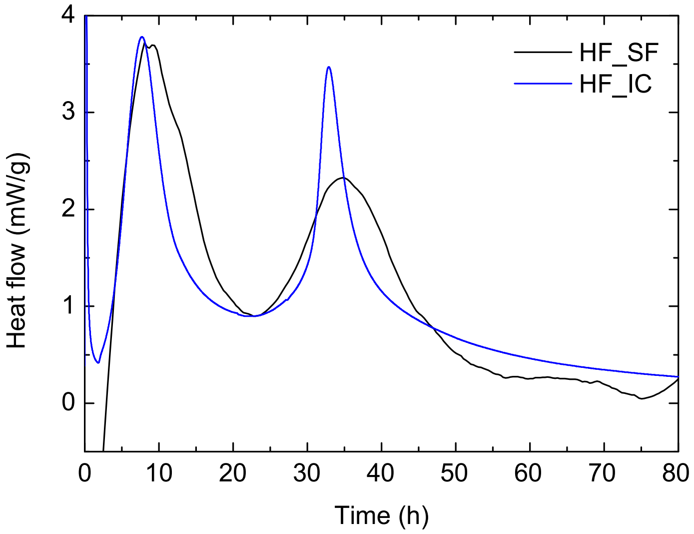

Figure 4.40: recalculation of generated heat flow starting from Rietveld scale factor (black) and comparison with measured heat flow through isothermal calorimetry (blue).

Heat flow calculated from α_{SF} shows a reliable absolute heat flow value for the first peak while the second absolute heat flow value is remarkably underestimated.

4.4.3 Mix 3

Very similar to mix 2, it differs for the time of occurrence of the events. From the beginning of hydration up to 87 hours, the hydration is almost entirely dominated by C_3S dissolution. From 87 hours up to the end of the measurement C_3A dissolution dominates the degree of hydration profile (figure 4.34).

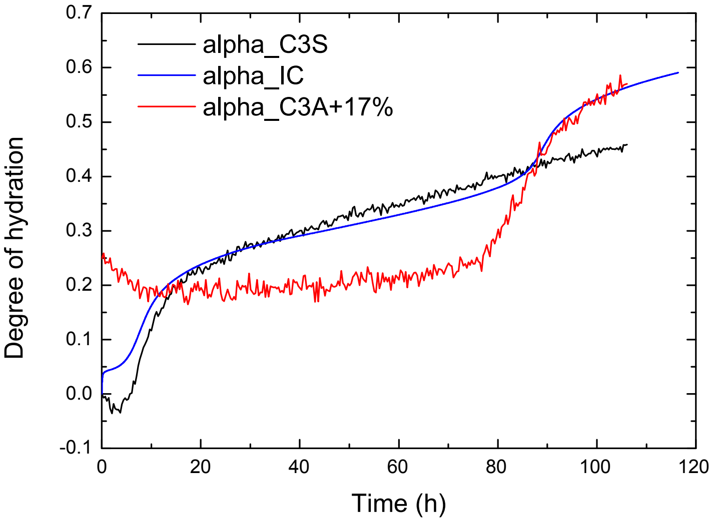

Figure 4.41: comparison between the degree of hydration calculated from isothermal calorimetry (alpha_IC) and the degree of hydration (alpha_C3A and alpha_C3S) calculated from the Rietveld scale factors.

When C_3A dissolution is the principal phenomenon, C_3S continues to contribute to the total degree of hydration: such contribution is quantified to be of 17% of the total degree of hydration of the second stage.

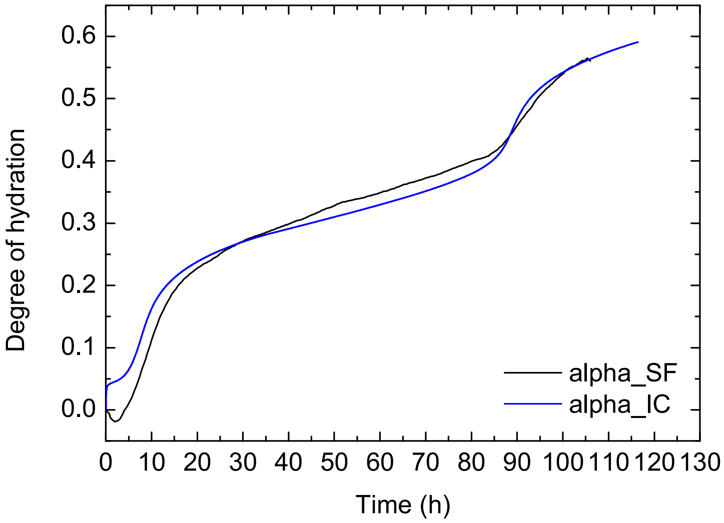

Figure 4.42: comparison between the degree of hydration calculated from isothermal calorimetry (blue) and from Rietveld scale factors (black). Adjacent-averaging smooth has been performed for the black curve.

With the calculated α_{SF}, it is now possible to recalculate the generated heat flow during the hydration of mix 3 (figure 4.36).

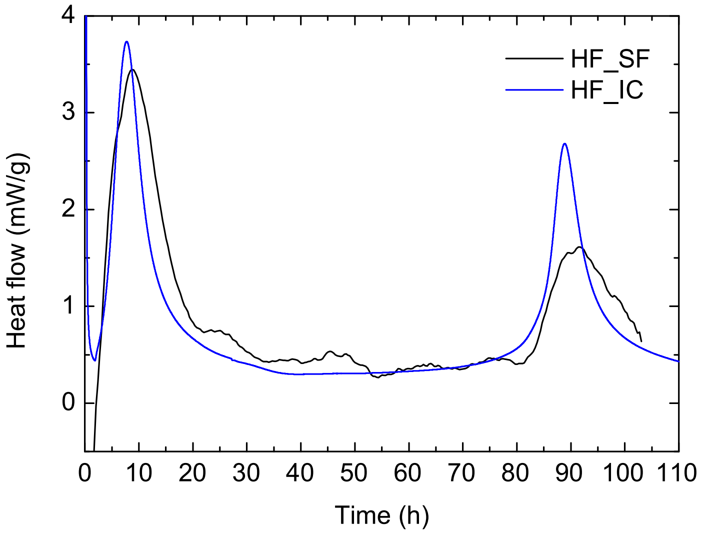

Figure 4.43: recalculation of generated heat flow starting from Rietveld scale factor (black) and comparison with measured heat flow through isothermal calorimetry (blue).

Heat flow calculated from α_{SF} shows a reliable absolute heat flow value, shape and time of occurrence for the first peak; the absolute heat flow value related to the second peak is remarkably underestimated but the time of occurrence is in agreement with measured heat flow.

4.5. Discussion

4.5.1 Apparent precipitation of C_3S and C_3A

The first thing that can be pointed out is the apparent precipitation observed in C_3A and C_3S dissolution kinetics. The reason why this can be referred just as "apparent" is the assumption of the chemical behaviour of C_3S and C_3A when mixed with water: in literature there is no evidence about a precipitation of material after an initial dissolution.

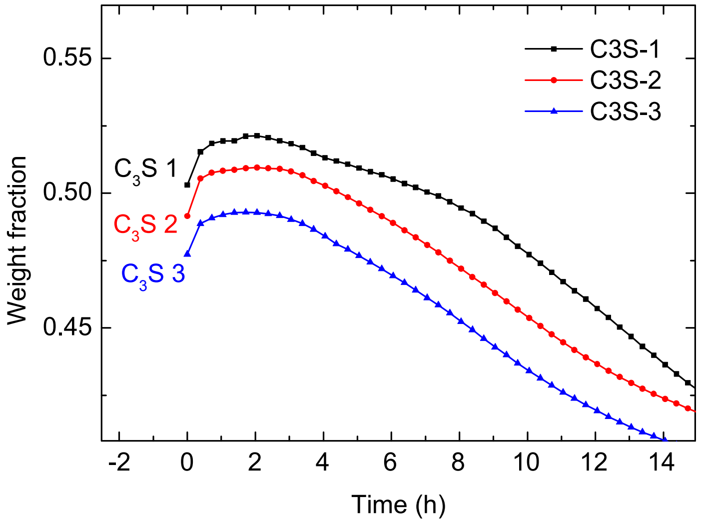

Figure 4.44: detail of C_3S kinetics showing the apparent precipitation effect detected during XRD measurement. Such effect is visible for all the blends within the beginning of hydration and 3 hours later. Mix 1: black squares, Mix 2: red rhombs; Mix 3: blue triangles

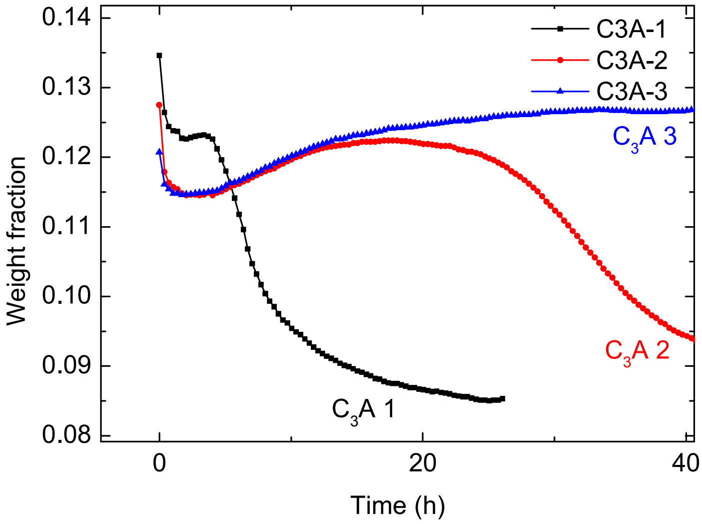

Figure 4.45: detail of C_3A kinetics showing the apparent precipitation effect detected during XRD measurement. Such effect is visible for all the blends from the beginning of hydration until the hydration rate of C_3A increases. Compared to C_3S, here the effect is enhanced and the duration is related to the initial gypsum quantity. Mix 1: black squares, Mix 2: red rhombs; Mix 3: blue triangles.

Thermodynamically speaking, C_3S and C_3A dissolution is much more favoured than precipitation. In this scenario, we tried to explain this behaviour with some hypothesis. When XRD data on cement pastes are considered, the variation in phase content during time can be due to:

1. Dissolution (or precipitation) of the phase
2. Absorption contrast between the cement phases, which overestimate the less absorbing phase [30–32]
3. Variation in the illuminated volume of the sample
4. The presence of an amorphous layer that alters the diffracted intensities [33]

Talking about C_3S and C_3A, we should see a continuous dissolution, with variations in the dissolution rate, but no precipitation. In fact, considering the Rietveld scale factor of both phases, we can see how the values decrease during all the measurement. But if we observe the quantitative phase analysis trend of both C_3S and C_3A, we can see how, initially, these 2 phases seem to precipitate (increase in weight %) while they should dissolve (decrease in weight %). This effect is much more enhanced in mix 2 and 3, where the quantity of gypsum present in the system is higher (mix 1 is not excluded, but the effect is less evident). Moreover, the apparent precipitation effect becomes larger in C_3A than in C_3S. These last two considerations can drive to consider gypsum as a main responsible for this effect. One possible explanation is given looking at the linear absorption coefficient of C_3S, C_3A and gypsum: in our experimental conditions, μ_{C3S}=252.24 cm^{-1}, μ_{C3A}=215.55 cm^{-1} and μ_{gy}=88.57 cm^{-1}. μ_{C3S} and μ_{C3A} values are very close but a significant difference can be encountered looking at the two couples C_3S-gypsum and C_3A-gypsum. During a period of slow dissolution rate of C_3S and C_3A and a higher gypsum dissolution rate, the more absorbing phase (C_3S or C_3A) becomes overestimated, leading to an "apparent precipitation" of the dissolving phase. This is in contrast from what stated in the literature [30–32], in which microabsorption problem affects the more absorbing phase (C_3S or C_3A) underestimating it, while the less absorbing phase (gypsum) becomes overestimated. So, the microabsorption problem seems not to be the principal cause of this "apparent precipitation" effect.

Another possible explanation derives from the variation of illuminated sample volume. During the experiment, the capillary sample rotates along the goniometer axis to increase the diffracted count statistics and only a certain part of the capillary is illuminated by the x-ray beam. We may suppose that a certain part of C3S and C3A, previously out of the investigated volume, enters the illuminated part of the sample causing an increase in the diffracted signal and, consequently, in quantitative analysis. In this way, the investigated volume is not kept constant during the measurement and the quantitative phase analysis cannot be considered reliable. Moreover, the centrifugal movement can force the material to the walls of the capillary, creating a laminar flux and a practically unchanged situation in the centre of the capillary [34]. Furthermore, the same apparent precipitation effect has been seen in other *in-situ* XRD experiments performed in Bragg-Brentano geometry by Hesse *et al.* [6, 7] and in our laboratory, discarding the rotation as the main responsible for this effect. For all these reasons, the variation of investigated volume can be reasonably discarded.

Our last hypothesis about the apparent precipitation of C_3S and C_3A during their dissolution is the formation of an amorphous layer, continuous or discontinuous, that envelope the grains. Gordon and Harris [33] studied the effect of particle size of quartz in the quantitative determination by x-ray diffraction. They report the presence of an amorphous layer that reduces the intensity of the (11-22) diffraction line when the size of quartz particle stands between 0.5 and 10 microns. They suggest that such layer is not a clear shell surrounding perfectly crystalline material, but rather that a gradual increase in crystallinity occurs from the surface of a particle towards the interior [33]. Nagelschmidt et al. [36] found the same results on quartz graded sands, stating that the intensities in diffraction experiments increased with decreasing size that is partly due to the presence of such amorphous layer. If we consider the same effect on our materials, we can claim the presence of an amorphous layer on both C_3S and C_3A. At the very beginning of the hydration process, C_3S may form a very thin layer of C-S-H that temporally inhibits the dissolution but increasing the diffracted intensity, leading to an “apparent precipitation” of material, evidenced by an increase in the calculated weight fraction. In this period of time, the “apparent precipitation” effect dominates the dissolution process. When the acceleration period of C_3S starts (after 3 hours), the dissolution assumes a greater importance, leading to the decrease in calculated weight fraction, as expected.

A slightly different consideration has to be made for C_3A. In this case the “apparent precipitation” period duration increases at increasing amount of gypsum. So, the amorphous layer may be considered as Ca-Al hydrates but also as AFm phases. Such a theory has been previously advanced by Nonat *et al.* [37–40], who proposed the formation of AFm phases during the initial part of hydration process to explain the decrease of Ca^{2+} concentration in solution, but which had no evidence in x-ray diffraction. Claiming the presence of this amorphous layer shell around C_3A grains, we can confirm this proposed theory. Finally, when all the gypsum is consumed, the dissolution rate of C_3A increases, becoming the dominant effect and leading to the decrease in calculated weight fraction, as expected.

4.5.2 Dissolution/precipitation kinetics calculated from XRD data

Considering the dissolution/precipitation kinetics calculated from x-ray diffraction, we can separate the discussion between two systems: C_3S-gypsum and C_3A-gypsum. During the following discussion, we will refer to different parts of the kinetics specifying the transformations in dissolution/precipitation rate. Such division will be useful also to discuss about isothermal calorimetry data.

In literature the interactions between C_3A and gypsum are well reported and still nowadays this topic is deeply investigated, probably because the reactions that involve C_3A and gypsum lead to the formation of detectable and determinable phases. C_3S-gypsum system does not give the same clear products. The dissolution rate and the time of complete depletion of C_3A are strictly related to the initial amount of gypsum: in fact, from mix 1 to mix 3 we can see how the increase of the dissolution rate of C_3A occurs later in time and only when all the gypsum has been consumed (figure 4.39).

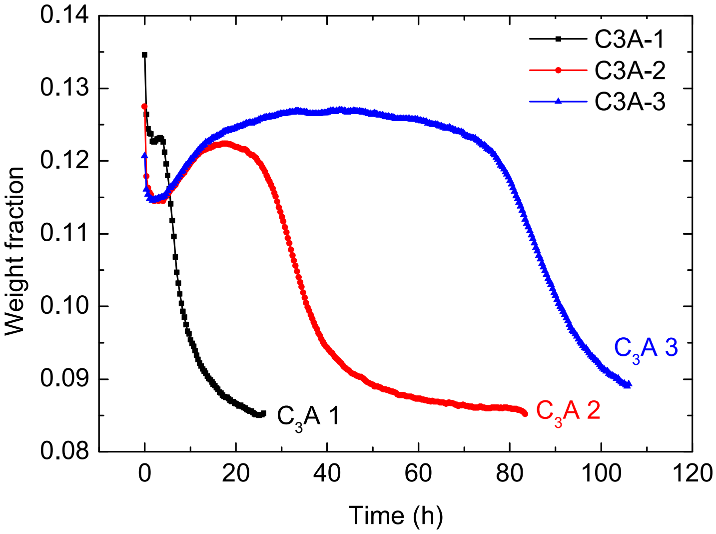

Figure 4.46: comparison of dissolution kinetis of C3A in mix 1 (black squares), mix 2 (red rhombs) and mix 3 (blue triangles).

The dissolution of C_3A and gypsum produces ettringite, which remains the stable phase until a source of sulphate ions is available. It is interesting to note that, especially for mix 2 and 3, ettringite continues to precipitate even when gypsum cannot be detected and it starts to dissolve when the dissolution rate of C_3A decreases.

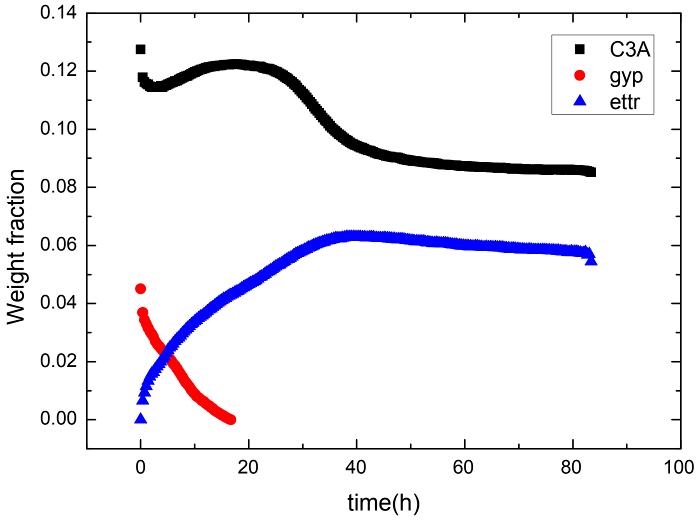

Figure 4.47: correlation between C_3A and gypsum dissolution with ettringite precipitation in mix 3. It has to be noted that the precipitation of ettringite continues after the complete depletion of gypsum, assuming another sulphate source that contributes to the precipitation of ettringite.

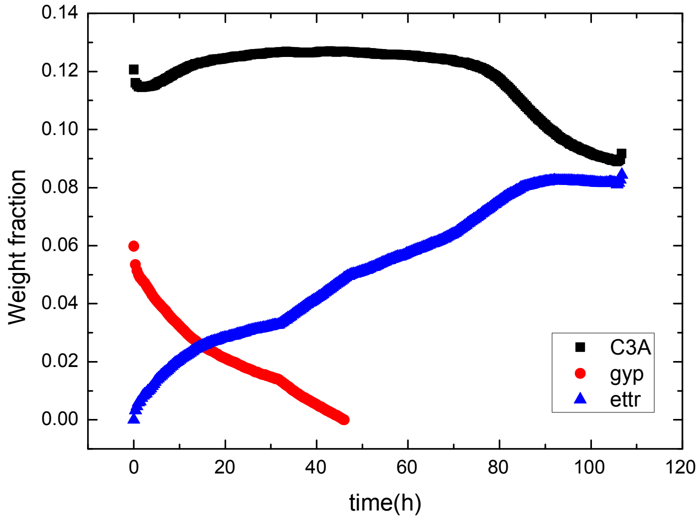

Figure 4.48: correlation between C_3A and gypsum dissolution with ettringite precipitation in mix 3. It has to be noted that the precipitation of ettringite continues after the complete depletion of gypsum, assuming another sulphate source that contributes to the precipitation of ettringite.

A possible explanation to this phenomenon is given in literature: it has been proposed by several authors [41–44] that C-S-H can incorporate $(SO_4)^{2-}$ anions on their structure, acting as a source of sulphates for the precipitation of ettringite even when gypsum is completely depleted. This hypothesis presumes that sulphates ions in C-S-H can be released only when gypsum is totally consumed.

Ettringite starts to dissolve only when any source of $(SO_4)^{2-}$ anions are exhausted; the transformation into a more stable phase is not always clear. In mix 1 and 2 the dissolution of ettringite lead to the formation of hemicarboaluminate while in mix 3 this is not clearly detectable. Such transformation is quite unexpected, because we used the boron-glass capillary sealed with wax in order to avoid any carbonation effect. Actually we properly sealed any sample before measurements but the carbonation still occurs. After the chemical titration of Millipore water, we found that a measurable quantity of CO_2 is dissolved in water, which acts as a source for the precipitation of hemicarboaluminate, thermodynamically stable in our experimental conditions.

Considering C_3S dissolution and the role of gypsum, we can see that gypsum accelerates the beginning of the dissolution process when the gypsum content increases. Although the dissolution process starts almost at the same time (3 hours after the beginning of hydration), mix 1 shows an initial lower rate than mix 2 and 3, which lead to a greater delay in the dissolution of C_3S when the gypsum content is lower (figure 4.42).

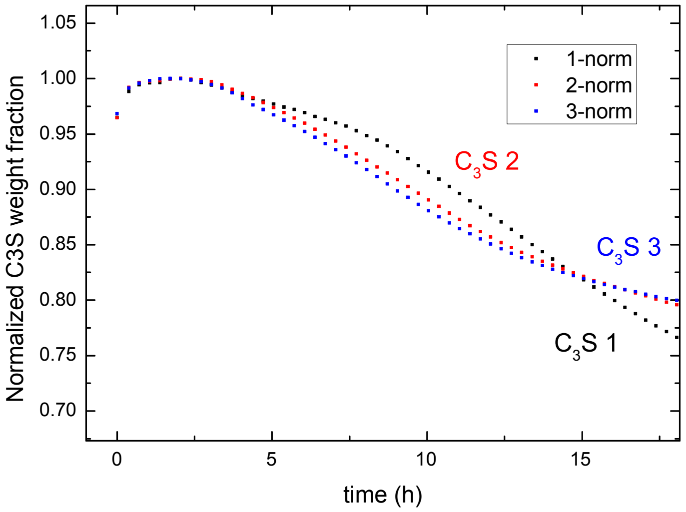

Figure 4.49: zoom within 16 hours of hydration into normalized C3S weight fractions. Black squares: mix 1; red rhombs: mix 2; blue triangles: mix 3.

This means that the same relative dissolution of C_3S (e.g., 10%) occurs after 9.1 hours for mix 3, 9.5 hours for mix 2 and 10.8 hours for mix 1.

Within 26 hours (measuring time of mix 1), also portlandite and C-S-H show precipitation trends strictly related to C_3S dissolution: the same relative precipitation of portlandite (e.g., 40%) occurs after 8.6 hours for mix 3, 9.7 hours for mix 2 and 10.5 hours for mix 1 (figure 4.43).

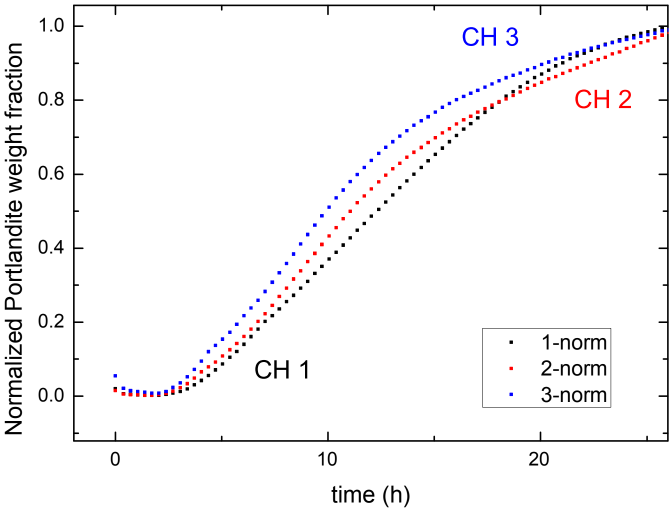

Figure 4.50: zoom within 26 hours of hydration into normalized Portlandite weight fractions. Black squares: mix 1; red rhombs: mix 2; blue triangles: mix 3.

C-S-H precipitation kinetics exhibit slightly different timings but equal trends: within 26 hours, the 40% precipitation occurs at 8.7 hours for mix 3, 9.7 hours for mix 2 and 10.6 hours for mix 1. The base hypothesis for this normalization is that all the precipitated portlandite and C-S-H are produced only by the dissolution of C_3S and no other calcium source (such as gypsum) is responsible for the precipitation of both phases.

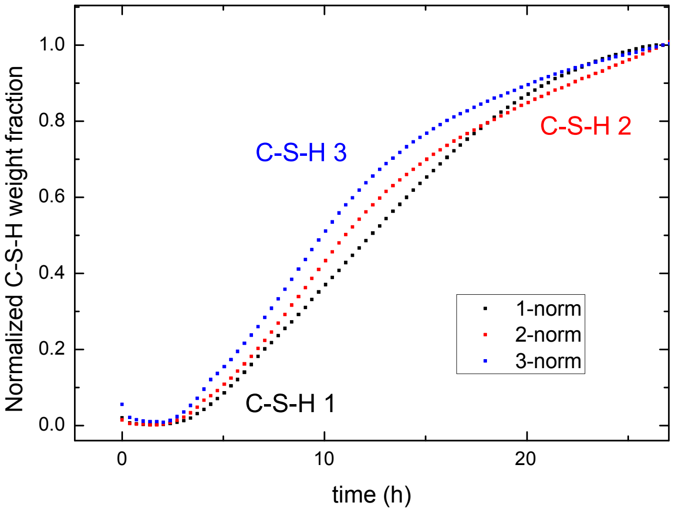

Figure 4.51: zoom within 26 hours of hydration into normalized C-S-H weight fractions. Black squares: mix 1; red rhombs: mix 2; blue triangles: mix 3.

Such behaviour has been partly described before when talking about ettringite precipitation. Gypsum increases the growth rates of C-S-H and its permeability leading to a greater degree of hydration for the same curing time [42]; Mehta et al. [45] found that small amounts of gypsum (3%) added to C_3S accelerates the setting and hardening of alite cements, while bigger amounts (6%) result in strength deterioration. Menetrier et al. [46] report again previous literature experiments, where a certain amount of $(SO_4)^{2-}$ can be incorporated into C-S-H, the main C_3S hydration product. From their experiments, the CaO concentration in solution for C_3S + gypsum system reaches the saturation level considerably before the C_3S hydrated alone: with gypsum, the C_3S dissolution rate increases during the acceleration period. Similar results have been obtained by our group monitoring the hydration of triclinic C_3S-gypsum and Alite-gypsum systems. Both systems show how the hydration of C3S and Alite is accelerated when gypsum is added. Consequently, higher degree of hydration at early ages are reached only when gypsum is present. Since in literature this phenomenon has been described in the past, we can consider it valid also for C_3S – C_3A – Gypsum blends.

4.5.3 Isothermal calorimetry data

The comparison of heat flow data measured at different temperatures returned different results for undersulphated (mix 1) and proper sulphated systems (mix 2 and 3). Mix 1 is undersulphated because the characteristic sharp peak of the aluminate reaction after gypsum depletion occurs before the silicate reaction and this later reaction is delayed and its peak lowered compared to properly sulphated systems. Mix 2 and 3 can be called properly sulphated as the aluminate reaction occurs after the silicate one [47]. The peak due to aluminate reaction is delayed with increasing gypsum content. This aluminate peak becomes also broader and lower as the gypsum content in the cement increases.

At 20°C, mix 1 shows one intense and asymmetric peak; when the calorimeter temperature is increased, this peak increases in intensity and occur earlier, with a small shoulder which occurs after the peak itself. The peak is referred to the increase of the dissolution rate of C_3A while the small shoulder to the maximum dissolution rate reached by C_3S. When the temperature is set at 32°C, an inversion occurs: the small shoulder becomes a definite peak which occurs even before the previously described one. With the peaks crossover we can see how the C_3S dissolution rate increases (higher heat flow value) while the C_3A dissolution rate decreases, both compared to the heat flow measured at 26°C.

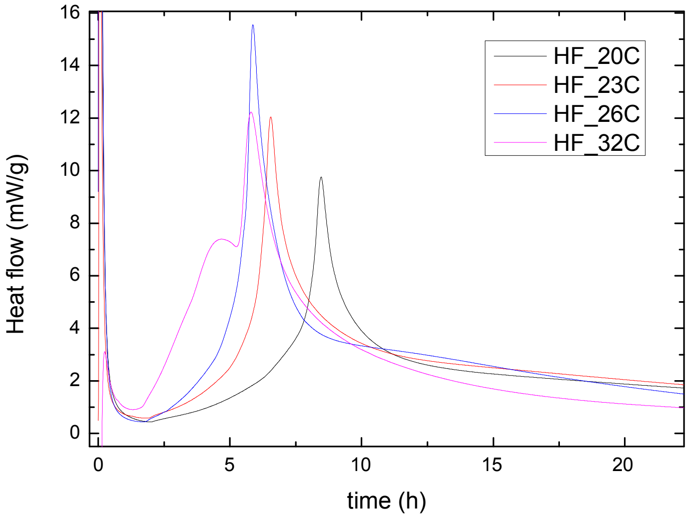

Figure 4.52: measured heat flow of mix 1 hydration at 4 different temperatures: 20°C (black), 23°C (red), 26°C(blue) and 32°C(pink).

A possible explanation is that when the rapid increase of C_3A dissolution rate occurs before that one of C_3S, the Al cations inhibits the dissolution of C_3S [41], causing a lower dissolution rate of C_3S. When temperature increases, reactions become faster (Arrhenius effect) [19] enough to make the increase of dissolution rate of C_3S occurring before the equivalent acceleration in C_3A dissolution rate: the dissolved Al cations are not able to limit C_3S dissolution, which occurs faster. On the other hand, C_3A dissolution rate result slower probably because the limiting factor is a higher Ca^{2+} concentration given by the previous abundant dissolution of C_3S.

Such hypothesis seems to be valid also for mix 2 and 3. In both the proper sulphated systems, we can observe 2 distinct, well separated calorimetric peaks: the first referred to an increase in C_3S dissolution and the second to the increase in C_3A dissolution.

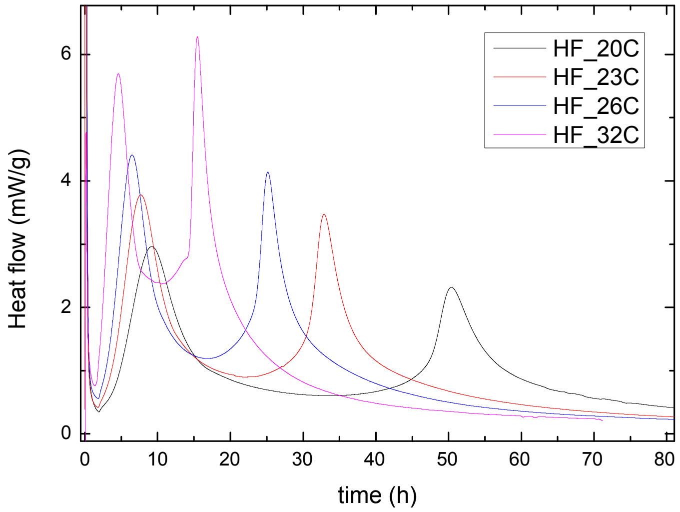

Figure 4.53: measured heat flow at 20°C (black), 23°C (red), 26°C(blue) and 32°C(pink) for mix 2 pastes.

The Arrhenius effect is clearly visible and affects both the dissolution rate of C_3S and C_3A, but no crossover effect can be detected. From 20°C to 32°C we observe a continuous increase in dissolution rates, especially for C_3A which shows a higher dissolution rate than C_3S only at 32°C.

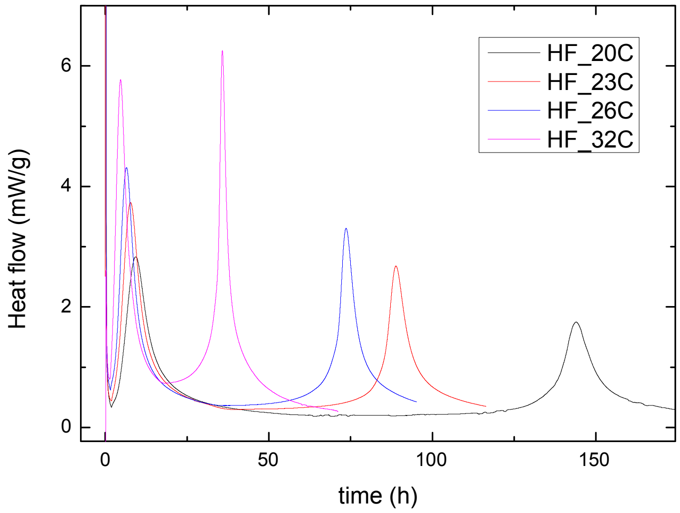

Figure 4.54: measured heat flow generated by mix 3 pastes at 20°C (black), 23°C (red), 26°C(blue) and 32°C(pink).

Finally, a general consideration about the shape of the curve has to be written. In Alexandra Quennoz Ph.D. thesis [10] it is reported a study of Di Murro [48] on mixtures of pure phases (monophase grains) and polyphase grains of alite and C_3A mixed with gypsum. There are significant differences between the hydration of two different nature of grains, especially regarding C_3A. For polyphase grains C_3A dissolution occurs earlier and the calorimetric peak is not well defined; for monophase grains the reaction is slower, the peak occurs later and appears to be well separated and defined. She explains this phenomenon with the difference in phase availability: in polyphase grains, C_3A is better dispersed and present in small amounts in all the cement grains instead of few monophase C_3A grains. Its specific surface is also higher than in monophase systems, leading to a higher reactivity.

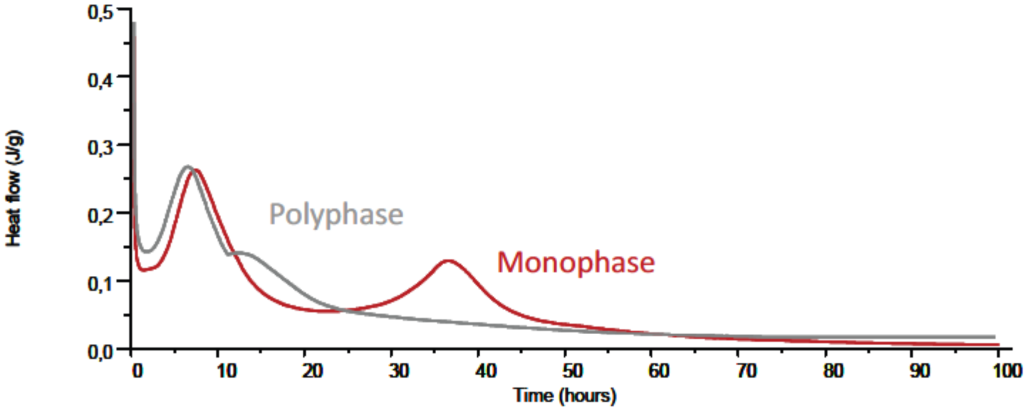

Figure 55: Heat evolution and conductivity curves of monophase and polyphase model cement pastes containing 73% alite – 18% C3A – 9% gypsum [48].

REFERENCES

[1] H. F. W. Taylor, *Cement chemistry*, Second Edi. Thomas Telford, 1997.

[2] B. H. O'Connor and M. D. Raven, "Application of the Rietveld Refinement Procedure in Assaying Powdered Mixtures," *Powder Diffraction*, vol. 3, no. 01, pp. 2–6, Jan. 1988.

[3] N. V. Y. Scarlett and I. C. Madsen, "Quantification of phases with partial or no known crystal structures," *Powder Diffraction*, vol. 21, no. 04, pp. 278–284, 2006.

[4] P. Whitfield and L. Mitchell, "Quantitative Rietveld analysis of the amorphous content in cements and clinkers," *Journal of Materials Science (…*, vol. 8, pp. 4415–4421, 2003.

[5] L. D. Mitchell, J. C. Margeson, and P. S. Whitfield, "Quantitative Rietveld analysis of hydrated cementitious systems," *Powder Diffraction*, vol. 21, no. 2, p. 111, 2006.

[6] A. G. D. La Torre, S. Bruque, and M. A. G. Aranda, "Rietveld quantitative amorphous content analysis research papers," *Journal of Applied Crystallography*, vol. 34, pp. 196–202, 2001.

[7] L. León-Reina, a. G. De la Torre, J. M. Porras-Vázquez, M. Cruz, L. M. Ordonez, X. Alcobé, F. Gispert-Guirado, a. Larrañaga-Varga, M. Paul, T. Fuellmann, R. Schmidt, and M. a. G. Aranda, "Round robin on Rietveld quantitative phase analysis of Portland cements," *Journal of Applied Crystallography*, vol. 42, no. 5, pp. 906–916, Sep. 2009.

[8] L. Valentini, M. C. Dalconi, M. Parisatto, G. Cruciani, and G. Artioli, "Towards three-dimensional quantitative reconstruction of cement microstructure by X-ray diffraction microtomography," *Journal of Applied Crystallography*, vol. 44, no. 2, pp. 272–280, 2011.

[9] J. F. Young and W. Hansen, "Volume relationships for C-S-H formation based on hydration stoichiometries," *Materials Research Society Symposium Proceedings*, vol. 85, pp. 313–322, 1986.

[10] A. Quennoz, "Hydration of C3A with Calcium Sulphate alone and in the presence of Calcium silicate," Ecole Polytechnique Federale de Lousanne, 2011.

[11] V. M. Malhotra and N. J. Carino, *Handbook on Nondestructive Testing of Concrete*. CRC Press, 2004, p. 386.

[12] J. Poole, K. Riding, and K. Folliard, “Methods for calculating activation energy for Portland cement,” *ACI materials …*, no. 104, 2007.

[13] A. Hardison, G. Lewis, A. U. D. Daniels, and R. A. Smith, “Determination of the activation energies of and aggregate rates for exothermic physico-chemical changes in UHMWPE by isothermal heat-conduction microcalorimetry (IHCMC).,” *Biomaterials*, vol. 24, no. 28, pp. 5145–51, Dec. 2003.

[14] R. J. Tank and N. J. Carino, “Rate constant functions for strength development of concrete,” *ACI Materials Journal*, vol. 88, no. 1, pp. 74–83, 1991.

[15] M. Avrami, “Kinetics of Phase Change. I General Theory,” *Journal of Chemical Physics*, vol. 7, p. 1103, 1939.

[16] M. Avrami, “Kinetics of Phase Change. II Transformation-Time Relations for Random Distribution of Nuclei,” *Journal of Chemical Physics*, vol. 8, p. 212, 1940.

[17] M. Avrami, “Granulation, Phase Change, and Microstructure Kinetics of Phase Change. III,” *Journal of Chemical Physics*, vol. 9, p. 177, 1941.

[18] R. Berliner, M. Popovici, K. W. Herwig, M. Berliner, H. M. Jennings, and J. J. Thomas, “Quasielastic Neutron Scattering Study of the Effect of Water-To-Cement Ratio on the Hydration Kinetics of Tricalcium Silicate,” *Cement and Concrete Research*, vol. 28, no. 2, pp. 231–243, 1998.

[19] J. J. Thomas, “A new approach to modeling the nucleation and growth kinetics of tricalcium silicate hydration,” *Journal of American Ceramic Society*, vol. 90, no. 10, pp. 3282–3288, 2007.

[20] A. Damasceni, L. Dei, E. Fratini, F. Ridi, S.-H. Chen, and P. Baglioni, “A Novel Approach Based on Differential Scanning Calorimetry Applied to the Study of Tricalcium Silicate Hydration Kinetics †,” *The Journal of Physical Chemistry B*, vol. 106, no. 44, pp. 11572–11578, Nov. 2002.

[21] D. Jansen, S. T. Bergold, F. Goetz-Neunhoeffer, and J. Neubauer, “The hydration of alite: a time-resolved quantitative X-ray diffraction approach using the G -factor method compared with heat release,” *Journal of Applied Crystallography*, vol. 44, no. 5, pp. 895–901, Aug. 2011.

[22] D. Jansen, F. Goetz-Neunhoeffer, B. Lothenbach, and J. Neubauer, “The early hydration of Ordinary Portland Cement (OPC): An approach comparing measured heat flow with calculated heat flow from QXRD,” *Cement and Concrete Research*, vol. 42, no. 1, pp. 134–138, Jan. 2012.

[23] C. Hesse, F. Goetz-Neunhoeffer, and J. Neubauer, “A new approach in quantitative in-situ XRD of cement pastes: Correlation of heat flow curves with early hydration reactions,” *Cement and Concrete Research*, vol. 41, no. 1, pp. 123–128, Jan. 2011.

[24] K. Van Breugel, “Prediction of Temperature Development in Hardening Concrete,” in *Prevention of Thermal Cracking in Concrete at Early Ages, RILEM Report 15*, E. Spon, Ed. London: , 1998, pp. 51–75.

[25] L. D’Aloia and G. Chanvillard, “Determining the ‘apparent’ activation energy of concrete: Ea—numerical simulations of the heat of hydration of cement,” *Cement and Concrete Research*, vol. 32, pp. 1277–1289, 2002.

[26] H. Kada-Benameur, E. Wirquin, and B. Duthoit, “Determination of apparent activation energy of concrete by isothermal calorimetry,” *Cement and Concrete Research*, vol. 30, no. 2, pp. 301–305, Feb. 2000.

[27] L. E. Copeland, D. L. Kantro, and G. Verbeck, “Part IV-3 Chemistry of Hydration of Portland Cement,” in *4th International Symposium of the Chemistry of Cement*, 1960, pp. 429–465.

[28] G. De Schutter and L. Taerwe, “Degree of Hydration-Based Description of Mechanical Properties of Early-Age Concrete,” *Materials and Structures*, vol. 29, no. 7, pp. 335–344, 1996.

[29] A. Schindler and K. Folliard, “Heat of hydration models for cementitious materials,” *ACI Materials Journal*, no. 102, 2005.

[30] G. W. Brindley, “A Theory of X-ray Absorption in Mixed Powders,” *Philosophy Magazine*, vol. 36, pp. 347–369, 1945.

[31] T. M. Sabine, B. A. Hunter, W. R. Sabine, and C. J. Ball, “Analytical Expressions for the transmission factor and peak shift in absorbing cylindrical specimens,” *Journal of Applied Crystallography*, vol. 31, pp. 47–51, 1998.

[32] J. C. Taylor and C. E. Matulis, “Absorptron Contrast Effects in the Quandtative XRD Analysis of Powders by Full Multiphase Profile Refinement,” *Journal of Applied Crystallography*, vol. 24, pp. 14–17, 1991.

[33] R. Gordon and G. Harris, "Effect of particle-size on the quantitative determination of quartz by X-ray diffraction," *Nature*, vol. 175, p. 1135, 1955.

[34] J. Seo, M. H. Lean, and A. Kole, "Membraneless microseparation by asymmetry in curvilinear laminar flows.," *Journal of chromatography. A*, vol. 1162, no. 2, pp. 126–31, Aug. 2007.

[35] C. Hesse and F. Goetz-Neunhoeffer, "Quantitative in situ X-ray diffraction analysis of early hydration of Portland cement at defined temperatures," ... *Diffraction*, pp. 112–115, 2009.

[36] G. Nagelschmidt, R. L. Gordon, and O. G. Griffin, "Surface of Finely-Ground Silica," *Nature*, vol. 169, no. 4300, pp. 539–540, Mar. 1952.

[37] S. Pourchet, L. Regnaud, J. P. Perez, and A. Nonat, "Early C3A hydration in the presence of different kinds of calcium sulfate," *Cement and Concrete Research*, vol. 39, no. 11, pp. 989–996, 2009.

[38] S. Garrault, H. Minard, and A. Nonat, "Hydration of silicate phase and mechanical evolution in'alite-tricalcium aluminate-gypsum'complex system," *12 th International ...*, 2007.

[39] H. Minard, S. Garrault, L. Regnaud, and A. Nonat, "Mechanisms and parameters controlling the tricalcium aluminate reactivity in the presence of gypsum," *Cement and Concrete ...*, vol. 37, pp. 1418–1426, 2007.

[40] H. Minard, S. Garrault, and A. Nonat, "Understanding of Reactional Sequences and Limiting Stages during Tricalcium Aluminate Hydration with and without Gypsum.," *12 th International ...*, 2007.

[41] A. Quennoz and K. L. Scrivener, "Interactions between alite and C3A-gypsum hydrations in model cements," *Cement and Concrete Research*, vol. 44, pp. 46–54, Feb. 2013.

[42] S. Gunay, S. Garrault, A. Nonat, and P. Termkhajornkit, "Influence of calcium sulphate on hydration and mechanical strength of tricalcium silicate," *Unpublished*, 2012.

[43] X. Pardal, I. Pochard, and A. Nonat, "Experimental study of Si–Al substitution in calcium-silicate-hydrate (C-S-H) prepared under equilibrium conditions," *Cement and Concrete Research*, vol. 39, no. 8, pp. 637–643, Aug. 2009.

[44] Y. Fu, P. Xie, P. Gu, and J. Beaudoin, “Effect of temperature on sulphate adsorption/desorption by tricalcium silicate hydrates,” *Cement and concrete research*, vol. 24, no. 8, pp. 1428–1432, 1994.

[45] P. Mehta, D. Pirtz, and M. Polivka, “Properties of alite cements,” *Cement and concrete research*, pp. 439–450, 1979.

[46] D. Menetrier, I. Jawed, and J. Skalny, “Effect of gypsum on C 3 S hydration,” *Cement and Concrete Research*, vol. I, no. c, pp. 697–701, 1980.

[47] N. Tenoutasse, “The Hydration Mechanism of C3A and C3S in the Presence of Calcium Chloride and Calcium Sulphate,” 1969, pp. 372–378.

[48] H. Di Murro, “Mécanismes d’élaboration de la microstructure des bétons,” Université de Bourgogne, 2007.

5. Conclusions

The main topic of this Ph.D. thesis was to investigate the kinetics of simplified cement systems, composed only by C_3S, C_3A and gypsum, mostly by means of *in-situ* x-ray powder diffraction experiments. The choice to use a set of model cements is to have a deeper insight into the kinetics at early age of the most abundant and most important phases of a Portland cement. It has emerged the opportunity to investigate the model cements also by means of isothermal calorimetry, which is more suitable to obtain reliable kinetic data.

We have seen how *in-situ* x-ray diffraction with a laboratory instrument is a useful technique to investigate cement kinetics, although the first 20 minutes of hydration cannot be monitored (due to the *ex-situ* sample preparation). The boron-glass capillary as sample holder confirmed that the sample does not suffer water bleeding and carbonation; furthermore, the focussing transmission geometry and the small size capillary (0.3mm) permit to avoid absorption problems. On the other hand, to obtain reliable kinetics, we had to reduce the acquisition time, which coupled with the use of 0.3mm capillary and a low amount of investigated material produced very noisy measurements.

As explained in the appendix chapter, we performed also some measurements in Bragg-Brentano geometry that force the use of a Kapton film to prevent carbonation. The measurement in Bragg-Brentano geometry permits to avoid any absorption problem and to investigate a more homogeneous amount of material. Unfortunately, the water bleeding effect cannot be avoided, because the Kapton film revealed to be not perfectly insulating. Also the chemical shrinkage cannot be avoided and the result is a left shift of diffraction peaks, which is more difficult to treat when a parametric refinement (as what we do to obtain kinetics) is performed.

C_3S kinetics has been observed to be very similar from mix 1 to mix 3: the dissolution trends are very close in shape and time. Such trends seems to be slightly accelerated when gypsum is added to the system. This suggest an active contribution of gypsum to the dissolution rate of C_3S.

On the other hand, C_3A is greatly influenced by the quantity of gypsum: the more gypsum quantity, the more delayed C_3A increase in dissolution rate.

It is proposed the presence of an amorphous layer that partially inhibits the dissolution of C_3A as long as gypsum is still present as solid phase and which is claimed to be responsible of the "apparent precipitation effect" observed especially in C_3A kinetics.

Isothermal calorimetry measurements revealed the presence of two distinct peaks, one related to the increase in C_3S dissolution rate and the other one related to the increase in C_3A dissolution rate. The presence of these 2 distinct peaks is particularly different from an OPC heat flow chart, where a wide and broad peak is usually detected as a result of the convolution of C_3S dissolution heat (mostly) and C_3A dissolution heat. Such feature can be explained with the monophase nature of the grains that results in a greater specific surface, especially for C_3A, in our model cements, while an OPC is constituted by polyphase clinker grains that conduct to a main hydration peak.

The increase in reaction temperature inside of the calorimeter drives to an increase in reaction rates, as seen from the left shift of calorimetric peaks (earlier occurrence) of heat flow plots. Peaks are very sharp and intense and this could be explained with the synthetic nature of the materials. In a lab synthesis, materials are usually finer than that produced in an industrial plant, leading to an higher specific surface that is responsible for more sharp and intense calorimetric peaks.

From calorimetric data it is not possible to appreciate the influence of gypsum on C_3S hydration rate, as revealed by x-ray diffraction. It is much more evident the delay, within the 3 blends, in the second calorimetric peak due to the total depletion of gypsum.

It has emerged that C_3S dissolution and C_3A dissolution are not independent processes. In particular, gypsum seems to interacts with both of them, accelerating the C_3S dissolution and decelerating C_3A dissolution. In mix 1 (undersulphated system) the first part of the hydration is dominated by C_3A dissolution but the second part is controlled mainly by C_3S dissolution. First/second part can be identified with the occurrence of the first/second calorimetric peak, respectively. As a consequence, in mix 1 there is not a clear distinction within 2 peaks but an intimate bind between C_3A and C_3S dissolution processes. In mix 2 and 3 (properly sulphated systems) the first part is dominated by C_3S dissolution while the second part is mostly controlled by C_3A dissolution. This can be recognized by plotting α_{SF} and α_{IC}vs. time: the first part of the hydration process is controlled only by the dissolution of the first phase while the second α_{SF} has to be shifted upwards to obtain a sufficient fit with α_{IC}. Such shift is the continuous contribution of the first phase to the total degree of hydration and can be considered as a proof that C_3S and C_3A dissolutions are not independent processes.

The analysis of the kinetics revealed controversial results for activation energies calculated using different approaches. The Avrami nucleation and growth model has been useful to describe the acceleration periods of both C_3S and C_3A. The calculated M values are in agreement with the possible nucleation, growth and shape of C-S-H (from C_3S dissolution), AFm and C-A-H (from C_3A dissolution).

Unfortunately, the modelling part of the project has not been developed sufficiently. On one hand, it was possible to model the early hydration of C_3S-gypsum systems, with results confirmed by experimental data (x-ray diffraction, calorimetry, mechanical strength measurements). On the other hand, modelling revealed several issues when focussed on C_3A-gypsum, especially in treating the right dimensions of particles and thermodynamic parameters of gypsum, probably because the interactions between C_3A and gypsum are much more complex and difficult to describe than C_3S-gypsum. For these reasons, the modelling of C_3A-gypsum hydration has to be improved before starting the more complex C_3S-C_3A-gypsum systems.

6. Appendix

The purpose of this chapter is to include selected Ph.D. experimental activities performed that cannot be included in the dissertation of the main project.
Such activities were important to improve laboratory and data analysis skills and for these reasons can be included in an appendix chapter.

Bragg-Brentano measurements on Portland cement pastes

In addition to transmission capillary measurements, we have performed also transmission flat-stage and Bragg-Brentano reflection measurements. Flat-stage transmission geometry is very useful when the available amount of material is low, but it becomes unsuited for kinetic studies because of the water bleeding. In fact, the 2 Kapton foils that squeeze the material within are not able to seal the sample, causing the water bleeding effect and forcing the hydration stop.
Bragg-Brentano measurements can be considered much more suitable for kinetics detection because of the proper amount of investigated material and more homogeneous samples. Unfortunately, Kapton is not a perfect sealing cap and this can cause water bleeding and sample segregation effects. Moreover, when the chemical shrinkage occurs, a strong sample displacement effect can be detected. In figure 1 it can be seen that such sample displacement affects the sample from the very first measurements. Finally, Kapton is not completely x-ray transparent, contributing with some diffraction peaks between 12° and 27° 2θ at CuK$\alpha_{1,2}$ and interfering with the detection of sample diffraction lines in that region (figure 2).

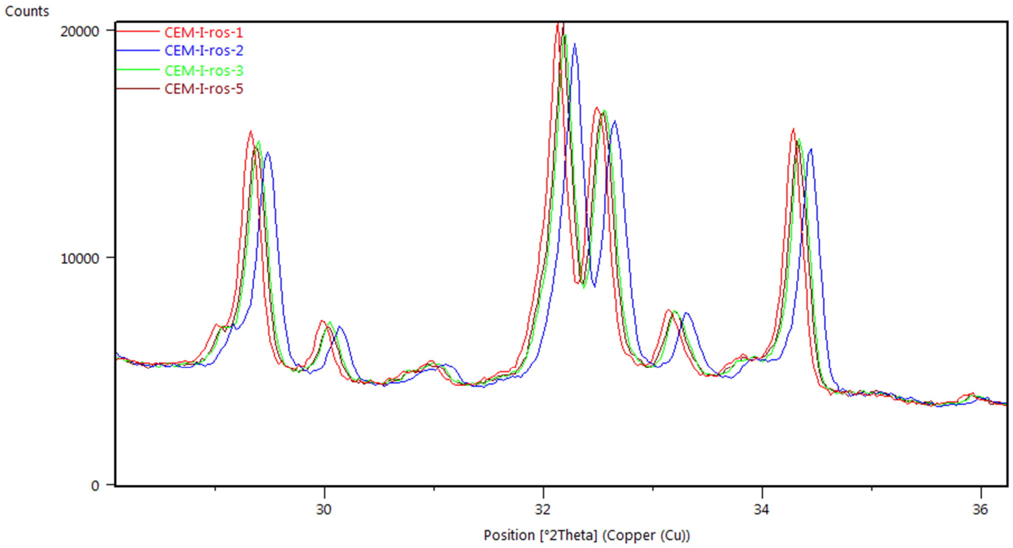

Figure A.56: sample displacement effect occuring from the very first measurements. 2θ range: 28°-36°. 1 is referred to the first measure, 5 to the fifth.

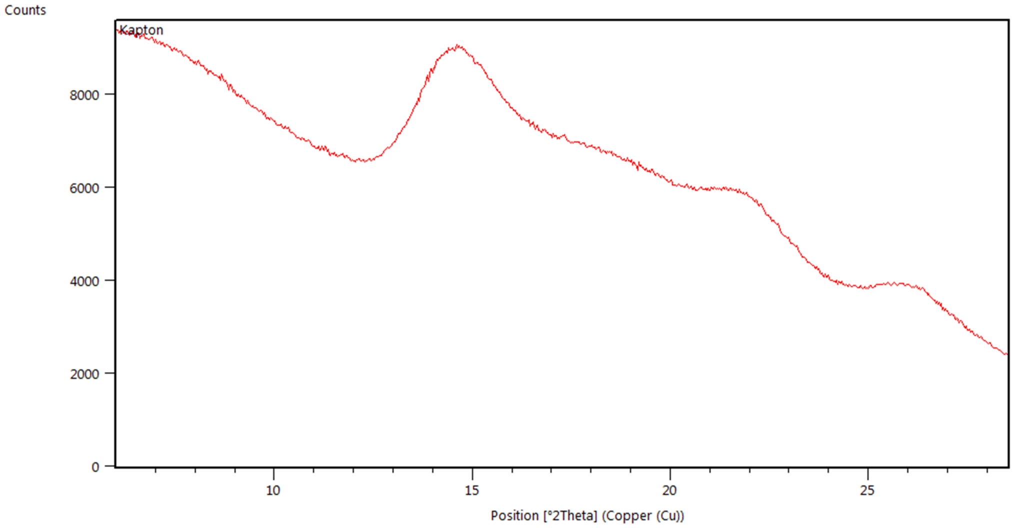

Figure A.57: Kapton contribution to the measured background. At least 3 broad peaks can be recognized between 12° and 27° 2θ, CuK$\alpha_{1,2}$.

The choice to use the focussing transmission capillary geometry was taken because it guarantees the accessibility of low 2θ angles (between 1° and 3°), no segregation effects and no preferred orientations.

Loss of reactivity on C_3S-C_3A-Gy systems

During these 3 years, we noted that our C_3S-C_3A-Gy blends were behaving in different ways every time we measured them, although the materials have been sealed in vacuum conditions. In particular, the occurrence time of C_3A acceleration period was measured to be more delayed at any experiment, both for XRD and isothermal calorimetry. This means that C_3A suffered a sort of reactivity loss.

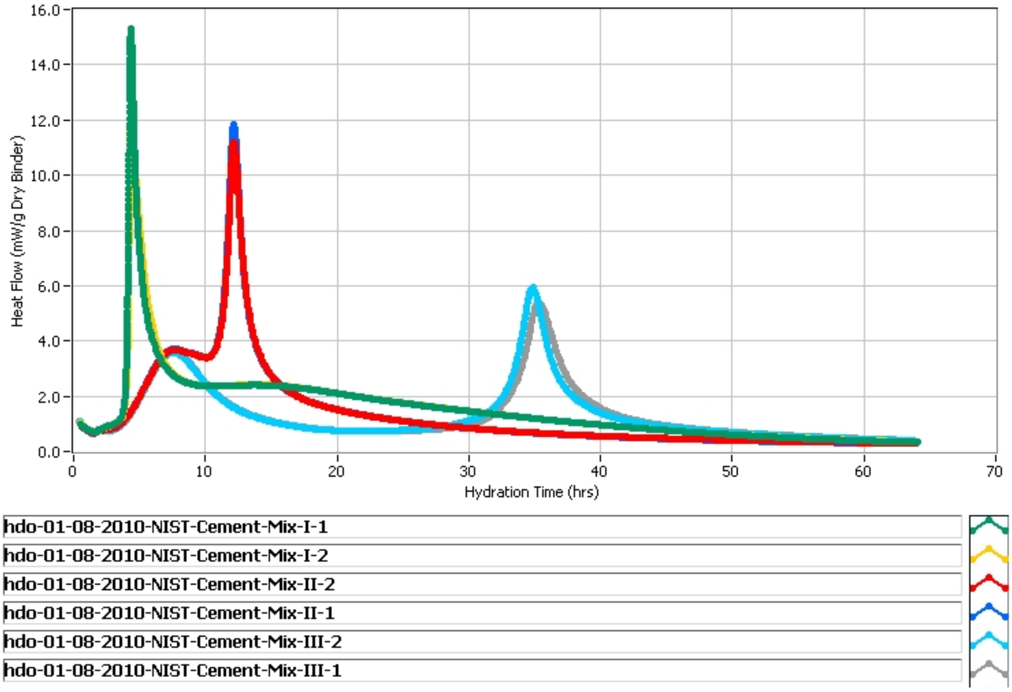

Figure A.58: isothermal calorimetry on the 3 C_3S-C_3A-Gy mix performed on January, 2010. It is important to focus on mix 2 (see next figure).

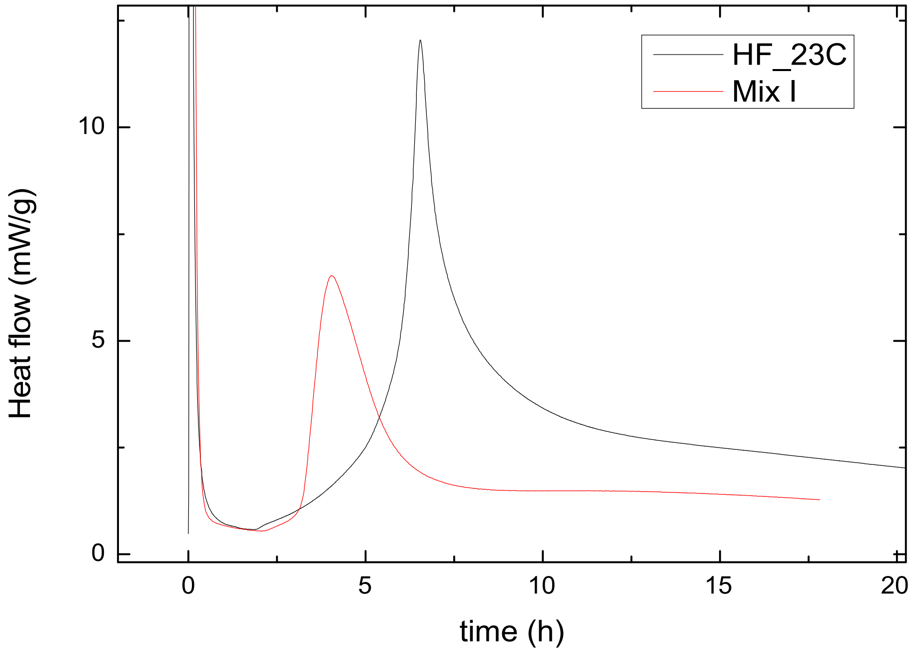

Figure A.59: isothermal calorimetry on mix 1 performed at Dijon on February, 2011 (red) and at Mapei on October, 2011 (black).

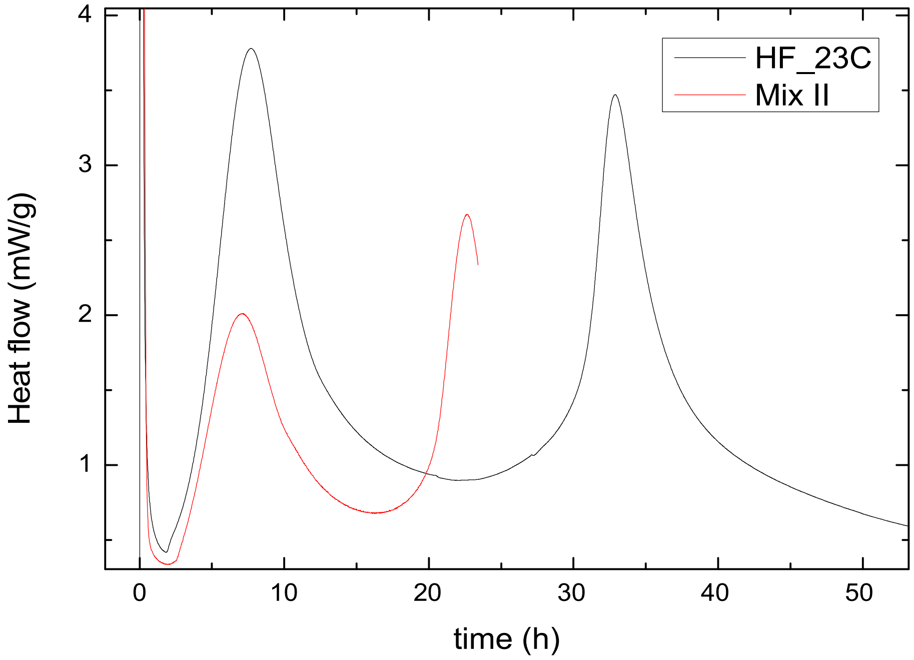

Figure A.60: isothermal calorimetry on mix 2 performed at Dijon on February, 2011 (red) and at Mapei on October, 2011 (black).

Comparing figures A.3, A.4 and A.5 some remarkable notes can be underlined. First of all, a general decrease in heat flow intensity with passing time can be detected mostly for C_3A peak. Secondly, a progressive delay in the occurrence time of calorimetric peaks is revealed. In mix 1 C_3A calorimetric peak occurs after 5 hours in Jan, 2010, after 4 hours in Feb, 2011 and after 6.5 hours in Oct, 2011. In mix 2 C_3S calorimetric peak results slightly delayed whereas the such delay can be clearly for C_3A: 13 hours in 2010, 23 hours in Feb, 2011 and 33 hours in Oct, 2011.

Assuming that gypsum may have a crucial role in this phenomenon, we supposed that C_3A grains should have a reaction rim that could be detected by the scanning electron microscope. To be sure to detect properly the phase, x-ray microanalysis has been performed on each grain.

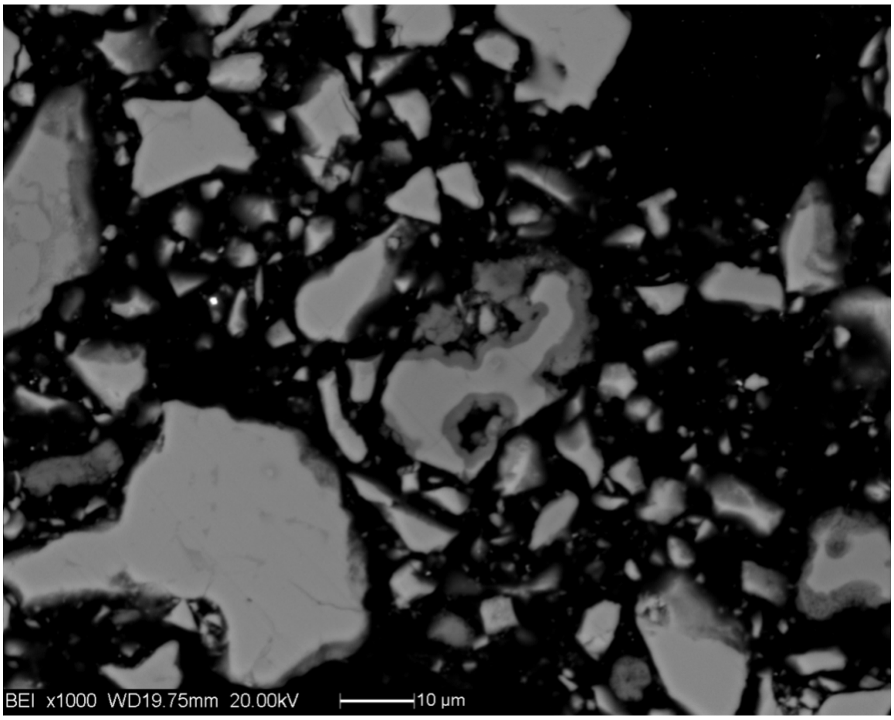

Figure A.61: C_3A grain (centre, light gray) surrounded by a reaction rim (dark gray),with a lower density in respect to C_3A.

C_3A grain in the middle of figure A.6 presents an uneven reaction rim characterized by a lower grey value in respect to C_3A grey value. Qualitative speaking, this can be described as a difference in phase density: the lower the grey value, the lower the material density. If this reaction rim is truly formed by AFm phases, this is in agreement with initial hypothesis. The reaction rim works as physical barrier, limiting C_3A reactivity as long as it remains stable during hydration.

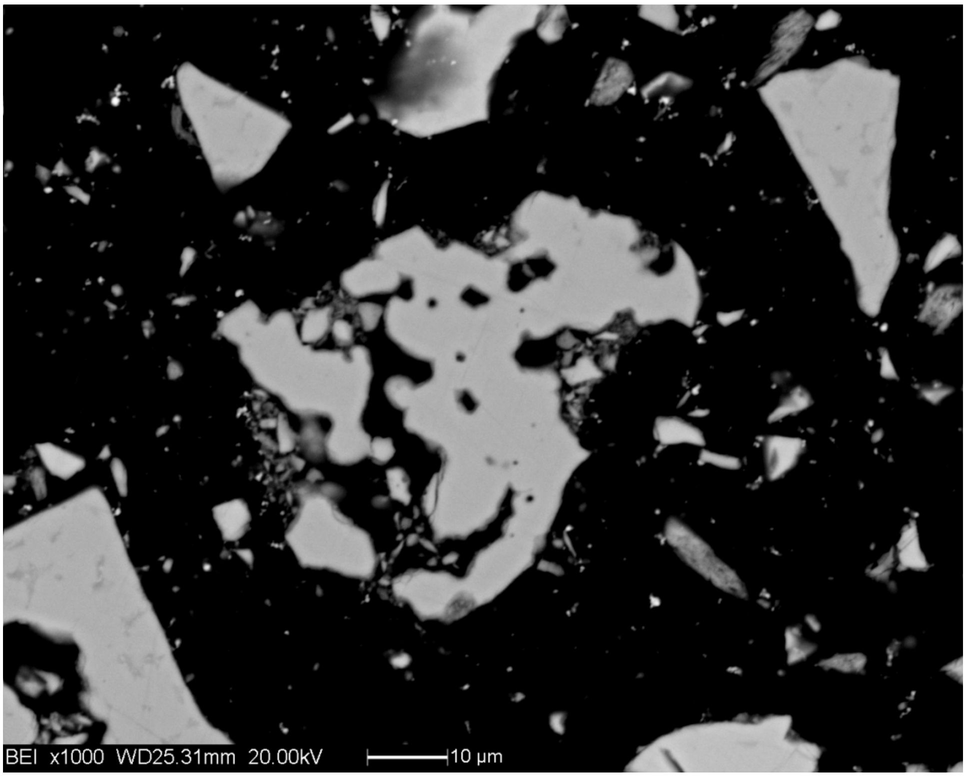

Figure A.62: partially reacted C_3A grain (centre).

Even when a clear rim is not visible, C_3A grains which suffer of low reactivity show buttered holes and dull grain boundaries (figure A.7). Such evidences give an idea on material decay during time, influencing its reactivity and, by a consequence, reaction kinetics.

Even C_3S shows a sort of reaction products that are grown on the grain surface, instead of the boundary (figure A.8).

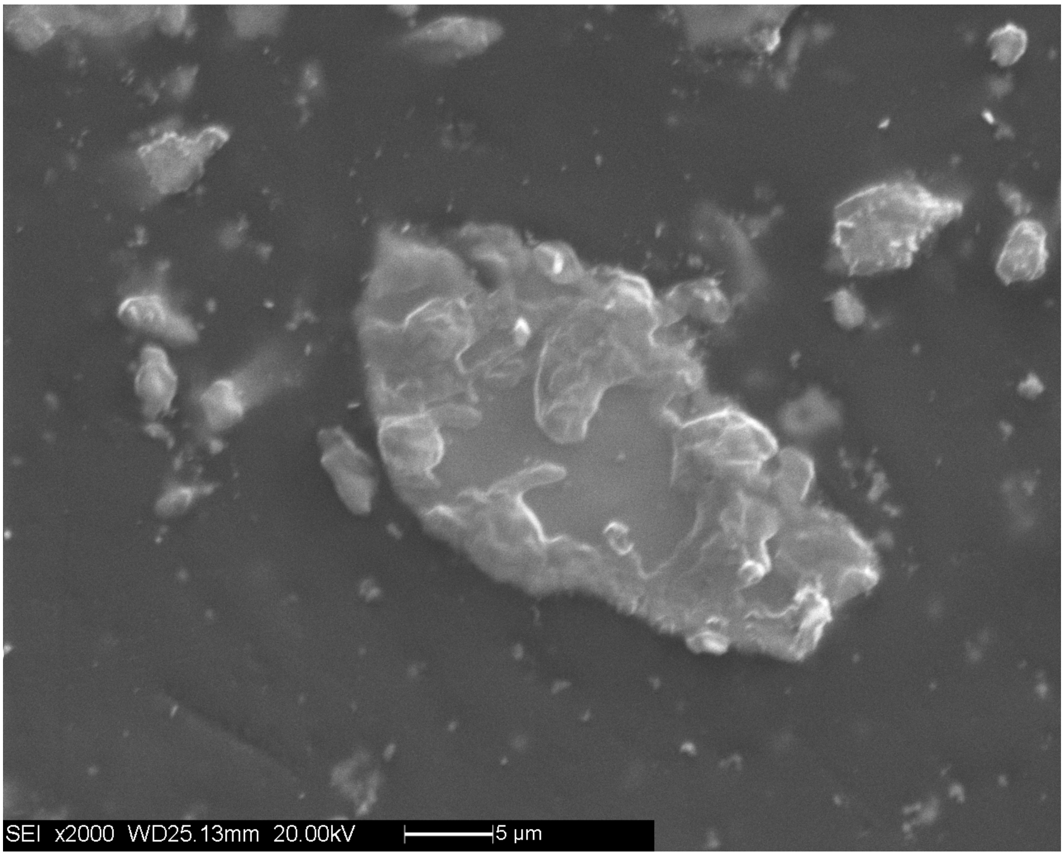

Figure A.63: C_3S grain showing a partly reacted surface and its reaction product. Microanalysis showed only the presence of CaKα and SiKα.

One possible explanation is that partial gypsum decomposition occurs, causing the formation of hydration products and the already claimed loss of reactivity. Another plausible justification is that the vacuum sealing was not sufficient to avoid the formation of these hydration products.

In any case, the loss of reactivity was a difficult issue to consider because it was practically unpredictable. Since the materials decay cannot be avoided, XRD and isothermal calorimetry measurements have to be performed simultaneously to obtain reliable and comparable data.

Synthesis of hemicarboaluminate: an attempt to solve the crystal structure

Hemicarboaluminate, $Ca_4Al_2(CO_3)_{0.5}(OH)_{13}\cdot5.5H_2O$, is one of the AFm phases [1, 2] that can precipitate once the sample is exposed to air or to water containing dissolved CO_2, when $CaCO_3$ is present in a cement. It is a metastable phase that precipitates when the increase in dissolution rate of C_3A occurs. The corresponding stable phase is monocarboaluminate, $Ca_4Al_2(CO_3)(OH)_{12}\cdot5H_2O$, which occurs only at later hydration ages [1]. For these reasons, it is a common product in cements pastes.

Despite of its occurrence, it was only known to have a layered structure, such as other AFm, but the structure was unsolved. The aim of this work was to perform a crystal structure solution on a powder sample using a laboratory instrument.

First of all, pure hemicarboaluminate is necessary to perform a crystal structure solution. We synthetized the material starting from a paper of Balonis and Glasser [3]: C_3A, $CaCO_3$ and CaO have been mixed in stoichiometric proportions with Millipore water at room temperature, water to solid ratio equal to 10 and continuously stirred in a glass flask for 14 days before filtration. The chemical reaction that set hemicarboaluminate precipitation is:

$$4C_3A + 2CaCO_3 + 2CaO + 48H_2O \rightarrow 4Ca_4Al_2(CO_3)_{0.5}(OH)_{13}\cdot5.5H_2O \qquad (A.1)$$

Laboratory C_3A was supplied by Sorrentino, $CaCO_3$ by Sigma-Aldrich and CaO was obtained after calcination of $CaCO_3$ for 1 hour at 100°C. CaO quality and crystallinity were checked by means of XRD.

After 14 days the precipitated solute has been filtered by centrifugation and measured by x-ray powder diffraction, in focussing transmission geometry, using a 0.5mm boron-glass capillary as sample holder. The angular range chosen was 5°-80°, angular step 0.026° and 150s of counting time per step. The result is described in figure A.9. The pattern is characterized by two sharp, very intense

(>40000 counts) diffraction peaks while all the others result broader and smaller (<4000 counts). Qualitative phase analysis detected hemicarboaluminate (ICDD 41-221) and Portlandite (ICDD 44-1481).

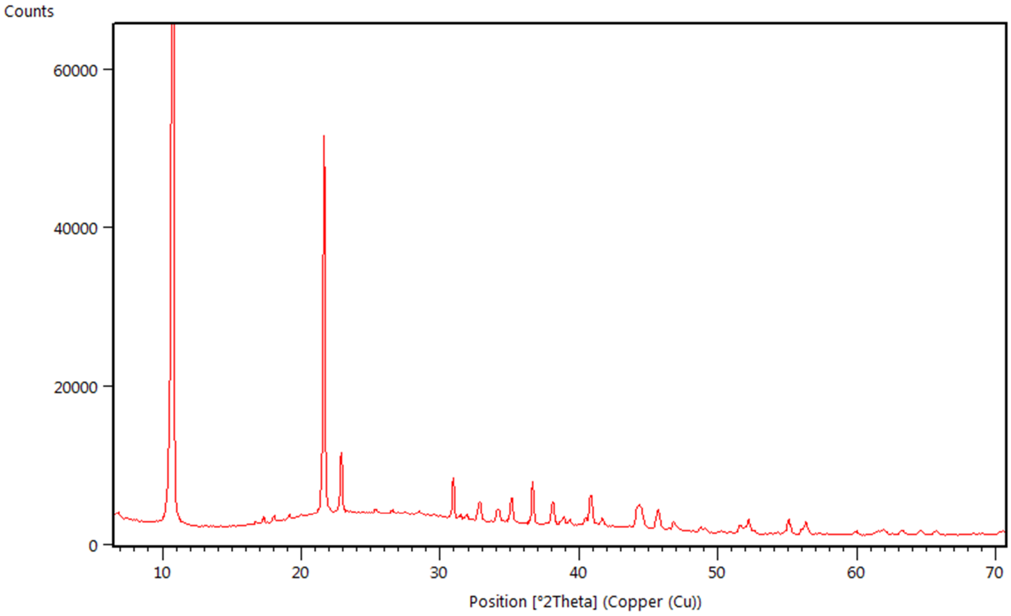

Figure A.64: diffraction pattern of synthetic hemicarboaluminate. Zoom into 7°-70° 2th range.

Considering the number of detected phase, the synthesis product can be suitable to perform a crystal structure solution. From a crystallographic point of view, the measured pattern showed that the starting material seems to be not so appropriate to achieve a crystal structure solution.

A preliminary attempt determined the presence of a layered structure, as for other AFm phases, but the work has to be improved to reach a good stability on the solution.

When this structure solution attempt started, the first hemicarboaluminate structure has been published by Runčevski et. al [4]. They measured a synthetic hemicarboaluminate in a synchrotron radiation facility, which is the solution to have an high signal to noise ratio. It becomes evident that such crystal structure will be a significant starting point to solve the structure of our synthetic material.

Selective dissolution: a powerful technique to characterize cement phases

Selective dissolution is a peculiar technique that permits to concentrate a preferred phase (or group of phases) eliminating the unwanted ones from a powder by dissolving them in an acid or basic solution.

Coupled with x-ray powder diffraction, it permits to quantify ratios between certain phases better than the analysis on the whole clinker.

Two different solutions are considered to dissolve aluminates and silicates. KOH/sugar solution is used to dissolve aluminates and sulphates, giving a residue of silicates and minor phases (e.g. Periclase). Salicylic Acid/ Methanol (SAM) solution is alternatively took to extract the interstitial, sulphate and minor phases, dissolving silicates and free lime present in a clinker. We followed the schematic procedure described by Stutzman [5], preparing the two solutions before proceeding to the selective dissolution.

We chose a CEM I 52.5R (Rossi) to perform the selective dissolution procedure.

Qualitative phase analysis showed the presence of C_3S, C_2S, MgO and $CaCO_3$ after KOH/sugar extraction. C_3A, C_4AF, Bassanite, Gypsum, Arkanite, Syngenite, MgO, Calcite and Portlandite have been detected after SAM extraction. The presence of Portlandite could be interpreted as a product of unreacted free lime when mixed with methanol.

Quantitative phase analysis through Rietveld refinement has been performed in order to obtain an accurate quantification of phases ratios (i.e. C_3S/C_2S) and also to optimize the crystal lattice parameters.

QPA on extracted powder	KOH/sugar extraction	SAM extraction
C_3S	64.12	
C_2S	24.02	
C_3A		29.60
C_4AF		23.50
$CaCO_3$	9.22	15.16
Gypsum		1.82
Bassanite		14.59
Syngenite		5.64
Arcanite		3.32
Periclase	2.43	5.18
Portlandite	0.21	1.19

Table A.9: QPA on extracted powders, after selective dissolution.

QPA on cement	Pre lattice parameters optimiz.	Post lattice parameters optimiz.
C_3S	59.11	57.96
C_2S	17.50	18.05
C_3A	6.90	6.52
C_4AF	4.42	5.36
$CaCO_3$	3.56	3.78
Gypsum	0.88	0.96
Bassanite	2.55	3.24
Syngenite	1.24	1.02
Arcanite	1.36	1.18
Periclase	1.72	1.34
Portlandite	0.75	0.58

Table A.10: QPA on CEM I 52.5R comparing pre lattice parameters optimization (before selective dissolution procedure) and post lattice parameters optimization (after selective dissolution procedure).

	KOH/sugar	SAM	Pre optimiz. (cem)	Post optimiz. (cem)
C_3S/C_2S	2.67		3.38	3.21
C_3A/C_4AF		1.26	1.56	1.22
All sulphates			6.03	6.40
Accessories			6.03	5.70

Table A.11: comparison between different ratios and sums.

From table A.3 we can assume a lower C_3S/C_2S ratio when extraction is performed, compared to C_3S/C_2S ratio calculated from a standard QPA on the cement: the difference is about 17%. This can be due to a better estimation of C_2S when KOH/sugar extraction is carried out. C_3A/C_4AF ratio calculated after SAM extraction is very similar to that calculated after phase parameters optimization on cement QPA. This is not true when considering the pre-optimization: the difference is about 20%.

In order to be sure about the presence of calcite, portlandite and sulphates, we performed TGA (coupled with D-TGA) and DTA.

TGA analysis showed three endothermic events, related to water consumption of hydrous sulphates (~200°C), OH^- consumption from portlandite (450-550°C) and CO_2 release from calcite (650-830°C). Quantitative analysis returned 4.81% of hydrous sulphates, 0.22% of portlandite and 3.55% of calcite. These values are not so distant from Rietveld calculations, especially referring to calcite, while the hydrous sulphates calculation can be considered an appropriate estimation.

DTA showed three endothermic events, referred to water consumption described above. At 720°C and 980°C we detected also two main exothermic events, probably related to two phase transitions: the first involving $\beta\text{-}C_2S \rightarrow \alpha\text{-}C_2S$ and the second involving $M_1C_3S \rightarrow M_2C_3S$.

Characterization of selected phases for internal and external standard methods in Rietveld quantitative phase analysis

An internal or external standard in quantitative phase analysis results really useful to determine the exact content of all the other phases present in the investigated mixture.

When a weighted amount of a standard phase is added to a mixture, the quantitative phase analysis can be scaled to the amount of standard, revealing the presence of unknown or amorphous phases. This is, practically, what the internal standard method requires to have a reliable quantification of all the phases of a sample [6, 7]. In cement science, it is a matter of debate which should be the most appropriate standard to quantify the unknown phases: Al_2O_3 [8–10] and TiO_2 [11] seems to work both properly. Al_2O_3 produced by NIST (National Institute of Standards and Technology) is the leading standard for quantitative phase analysis but its linear absorption coefficient (127 cm^{-1}) is pretty different from the related cement phases coefficients (C_3S=323cm^{-1}, C_3A=274cm^{-1}, [11]). Such difference causes microabsorption problems that are difficult to correct. On the other hand, TiO_2 and most absorbing phases of a clinker have comparable linear absorption coefficients but different particle size distributions (TiO_2=0.4 μm, clinker phases=23-27μm) that can induce a non-uniform distribution of particles in the sample.

It is also possible to determine the amount of all the crystalline phases by using the external standard method developed by O'Connor and Raven [12] and more recently used by Jansen et al. [13]. The external standard depends only by the instrument settings (tube intensity, divergence slits, Soller slits, beam masks, monochromators): for this reason it has to be calculated periodically (e.g., tube ageing causing intensity loss) and each time the instrumental setting is changed. It is related to the quantification of a phase as expressed in equation A.2:

$$W_{\alpha} = \frac{S_{\alpha}(ZMV)_{\alpha}\mu_m^*}{K} \qquad (A.2)$$

Where W_{α} is the calculated weight fraction of phase α, S_{α} is the Rietveld scale factor of phase α, $(ZMV)_{\alpha}$ are the number of formula units in the unit cell, the mass and the volume of unit cell of phase α, μ_m^* is the linear absorption coefficient of the mixture and K is the external standard. With this method, it is possible to obtain the amount of each crystalline phase and, by difference, the amount of the whole unknown/amorphous content of a sample.

Before using the internal or external standard method for our purposes, we wanted to verify the reliability of the methods by producing a set of mixed and weighted standards, which are generally useful also to characterize the materials.

For these purposes, we used Dupont Ti-Pure® R900 TiO2 for internal standard method, quartz and Boron Carbide (BC, high availability in our laboratory) for external standard method. The original choice of boron carbide is also due to the request of using a low absorbing phase “to simulate” Si NIST that has been chosen by Jansen [13]. At this point it becomes useful to distinct the characterization of TiO_2 for internal standard and Al_2O_3 and boron carbide for external standard.

Internal standard

We prepared 2 samples composed by a mix of 50:50 and 75:25 of TiO_2 and ZnO (used as reference), both measured in Bragg-Brentano reflection geometry, within 23° and 120° of angular range, step size 0.017° counting 60s per step.

Results are controversial: in the 50:50 sample, the amount of amorphous material detected was 0.7%-0.9% while in the 75:25 sample the calculation returned negative amorphous content.

The same blends were also measured in focusing capillary geometry, using a 0.3mm and a 0.1mm capillary, with the same instrumental parameters as in Bragg-Brentano. Results here are much more controversial than in Bragg-Brentano, because of unsolvable microabsorption problems.

External standard method

We measured 2 different blends: Al_2O_3-BC and Al_2O_3-SiO_2, with Al_2O_3 used as reference. Al_2O_3-BC samples have been measured in reflection and transmission geometry while Al_2O_3-SiO_2 blends have been measured only in reflection geometry.

Unfortunately, in both cases the difference between the weighted amount of materials and the quantitative phase analysis derived from external standard calculation is too wide to consider the method reliable. Considering that these samples are very simple, the method cannot be extended to a cement system.

REFERENCES

[1] T. Matschei, B. Lothenbach, and F. Glasser, “The AFm phase in Portland cement,” *Cement and Concrete Research*, vol. 37, no. 2, pp. 118–130, Feb. 2007.

[2] T. Matschei, B. Lothenbach, and F. P. Glasser, “The role of calcium carbonate in cement hydration,” *Cement and Concrete Research*, vol. 37, no. 4, pp. 551–558, Apr. 2007.

[3] M. Balonis and F. P. Glasser, “The density of cement phases,” *Cement and Concrete Research*, vol. 39, no. 9, pp. 733–739, Sep. 2009.

[4] T. Runčevski, R. E. Dinnebier, O. V Magdysyuk, and H. Pöllmann, “Crystal structures of calcium hemicarboaluminate and carbonated calcium hemicarboaluminate from synchrotron powder diffraction data.,” *Acta crystallographica. Section B, Structural science*, vol. 68, no. Pt 5, pp. 493–500, Oct. 2012.

[5] P. Stutzman, *Guide for X-ray powder diffraction analysis of Portland cement and clinker*. 1996.

[6] R. E. Dinnebier and S. J. L. Billinge, *Powder Diffraction Theory and Practice*. 2008.

[7] T. Westphal, T. Füllmann, and H. Pöllmann, “Rietveld quantification of amorphous portions with an internal standard—Mathematical consequences of the experimental approach,” *Powder Diffraction*, vol. 24, no. 03, pp. 239–243, Feb. 2012.

[8] L. León-Reina, a. G. De la Torre, J. M. Porras-Vázquez, M. Cruz, L. M. Ordonez, X. Alcobé, F. Gispert-Guirado, a. Larrañaga-Varga, M. Paul, T. Fuellmann, R. Schmidt, and M. a. G. Aranda, “Round robin on Rietveld quantitative phase analysis of Portland cements,” *Journal of Applied Crystallography*, vol. 42, no. 5, pp. 906–916, Sep. 2009.

[9] A. G. D. La Torre, S. Bruque, and M. A. G. Aranda, “Rietveld quantitative amorphous content analysis research papers,” *Journal of Applied Crystallography*, vol. 34, pp. 196–202, 2001.

[10] a G. de la Torre, A. Cabeza, A. Calvente, S. Bruque, and M. a Aranda, “Full phase analysis of Portland clinker by penetrating synchrotron powder diffraction,” *Analytical chemistry*, vol. 73, no. 2, pp. 151–6, 2001.

[11] P. Whitfield and L. Mitchell, “Quantitative Rietveld analysis of the amorphous content in cements and clinkers,” *Journal of Materials Science*, vol. 8, pp. 4415–4421, 2003.

[12] B. H. O’Connor and M. D. Raven, “Application of the Rietveld Refinement Procedure in Assaying Powdered Mixtures,” *Powder Diffraction*, vol. 3, no. 01, pp. 2–6, Jan. 1988.

[13] D. Jansen, S. T. Bergold, F. Goetz-Neunhoeffer, and J. Neubauer, “The hydration of alite: a time-resolved quantitative X-ray diffraction approach using the G -factor method compared with heat release,” *Journal of Applied Crystallography*, vol. 44, no. 5, pp. 895–901, Aug. 2011.